Design of Surface-Supported Bio-inspired Networks for CO2 and O2 Activation at Room Temperature

THÈSE N^{O} 8377 (2018)

PRÉSENTÉE LE 16 JUILLET 2018

À LA FACULTÉ DES SCIENCES DE BASE
LABORATOIRE DE SCIENCE À L'ÉCHELLE NANOMÉTRIQUE
PROGRAMME DOCTORAL EN PHYSIQUE

ÉCOLE POLYTECHNIQUE FÉDÉRALE DE LAUSANNE

POUR L'OBTENTION DU GRADE DE DOCTEUR ÈS SCIENCES

PAR

Daniel Eduardo HURTADO SALINAS

acceptée sur proposition du jury:

Prof. N. Grandjean, président du jury
Prof. K. Kern, Dr M. A. Lingenfelder, directeurs de thèse
Prof. C. Ocal, rapporteuse
Prof. A. Arnau Pino, rapporteur
Dr M. Pivetta, rapporteuse

ÉCOLE POLYTECHNIQUE
FÉDÉRALE DE LAUSANNE
Suisse
2018

Esta tesis está dedicada a mis adorados padres,

Eduardo Hurtado y Raquel Salinas.

Acknowledgements

First of all, I would like to express my special gratefulness to my supervisor Dr. Magali Lingenfelder. Four years ago, her letter of acceptance gave me the big chance to belong to her group at the EPFL. I am thankful for the friendly working environment that I found at her laboratory, which gave me the best conditions to perform my research. I am very grateful for all the valuable knowledge that I got at her laboratory during the development of my PhD studies.

I would like to express my sincere gratitude to my supervisor Professor Klaus Kern for the big opportunity to belong to his group. To give me the invaluable chance to have a scientific experience in two remarkable institutions, such as the EPFL in Switzerland and the Max Planck Institute for Solid State Research of Stuttgart in Germany as part of my PhD program.

I would also like to thank to Dr. Fernando Cometto for his guidance, giving me comments and suggestions for improving the scope and structure of my thesis. I will never forget his active participation and his help in the last stage of my thesis, because that gave me the motivation that I needed. I like to thank to Dr. Gustavo Ruano, for his time and patience to teach me all about the vacuum systems and for his help in the analysis of the XPS spectra. While we repaired the STM system, he provided me with the technical information that was very useful during my whole PhD program. Special thanks also go to Ane Sarasola and Prof. Andres Arnau from the Donostia International Physics Center in Spain, for performing the DFT calculations presented in this thesis.

I would also like to thank to my colleague Bart Stel for giving me always a hand in the laboratory, and for his direct help with my research during the long days at the synchrotron facilities. I also want to thank to my colleague Karla Banjac for the discussions about chemistry. To my friends Ana, Murari and Eleonora with whom I shared many experiences in Switzerland, making my PhD life here more enjoyable especially with our meetings at the bar of the university.

Finally but not last, I would like to thank to Mélissa Josseron for all her love, her help and concern during the completion of my thesis. Merci beaucoup pour ton soutien ma chérie. This thesis and the whole path that preceded would not have been concluded without the constant support of my lovely family. My parents Eduardo Hurtado and Raquel Salinas, my sister Gabriela Hurtado and my brother Marco Velasquez always encouraged me for not to give up, to pursue my dreams and to face up any problem that could appear in my life. Ustedes son el motor de mi vida.

Abstract

The structure of a biological system defines its function. Therefore, nature has developed sophisticated systems that catalyze chemical reactions that are vital for life on earth. For instance, photosynthesis is a biological process that is partially regulated by the metallo-enzyme RuBisCO (Ribulose-1,5-bisphosphate carboxylase/oxygenase), whose function is to catalyze the capture and transfer of CO_2 into organic molecules. This carboxylation reaction occurs at the active site, where a magnesium ion (Mg^{2+}) is bound to organic molecules with carboxylate (COO^-) and amine (NH_2) functional groups.

In the last decades, supramolecular chemistry has proven to be a valid approach to replicate the structural characteristics of these natural metal-organic systems. Metal atoms and organic molecules are used as building blocks to form two-dimensional (2D) metal-organic networks (MONs) on metal surfaces, through a self-assembly process that occurs spontaneously. In these systems the molecules bind to the metal centers and control their oxidation state that, as found in metallo-enzymes, is crucial to perform a catalytic task. Therefore, these supramolecular assemblies show promising features to be explored for heterogeneous catalysis.

The main objective of this thesis is to *reverse the structure-function equation*, that is: instead of finding specific functions of well-known 2D structures for future applications, 2D structures are designed to reproduce the specific functions of well-known bio-systems. Thus, inspired in the structure of the active site of RuBisCO, 2D Mg-based supramolecular assemblies are rationally designed on Cu(100) or Mg(0001) surfaces at room temperature (RT) as a platform for CO_2 adsorption. This work is the first study of self-assembly of alkaline earth metal atoms (Mg) with organic molecules ((1,4-benzenedicarboxylic acid (TPA) and 2,4,6-tris(4-aminophenyl)-1,3,5-triazine (TAPT)) on metal surfaces.

The first part of this thesis investigates the self-assembly of TAPT molecules. Scanning Tunneling Microscopy (STM) and High Resolution X-ray Photoemission Spectroscopy (HR-XPS) demonstrate that the molecules typically semi-deprotonate to form MONs with the adatoms from the host substrates. The exposure of these structures to CO_2 results in the carboxylation of the amino groups.

The second part proves that the COOH moieties of TPA molecules fully-deprotonate to form homo-molecular structures. The incorporation of Mg adatoms result in ionic MONs, which reproduce the carboxylate environment of the active site of RuBiSCO. STM, XPS and Density Functional Theory (DFT) analyze the structural changes, the chemical reactions and charge transfer during either the CO_2 or O_2 adsorption on the Mg^{2+} centers.

The last part focusses on the co-deposition of both molecules to form 2D metallic-hetero-molecular networks with Mg^{2+} centers. The role of the Mg^{2+} centers as active sites for molecular adsorption and model systems for gas storage is studied. STM reveals that CO_2 partially modifies

the network towards a configuration that resembles the active site of RuBisCO. The formation of 3D structures to enhance CO_2 adsorption is also evaluated.

Keywords: RuBisCO, active site, adsorption, carbon dioxide, metal-organic networks, magnesium, amine groups, carboxylate groups, ultra-high vacuum, room temperature.

Résumé

La structure d'un système biologique définit sa fonction. Par conséquent, la nature a développé des systèmes sophistiqués qui catalysent les réactions chimiques vitales pour la vie sur terre. Par exemple, la photosynthèse est un processus biologique partiellement régulé par la métallo-enzyme RuBisCO (ribulose-1,5-bisphosphate carboxylase/oxygénase), dont la fonction est de catalyser la capture et le transfert du CO_2 dans les molécules organiques. Cette réaction de carboxylation se produit sur le site actif, où un ion magnésium (Mg^{2+}) est lié à des molécules organiques avec des groupes fonctionnels carboxylate (COO^-) et amine (NH_2).

Au cours de la dernière décennie, la chimie supramoléculaire utilise une approche ascendante pour reproduire les caractéristiques structurelles de ces systèmes organométalliques naturels. Ainsi, des atomes métalliques et des molécules organiques sont utilisés comme blocs de construction pour former des réseaux organométalliques (MONs) en deux dimensions (2D) sur des surfaces métalliques, à travers un processus d'auto-assemblage qui se produit spontanément. Dans ces systèmes, les molécules se lient aux centres métalliques et contrôlent leurs états d'oxydation qui, comme dans les métallo-enzymes, sont cruciaux pour effectuer une tâche catalytique. Ces assemblages supramoléculaires montrent donc une voie prometteuse vers la catalyse hétérogène.

L'objectif principal de cette thèse est de *renverser l'équation structure-fonction*, c'est-à-dire: au lieu de trouver des fonctions spécifiques de structures 2D pour des applications futures, les structures 2D sont conçues pour reproduire les fonctions spécifiques des bio-systèmes bien connus. Ainsi, inspirée de la structure du site actif de RuBisCO, des assemblages supramoléculaires 2D à base de Mg sont conçus rationnellement sur des surfaces Cu(100) ou Mg(0001) à température ambiante (RT) comme méthode d'adsorption du CO_2. Ainsi, voici la première étude de l'auto-assemblage des atomes de métaux alcalino-terreux (Mg) avec des molécules organiques (acide 1,4-benzènedicarboxylique (TPA) et 2,4,6-tris(4-aminophényl)-1,3,5-triazine (TAPT)) sur des surfaces métalliques.

La première partie de cette thèse étudie l'auto-assemblage des molécules TAPT. Le Microscope D'effet Tunnel (STM) et la Spectroscopie de Photoémission par Rayons X à Haute Résolution (HR-XPS) démontrent que les molécules se déprotone de manière partielle pour former des MONs avec les adatomes des substrats hôtes. L'exposition de ces structures au CO_2 entraîne la carboxylation des groupes amino.

La deuxième partie prouve que les fragments COOH des molécules de TPA se déprotonent complètement pour former des structures homo-moléculaires. L'incorporation d'adatomes de Mg forme des MONs ioniques, qui reproduisent l'environnement carboxylate du site actif de RuBiSCO. STM, XPS et la Théorie de la Fonctionnelle de la Densité (DFT) analysent les changements structurels, les réactions chimiques et le transfert de charges lors de l'adsorption de CO_2 ou d'O_2 sur les centres Mg^{2+}.

La dernière partie se concentre sur la co-déposition des deux molécules pour former des réseaux métalliques-hétéro-moléculaires en 2D avec des centres Mg^{2+}. Le rôle des centres Mg^{2+} en tant que sites actifs pour l'adsorption moléculaire et le stockage de gaz est étudié. La STM révèle que le CO_2 modifie partiellement le réseau vers une configuration qui ressemble au site actif de RuBisCO. La formation de structures 3D pour améliorer l'adsorption de CO_2 est également évaluée.

Mots-clés: RuBisCO, site actif, adsorption, dioxyde de carbone, réseaux organométalliques, magnésium, groupements aminés, groupements carboxylates, ultravide, température ambiante.

Table of contents

List of Figures

List of Tables

Chapter 1: Introduction

"Bio-inspired 2D networks to mimic the catalytic function of the RuBisCO enzyme"

Life on earth is affected by a global warming caused by the increment of CO_2 emissions. Unfortunately, the natural processes cannot carry-on with the excess load of CO_2 and give us the obligation to address strategies to reduce our carbon footprint on earth. During billions of years nature has developed photosynthesis, a self-sustaining process partially regulated by the RuBisCO enzyme. Thus, a promising approach towards artificial photosynthesis is to replicate the RuBisCO active site. Supramolecular chemistry allows the rational design of nano-architectures, which self-assemble to mimic the structural characteristics of enzymatic active sites for hetero-catalysis. This chapter presents the theoretical background that encourages the design of 2D supramolecular structures to be used as nano-catalysts for CO_2 adsorption.

1.1. The Photosynthesis Process

Photosynthesis is the model system for energy conversion. It is used by plants, algae or bacteria to transform light into chemical energy, *i.e.* organic molecules or biomass [1]. The process can be simplified as a chemical reaction that uses water (H_2O), carbon dioxide (CO_2) and energy from the sunlight to obtain sugar (glucose: $C_6H_{12}O_6$) and oxygen (O_2) as other sub-products:

$$6H_2O + 6CO_2 + light \rightarrow C_6H_{12}O_6 + 6O_2$$

Photosynthesis is performed in two steps known as the light and dark reactions. Each step occurs in two different structures of the chloroplasts from eukaryotic cells [2]:

- *The first step (light reaction), takes place in the thylakoids membranes*. H_2O and light are processed to produce O_2 as a waste product. Whereas, the energy from the sun is stored in molecules such as Nicotinamide adenine dinucleotide phosphate (NADPH) and into Adenosine Triphosphate (ATP).
- *The second step (known as the Calvin cycle or dark reaction) takes place in the stroma*. CO_2 is captured as a starting reactant to be transformed into carbohydrates ($C_6H_{12}O_6$),

using the chemical energy from the ATP and NADPH molecules obtained from the *light reaction*.

The Calvin cycle can be further divided in three different stages:

- *1st stage - Carbon fixation:* It is the first and rate-determining stage of this cycle and it is regulated by the enzyme RuBisCO. This enzyme immobilizes and activates a CO_2 molecule to catalyze a reductive carboxylation reaction that transforms a five-carbon sugar molecule, Ribulose 1,5-bisphosphate (RuBP), into two three-carbon molecules (3-phosphoglycerate (3-PGA)), which later act as building blocks for sugars [3].
- *2nd stage - Reduction:* The ATP and NADPH macromolecules deliver energy and fix a H^+ proton into the molecular structure of the two 3-PGA molecules, transforming it into Glyceraldehyde 3-Phosphates (G3P). The G3P is further assembled into a hexose sugar (glucose, $C_6H_{12}O_6$).
- *3rd stage - Regeneration:* Most of the produced G3P is recycled to regenerate the RuBP so that it can be used in a new Calvin cycle.

1.2. RuBisCO and the role of Magnesium for Catalysis

This thesis centers in the mimicking of the first stage of the photosynthesis process (*Carbon fixation*), regulated by the active site of the RuBisCO enzyme [3], [4]. To define the structure of RuBisCO, it is first necessary to address the basic structure of an enzyme: Amino acids. The structure of these organic compounds consists of an alpha-carbon terminated by -NH_2 and -COOH functional groups and a side chain (R) group that gives unique properties to the amino acids. The amino acids bind covalently to each other in a consecutive manner to form polypeptides, whose structure terminates with a COOH group in one side, and a NH_2 group in the other. The 3D fold of one or more polypeptides in a specific shape forms large macromolecules denominated proteins. Enzymes are big proteins capable of speeding up a reaction, i.e. catalysis. Photosynthesis, water oxidation, glycolysis, oxygen reduction and cellular respiration are good examples of biological processes catalyzed by enzymes. In addition, some of these enzymes contain metal atoms in their active centers (metallo-enzymes), where a molecule can be attached to be further catalyzed, e.g. H_2O_2 or CO_2 in the case of Catalase or RuBiSCO enzymes, respectively [5], [6]. The metallic centers bind to the enzyme through the functional groups of the amino acids (NH_2, COOH, and the functional groups from the R chains) [7].

Mg^{2+} participates in many biological processes as an active center. Mg^{2+} shows an affinity for carboxylate (COO^-) functional groups which allows its interaction with organic carbon-based macromolecules [8]. Particularly, Mg^{2+} plays an important role in the catalytic function of RuBisCO. On its first stages, the structure of this metallo-enzyme contains H_2O molecules, glutamate (Glu204) and Asparate (Asp203) residues, whose monodentate COO^- groups link the Mg^{2+} ion. This structure does not have any catalytic activity by itself, unless the ε-NH_2 group of a non-bonded lysine residue (*Lysine 201*) performs a nucleophilic attack to a CO_2 molecule to form a negatively charged carbamate, which gets stabilized electrostatically with the Mg^{2+}

center (**Figure 1.1(a)**) [9], [10]. From here, the RuBisCO enzyme becomes functional to allow the further binding of a RuBP molecule, through two of its highly electronegative O atoms, to the Mg^{2+} center [3]. Thus the active site of RubisCO is formed (**Figure 1.1(b)**), and presents a structure based on a Mg^{2+} ion coordinated by six O atoms in an octahedral geometry. This structural conformation of the molecules is crucial to allow the carboxylation reaction **(Figure 1.1(c))**.

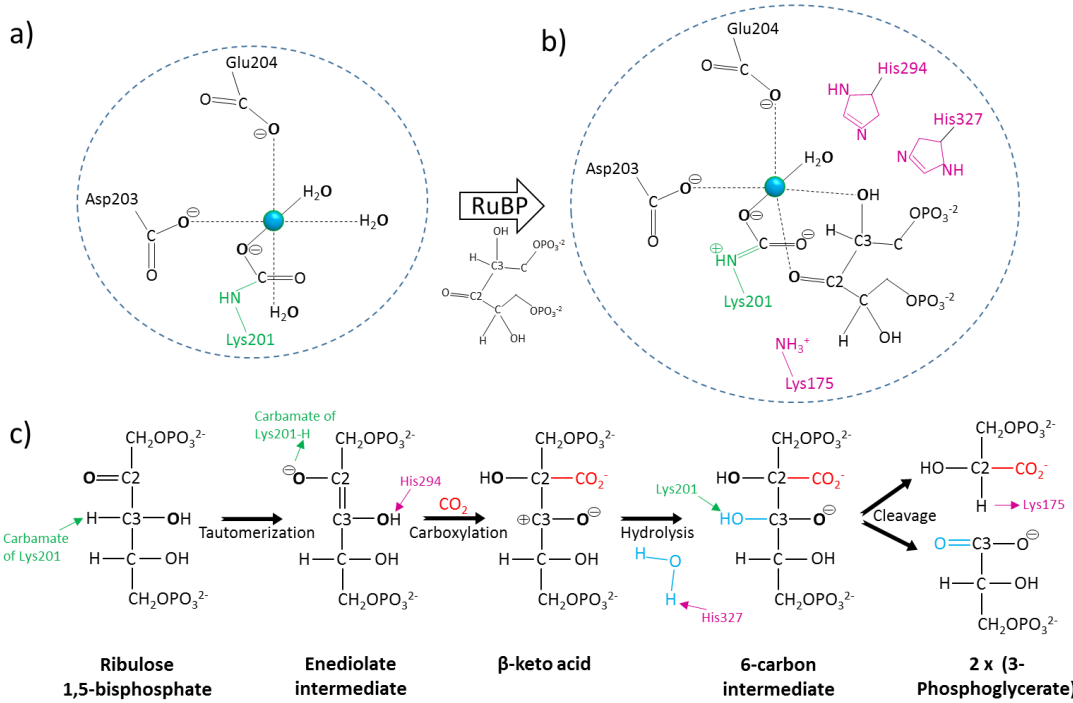

Figure 1.1: (a) The carbamylation of the Lysine 201 turns the active center of RuBisCO "functional" to allow the further introduction of RuBP. (b) Structure of the active center of the enzyme before carboxylation, where a Mg^{2+} ion is surrounded (in a D4h symmetry) by 6 oxygens: three from the amino acid residues glutamate, asparate and carbamylated Lysine 201, two from the RuBP and one from a H_2O molecule [4]. (c) The reductive carboxylation reaction catalyzed by the enzyme RuBisCO. A RuBP molecule absorbs a CO_2 molecule to form two 3-PGA molecules.

The carbamate of Lys201 subtracts a H^+ from the C3 in RuBP and brings it to the negatively charged O attached to the C2, as a result of the tautomerization of RuBP into an enediolate intermediate. The next step involves the carboxylation catalyzed by the enzyme, which begins when the H_2O molecule in the active site is replaced by a CO_2 molecule that is polarized by its proximity to the Mg^{2+}. A histidine residue (His294) subtracts a second H^+ from the O attached to the C3 to allow the nucleophilic attack of the enediolate intermediate to the CO_2 molecule. Note that after carbon fixation, this intermediate β-keto six-carbon compound is unstable and induces the C3 to react immediately with a H_2O molecule, in a hydrolysis reaction that releases a H^+ to be taken by a histidine residue (His327). Thus, a different six-carbon intermediate is formed while the carbamate of Lys201 subtracts a H^+ from the OH attached to the C3 to generate a C-C cleavage. The cleavage is back-upped by the donation of a H^+ from a lysine residue (Lys175) to

one of the sub-products to finally generate two 3PGA molecules [3], [11]. Hence, the carbamate of lys201 plays an important role during the catalysis for the carbon transfer, that takes place when RuBP reacts with a different CO_2 molecule [12].

At lower levels of CO_2, O_2 molecules compete with CO_2 to react with the RuBP. In this reaction, O_2 reacts with RuBP and produces a 3PGA molecule at high-energy expenses. The oxygenation reaction consumes extra energy (ATP) to eventually liberate CO_2. Thus, this process called photorespiration, wastes the energy produced during photosynthesis. The result is also a toxic by-product that is hazardous for many living organisms. Because of the oxygenation reaction, the enzyme is considered inefficient and motivates scientists to investigate ways to improve the enzymatic function of RuBiSCO.

1.3. Metal-Organic Networks

Metal-organic networks (MONs) are 2D self-assemblies of organic molecules and metal atoms supported on a substrate [13]. These supramolecular structures resemble the basic configuration of the active sites in metallo-enzymes. A large diversity of metal-organic motifs (**Figure 1.2**) can be designed and synthesized in a reproducible manner by the control of several parameters such as [14], [15]:

- The type of substrate.
- The nature of the metal centers and their oxidation number.
- The functional groups and the structure of the molecular backbones.

In general terms, the substrate gives a support to the adsorbates (metal atoms and organic molecules) for their self-assembly into 2D structures. The crystallographic symmetry of the substrate provides a template for the 2D assemblies, to grow with a preferential order and different structural configurations. Sometimes the interaction between the adsorbates is stronger than their binding energy with the substrates, thus it is possible to obtain self-organized assemblies with similar geometries regardless of the nature of the substrates [16], [17].

The design of a metal-organic network also comes hand in hand with the right choice of the adsorbents. Thus, it is important to know the nature of the metal centers as their electronic, magnetic and chemical properties may change depending on their electron affinity, the quantity or the functional groups of the ligand molecules, the type of substrate or the structural geometry of the structure where they are embedded. Several works have reported that transition metal atoms (d-block) can form well-defined structures through a metal-organic coordination with organic ligands [18]–[22]. Whereas, alkali metals such as Na, K or Cs (group I) normally lose an electron from the outer atomic shell (cation), and bind electrostatically with anionic molecules (due to their big difference in electronegativity), to form ionic networks [23]–[28]. The nature of the ionic bonds allows the formation of polymorphs, in contrast with the coordination bonds that tend to be directional in terms of network organization.

Thus, the functional groups of the organic molecules play the important role of binding the metal atoms to form the 2D supramolecular assemblies. Depending on their functional groups, the molecules can act as electron withdrawers or donators to stabilize the redox potential of the

metal centers. As it was mentioned above, the functional groups of the amino acids bind the metal ions present in the active sites of the metallo-enzymes [7]. Therefore, supramolecular chemistry has focused its attention in the formation of MONs with molecules whose functional groups are present in the amino acids. Hence, COO^- (and its protonated form COOH) is one of the most recurrent functional groups used as a building block in MONs, since the carboxylate oxygen forms strong bonds with the metal centers and control their redox potential [29], [30]. On the other hand, NH_2 is a functional group that can semi-deprotonate to form a metal-organic coordination bond with a metal adatom [31], [32]. In general, the formation of MONs has being studied in molecules with N-based functional groups such as nitrile end-groups (R-C≡N) [33]–[35]. Finally, some works have also reported the formation of MONs with functional groups from the R-group such as, hydroxyl [36], thiol [37], [38] or pyridine (imidazole) [16], [39], [17]. An additional role of the organic molecules is related to their molecular backbones, which control the separation and the even distribution of the metal centers along the surface. This generates pores or cavities in the structure which can act as reservoirs for guest molecules [40]–[42], gas adsorption [43] or centers for catalysis [44].

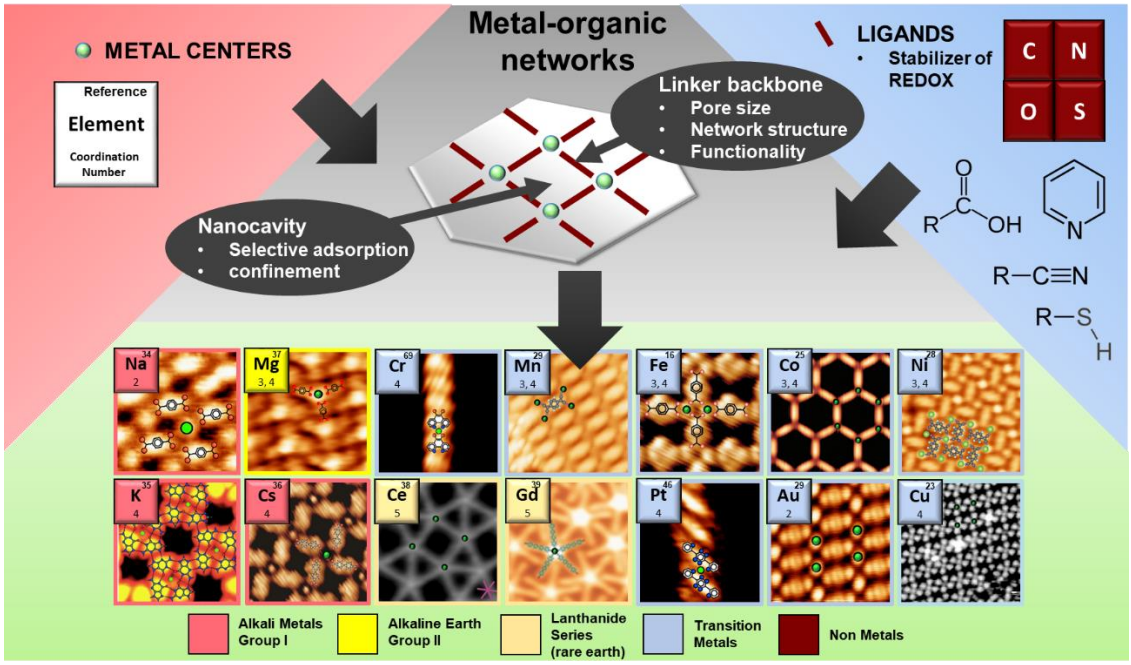

Figure 1.2: Structural characteristics of 2D MONs. Different structures can be formed tuning the type of metal or organic ligands deposited on a substrate. Image modified from refs [14], [45].

1.4. CO_2 and the catalytic gas adsorption on metals

CO_2 is a vital molecule for life on earth. It exists in a gaseous state in the atmosphere and is one of the most relevant and abundant components of greenhouse gases. CO_2 is expelled by different natural processes of the planet such as volcanic eruptions, oil or gas deposits, hot springs, the oceans and even from the respiration of animals. Since the industrial revolution, humanity has relied on burning fossil fuels as a primary source of energy, turning us into an

active contributor of CO_2 emissions. When CO_2 is trapped in the atmosphere, it prevents sunlight to be reflected back into the space [46], and in turn induces a global warming that affects the life on earth. This situation gives us the need to find new energy sources, or new technologies for energy conversion and storage, using the already existing excess of CO_2 as a carbon source [47]. Therefore, it is of special interest to find systems that can capture/absorb CO_2.

CO_2 is a thermodynamically stable molecule, whose ambivalent reactivity given by its nucleophilic oxygen and electrophilic carbon atoms, allows different type of interactions with transition metals [48]. Several methods have been investigated for catalyzing the CO_2 absorption [48]. In electro catalysis, copper (Cu) has proved to be a good catalyst candidate due to its high selectivity to hydrocarbons, that depends on the crystallographic orientation. Thus, Cu(100) and Cu(111) surfaces can catalyze the formation of ethylene and methane, respectively [49]. Under UHV conditions at RT, CO_2 is a relatively unreactive gas that physisorbs on metallic single-crystals with low Miller indexes such as [100], [110] or [111]. Exceptionally, the enhancement of the CO_2 reactivity towards a chemisorption has been shown in the presence of surface defects, oxide layers or surface doping with alkali metal atoms [50], [51].

A recent work has reported that CO_2 interacts with Cu substrate-supported amines, to form carbamates [52]. In nature, carbamates form supramolecular complexes with metals in the active center of the enzymes [12]. Recently, there exists interest for metal-organic frameworks (MOFs) in terms of gas separation, storage and catalysis. MOFs have been used to reproduce a structure similar to the active site of RuBiSCO, with a Mg^{2+} ion coordinated by six carboxylate oxygen atoms [53]; showing that the metal centers play a central role for gas capture [54]. Indeed, the metal centers in some Mg-based MOFs have shown selectivity in the adsorption of gases such as ethane, ethylene, propane and propylene [55]; whereas, in Mg, Cu and Ni-based MOFs have demonstrated CO_2 adsorption/desorption [54], [56], [57].

On the other hand, 2D MONs have also been presented as 2D analogs of 3D MOFs, and therefore as model systems for gas adsorption, allowing the visualization of processes occurring at MOFs. The functional group of the ligand molecules can control the redox properties of the metal centers [58]–[60]. Recent studies of the electronic properties of 2D networks with Pt or Fe centers have shown a hybrid behavior of the metal centers: They participate in the formation of metal-organic bonds and they also act as isolated adatoms with an oxidation state [60], [61]. These findings opened a route towards the fabrication of MONs bio-inspired in the structure of the active sites of metallo-enzymes [62]–[64]; where the oxidation state of the metallic centers plays an important role in their catalytic function. Hence, a recent work in 2D networks of TPA molecules coordinating Fe dimers, have shown the adsorption of O_2 and CO_2 molecules at RT and 100 K, respectively [58], [65]. In addition, the pore sizes in the MONs, could serve as reservoirs for guest molecules [41]. In this work, the enzyme RuBisCO was used as an inspiration to form 2D MONs that mimic the catalytic CO_2 adsorption.

Chapter 2: Techniques and Methods

Surface science allows the precise control of matter at the atomic level to rationally design complex 2D nano-architectures. A deep understanding of these systems requires the use of instruments and techniques with enough accuracy to characterize the structural characteristics at the atomic scale. This thesis mainly uses Scanning Tunneling Microscopy (STM) as a baseline to study the structure of supramolecular self-assemblies. Therefore, this chapter presents the theoretical background and the description of the set-up behind this powerful instrument. Furthermore, it shows the fundamental concepts behind complementary spectroscopic techniques, such as X-ray Photoemission Spectroscopy (XPS), and Density Functional Theory (DFT) level of theoretical calculations. All together provide a complete comprehension of complex systems at the atomic scale.

2.1. Scanning Tunneling Microscope (STM)

Nanotechnology studies structures with dimensions below 100 nm in size, where quantum effects take place. STM is an instrument that uses the quantum barrier principle of quantum mechanics to observe the surface of a sample with atomic resolution. Its invention was conferred to Gerd Binnig and Heinrich Rohrer in 1981, who were later awarded with the Nobel Prize in Physics in 1986, opening the door to a new world ruled by the atomic interactions. STM is a local imaging technique that reveals the spatial information of a surface at the atomic level [66]. It presents versatility either to work as a spectroscopic technique (Scanning Tunneling Spectroscopy (STS) [67]) that provides information of the vibrational modes in single molecules, or to manipulate atoms to form complex nanostructures or new molecules by induced chemical reactions [68].

The STM consists of a very sharp metallic tip made of tungsten (W) or Platinum-Iridium (PtIr) alloys, prepared by etching or by simple wire cutting. The imaging process begins approaching the tip to a conductive surface (sample), with the enough gap separation to detect a tunneling current signal (*I*) when a bias voltage (*V*) is applied (**Figure 2.1(a)**). Between the tip and the sample there is an insulating barrier of vacuum. Thus, the flow of transmitted electrons decreases exponentially with a bigger gap separation due to the quantum electron tunneling effect. The sharpness of the tip should reach a dimension as small as the size of an atom. Therefore, the apex of the tip (that is composed by just few atoms) presents an outermost atom that allows the flow of well-localized electron tunneling currents, to generate images able to resolve individual atoms. Hence, a feeble tunneling current signal is tested in nanoamperes (*nA*), for typical bias voltages up to 10 *V* (**Figure 2.1(b)**). The polarity bias controls the direction of the current between the tip and the sample: A negative bias (as used in all the STM images

presented in this thesis), allows the electrons to tunnel from the occupied states of the sample to the unoccupied states of the tip, while for a positive bias occurs the opposite.

Two piezos control the mechanical movement of the tip along the X and Y directions, to scan line by line the topography of the surface with an angstrom-level control. The tip operates in two different modes: constant height and constant current. In this thesis, the STM works in the constant current mode, that allows the tip to move up and down (in the Z-axis) in order to maintain a constant height, while a bias voltage is applied between the tip and the sample. The movement in the Z-axis is controlled by a third piezo that is contracted or expanded with a precision in picometers, while a preset current is compared at every X-Y position on the surface. If the tunneling current exceeds (or falls below) the preset value, a feedback circuit provides a correction voltage that increases (or decreases) the tip-sample distance. As a result, a high-resolution three-dimensional map of the surface topography down to the atomic scale is plotted, *i.e.* about 0.5 Å lateral and 0.01 Å vertical pixel area.

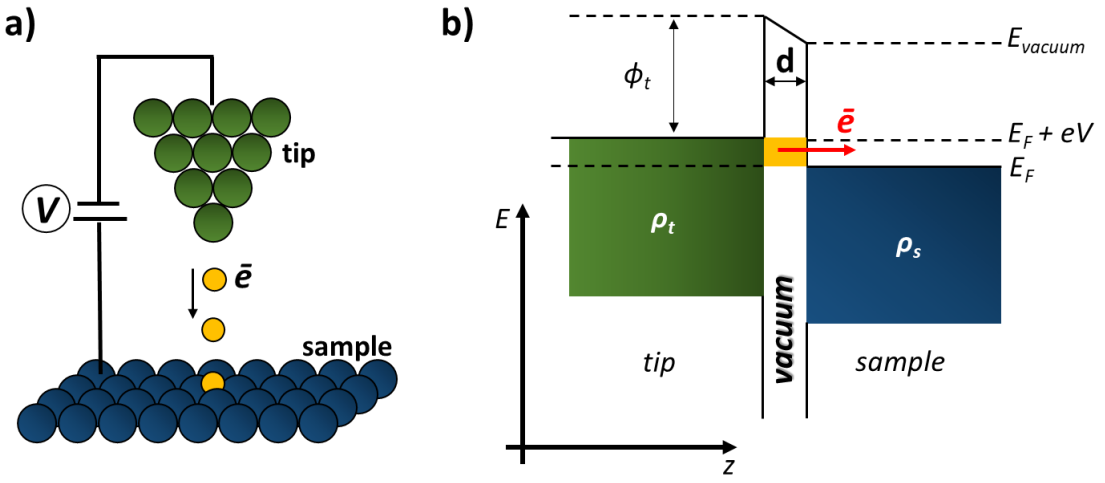

Figure 2.1: (a) Scheme of the STM tip that shows a tunneling current between the apex atom on the tip and the sample, when a positive bias is applied. (b) Scheme of the tunneling junctions showing the flow of the electrons tunneling from the tip to the sample when a voltage bias is applied. In both the tip and the sample, the energy levels of the electrons are filled up to the Fermi level E_F. When the tip and the sample get closer, the electron wave functions overlap; however, there exist a barrier energy that prevents the electron flow. A bias voltage is applied between the tip and the sample to overcome the energy of the barrier, thus to allow a net current flow.

To understand how the topography of the surface is obtained, it is necessary to analyze the theory behind the tunneling effect of the current flowing between the tip and the sample. The Bardeen approach [69], that is based on the Fermi's golden rule, considers all the quantum states between the tip and a metallic sample to give an estimation of the tunneling current (*I*):

$$I(V) = \frac{2\pi e}{\hbar}\sum_{s,t}\big(f(E_s)[1 - f(E_t + eV)]|M_{st}|^2\delta(E_s - E_t)\big)$$

Where $f(E)$ is the Fermi-Dirac function, related to the current tunneling from the occupied states of the sample to the unoccupied states of the tip. *V* is the bias voltage applied to the sample. E_s and E_t are the energies respect to the Fermi level (E_F) in a delta function (δ) that describes the elastic tunneling *i.e.* there is no loss of energy while the electron tunnels. M_{st} represents the tunneling matrix element between ψ_s and ψ_t(the wave functions for the sample and the tip, respectively), and it is calculated as:

$$M_{st} = \frac{\hbar^2}{2m}\int(\psi_s^*\nabla\psi_t - \psi_t\nabla\psi_s^*)dS$$

Considering a case in the limit of zero temperature and small *V*, the equation can be simplified as:

$$I(V) = \frac{2\pi eV}{\hbar}\sum_{s,t}\big(|M_{st}|^2\delta(E_s - E_F)\cdot(E_t - E_F)\big)$$

The calculations of Tersoff-Hamann assumed a system based on a sharp metallic tip, with a single atom at the apex that can be modeled with a radially symmetric electron density (s-orbital). Therefore, if the Fermi level is considered to be at $E_F = 0\ V$, the equation is further simplified to:

$$I(V) \propto \int_0^{eV}\rho_s(E,\vec{r})\cdot\rho_t(E - eV)\cdot\mathcal{T}(E, eV, d)dE$$

With ρ_s as the local density of states (LDOS) of the sample, right below the apex atom of the tip ($\vec{r}$) at the Fermi level, and ρ_t as the LDOS of the tip at a certain voltage *V*. Here, $\mathcal{T}$ is introduced as the transition matrix derived from M_{st}, that considers the mass of the electron (m_e) and the work functions of the sample (ϕ_s) and the tip (ϕ_t), to describe the exponential dependence of the tunneling probability when the tip apex and the sample are separated by a certain distance, *d* (in Å):

$$\mathcal{T}(E, V, d) = e^{\left(-2d\sqrt{(m_e/\hbar^2)\cdot(\phi_s + \phi_t - 2E + eV)}\right)}$$

Considering small enough voltages $\approx 0.1 - 3\ V$, leaves the contribution of $-2E + eV$ neglected respect to the work functions $(-2E + eV \ll \phi_s, \phi_t)$. Hence, $\kappa = \sqrt{(m_e/\hbar^2)\cdot(\phi_s + \phi_t)}$ is introduced to get a final equation that describes the tunneling current as:

$$I(V) \propto e^{-2\kappa\cdot d}\int_0^{eV}\rho_s(E,\vec{r})\cdot\rho_t(E - eV)dE$$

The first factor describes the exponential dependence of the current with *d*. This implies that the tunneling current is only carried-out by the outermost atom in the tip, since the neighboring atoms carry a negligible amount of current as a consequence of the exponential decay. On the other hand, the factors inside the integral show the influence of the LDOS from both the tip and the surface in the current signal.

Placing all together, the STM images can be interpreted as the observation of the electronic configurations that are typically influenced by the LDOS in the region between E_F and E_F+eV, the work functions of both the tip and sample, the tip-sample distance and the bias voltage and the shape of the tip. These factors vary constantly during the STM measurements and give valuable information that is represented in a simple image.

2.1.1. Experimental Setup

The STM is mounted on a chamber kept in ultra-high vacuum (UHV) conditions; the chamber is also equipped with a standard experimental setup to allow the preparation process of the sample *in-situ*:

- ***A homemade scanning tunneling microscope (STM):*** The system relies on a STM tip made of tungsten (W), fabricated by electrochemical etching. The STM tip is mounted in a manipulator that allows its movement in the X, Y and Z directions. During the scans, the STM is operated in constant current mode, with typical tunneling current and sample bias values of 1.0 nA and -1.0 V, respectively. The STM system resides inside a chamber that dangles from the ceiling by four springs, to provide the stability and isolation to the STM against any vibration sources from the building.
- ***Ion sputter gun:*** During preparation, first the surface of the sample is bombarded by accelerated ions of argon (Ar^+). This process begins circulating a current (I = 2.3 A) in a filament mounted on the sputter gun to generate a thermal electron emission. The released electrons impact with *Ar* atoms (which are also being injected during the process), producing their ionization. A high voltage (V = 500 V) accelerates the generated Ar^+ ions towards the sample, which is tilted by 45° with respect to the ion beam. The collision generates a sputter current of 8.0 μA in a surface area of about 13 mm^2. In this thesis, each sputter cycle lasted a maximum of 15 min, unless special conditions are remarked. During sputtering the *Ar* pressure is held at $1.0x10^{-5}$ mbar.
- ***Metal evaporators:*** An EFM 3/4-type UHV evaporator from FOCUS GmbH was used to sublimate Mg from small pellets residing in a crucible. A water flow system is installed through the evaporator to avoid the uncontrolled evaporation of the metal. A retractable load mechanism controls the evaporator-sample distance and, also prevents unwanted evaporation of the metal when the chamber bakes at high temperatures.
- ***Molecular evaporators:*** A home-built apparatus for standard organic molecular beam epitaxy (OMBE) was used to evaporate molecules. It is equipped with two sources; each of them contains a Knudsen cell based on an inert ceramic crucible made of boron nitride or aluminum oxide, where the molecules are placed as powders. A metallic filament heats the crucible, while the temperature is controlled by a thermocouple. A water flow system is installed through the evaporator to avoid the uncontrolled evaporation of the molecules. In addition, a retractable load mechanism controls the evaporator-sample distance to prevent also the unwanted evaporation of the molecules when the chamber bakes at high temperatures. **Table 2.1** shows the structure of the molecules used in this thesis with their corresponding sublimation temperatures. Before

deposition, the molecules were fully degassed, thus during their deposition on the substrates, the pressure in the chamber was not higher than 2.0×10^{-9} mbar.

Table 2.1: Chemical name of the two molecules used in this thesis with their respective sublimation temperatures used for deposition. The group of Bettina Lotsch at the Max Planck Institute for Solid State Research in Stuttgart provided the synthesized molecule (TAPT).

Molecule	**Chemical name**	**Structure**	**T_{subl}**	**Supplier**
TPA	1,4-benzenedicarboxylic acid	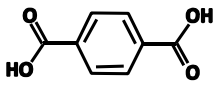	448 K	Fluka (>99%)
TAPT	2,4,6-tris(4-aminophenyl)-1,3,5-triazine	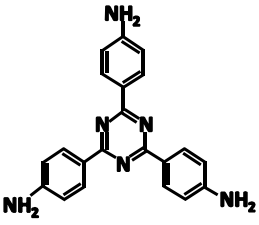	513 K	Prof. Bettina Lotsch

- ***Inlet for gas introduction:*** Standard pressurized bottles with 1.0 bar, carrying gases such as Ar, CO_2 or O_2, are equipped with a fine dosing valve to regulate the gas injection into the chamber, in-situ.
- ***Custom-made dispenser for liquids:*** An inlet equipped with a fine dosing valve regulates the entrance of liquids into the chamber, in-situ. For the case of acetophenone in liquid state, the molecule was placed inside the dispenser and frozen using dried ice. This allows the further pumping of the residual gases inside the line until a pressure of 1.0×10^{-3} mbar is achieved. The procedure was repeated three times and finalized unfreezing the acetophenone.
- ***A mass quadrupole spectrometer:*** To analyze and to quantify the residual gases inside the chamber.
- **Pumping systems:** ***During the preparation process,*** the chamber is pumped by two turbo pumps (TURBOVAC 340M, 370 l/sec and TURBOVAC SL 80, 65 l/sec) connected in series with a membrane pump acting as a backup (DIVAC 0.8T, 0.77 m^3/h). A small ion pump (Varian, 240 l/sec) is also used, to reach a final base pressure of 5.0×10^{-10} mbar in the chamber.

  During the STM measurements, the membrane and the turbo pumps are shut down to avoid vibrational noise, while a gate valve isolates them from the chamber. In this way, the ion pump operates alone, keeping a base pressure of 9.0×10^{-10} mbar in the chamber, to avoid significant contamination on the surface of the single crystals over a period up to a week. ***Pressure gauges*** are mounted in the chamber to control the pressure constantly.

2.1.2. Substrates preparation

The substrates used in this thesis are single crystals of Cu(100) and Mg(0001), provided by Mateck. These substrates act as templates for the growth of MONs. Hence, it is important to perform a cleaning process to obtain atomically clean surfaces with few surface defects and well-defined terraces with transversal lengths of at least 100 nm. This length is ideal to study the self-assembly of molecules and metal atoms on the surface. The cleaning process was performed in an UHV chamber with a base pressure of 5.0×10^{-10} mbar.

2.1.2.1. Preparation of Cu(100)

The surface was cleaned by consecutive cycles of Ar^+ sputtering (0.5 keV) and annealing at temperatures up to 810 K, followed by a slow and gradual cooling down of the crystal to 313 K before starting with the next cleaning cycle. If the single crystal was previously exposed to air conditions, six cycles are necessary to ensure the removal of the oxide layers and impurities from the surface. If the crystal already resides in the chamber, only two cycles are enough to get clean terraces of around 100 nm width, as shown in **figure 2.2.**

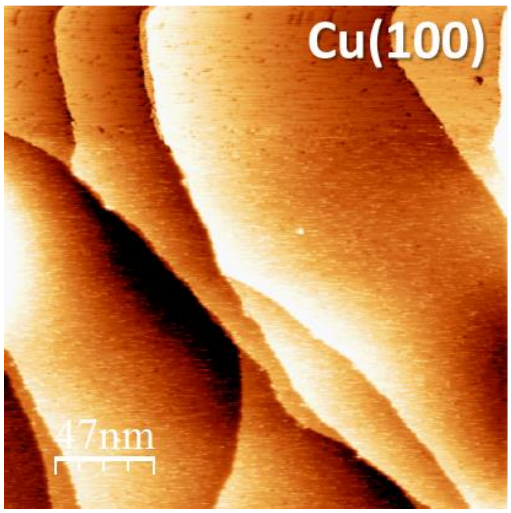

Figure 2.2: STM image of a typical atomically clean Cu(100) surface at RT. Some terraces have a width of around 100 nm. The STM images were taken applying a sample bias of -1V and a tunneling current of 1.0 nA.

2.1.2.2. Preparation of Mg(0001)

This thesis presents for the first time a Mg(0001) substrate as a template to grow 2D nano-architectures. Mg is an alkali earth metal that is very reactive in the presence of molecules such as CO_2 and O_2. As a consequence, unwanted oxide layers are formed on the relatively high reactive surface of Mg(0001). In the literature, few works report complex cleaning methods [70]–[73], and therefore we developed a new cleaning procedure as follows.

If the single crystal was previously exposed to air conditions, the surface is degassed in 16 cleaning cycles on three different stages. The first stage involved 9 consecutive cycles of Ar^+

sputtering (kinetic energies of 0.5 keV) during 15 minutes, followed by a flash annealing at 403 K, and a slow cooling down below 313 K. The second stage involved 5 cycles of Ar^+ sputtering during 10 minutes, followed by a flash annealing at 398 K, and a slow cooling down below 313 K. The third stage involved 2 cycles of Ar^+ sputtering during 10 minutes, followed by a flash annealing at 393 K, and a slow cooling down below 313 K. This resulted in smooth and clean terraces of around 70 nm width, with low amounts of impurities (**Figure 2.3)**. If the single crystal already resides in the chamber, only 2 cycles are required: The first cycle involves Ar^+ sputtering during 15 minutes, followed by a flash annealing at 403 K, and a slow cooling down below 313 K. The second cycle involves Ar^+ sputtering during 10 minutes, followed by annealing at 393 K during 5 minutes, and a slow cooling down below 313 K. This resulted in flat and clean terraces as seen in **Figure 2.3**.

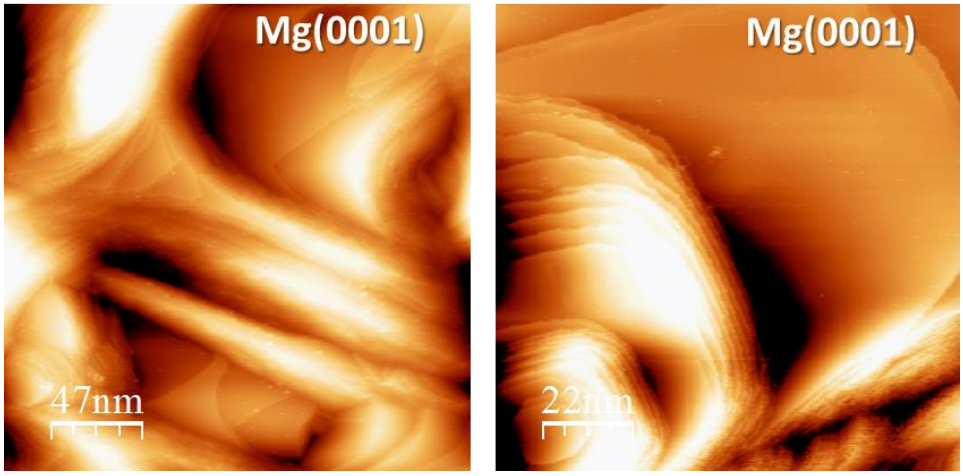

Figure 2.3: STM image of typical atomically clean Mg(0001) surfaces at RT, with smooth terraces with a length of up to 70 nm. The fuzzy step edges are related to the diffusion of Mg adatoms [70]. The STM images were taken applying a sample bias of -1V and a tunneling current of 1.0 nA.

2.2. X-Ray Photoelectron Spectroscopy (XPS)

XPS is a sensitive and generally a non-destructive surface technique that gives information of the electronic structure of atoms and their ionization energies to study the chemical composition of a material. However, this technique cannot provide details about the molecular configuration, unless it is complemented by the special topographic information obtained from STM [68].

The operation is performed in ultra-high vacuum (UHV) conditions, while the X-rays are generated from a monochromatic X-ray source. The principle is based on irradiating a sample with an X-ray beam, with enough energy to be adsorbed by the core levels of an atom to eventually lead to its ionization (**Figure 2.4**). Common sources are made of Mg and aluminum (Al) emitting at 1253.6 and 1486.6 eV, respectively. Other alternative to the regular anodes of Mg and Al is a synchrotron radiation source with energies that can be set-up between few tens to several thousand eV. After irradiation, the excess of energy allows the atom to return to its

original energy state with the ejection of an electron from the inner shells (photoelectric effect). Photo-emitted electrons leave the sample towards a U-shaped electron detector, which counts them and measures their kinetic energy. The intensity of the counted electrons ejected versus the kinetic energy is represented in a spectrum. However, depending on the wavelength of the incident X-ray (*hv*) and the kinetic energy of the ejected electron, the spectrum can also be represented as a function of the binding energy ($E_{binding}$), which can be calculated using the principle of the conservation of energy:

$$E_{binding} = E_{photon} - (E_{kinetic} + \phi)$$

ϕ is the work function of the spectrometer, as the sample and the spectrometer are connected to a shared electrical contact that aligns their E_F.

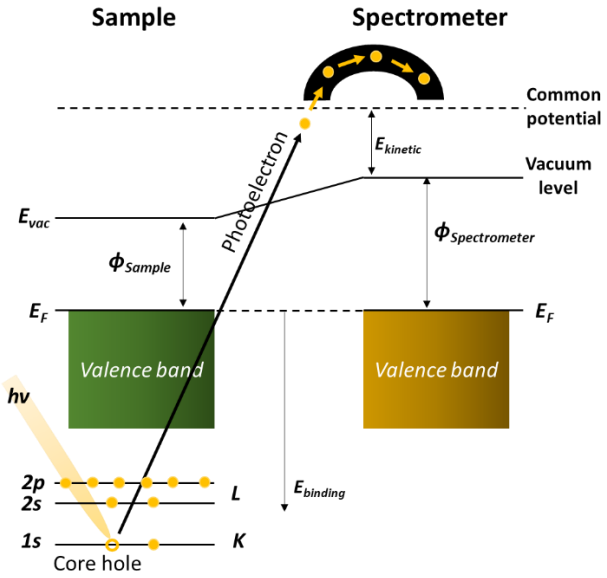

Figure 2.4: Schematic energy diagram of the spectrometer and the sample during the XPS process. An X-ray beam with an incident energy, hv, removes an electron from the inner core shell, which is later detected by the spectrometer.

The peaks appearing at each energy correspond to the atoms emitting electrons with a characteristic environment. The intensities and energy positions at each peak, allow the identification and quantification of all the elements from the surface due to their unique binding energies. The intensity or height of the peaks is proportional to the amount of photoelectrons ejected from a certain energy level; while the areas under the curves measure the relative amount of the elements to calculate their concentrations. Another point of consideration, is the chemical shift in compounds ruled for example by ionic or covalent bonds, which makes the peaks positions to have a shift in energy, allowing the determination of the chemical environment, composition (elements involved), functional groups and oxidation states. The identification of the peak elements and chemical groups is made by a simple comparison with the already known binding energies obtained from the literature.

After the photoemission process, an excited ion is left behind. The ion relaxes through the fall of an electron from an upper shell (e.g. L) to a lower shell (e.g. K), to fill the hole created by the X-ray beam. The energy difference is absorbed by a second electron (Auger electron), that gets enough energy to escape from the atom. Alternatively, the atom can also recover from its ionized state by the emission of a photon (fluorescence). The peaks in the spectra obtained from the Auger electrons do not depend on the photon energy and can be used as references for the characterization of other peaks.

In this thesis, the XPS data were acquired in the X-Ray beamline PEARL at the Swiss light source (SLS) of the synchrotron facilities at The Paul Scherrer Institute (PSI), Switzerland. The energy axis of the spectra is inversed to have a clear representation of the atom structure *i.e.* the closer we are to the nuclei, the higher is the binding energy.

2.3. Density Functional Theory

To determine the electronic properties and structural configuration of molecules on substrates, is a tough task that implies solving the Schrödinger equation for a complex many-body problem with electron-electron, electron-nuclei and nuclei-nuclei interactions. The Born-Oppenheimer approximation is presented as a solution that considers the nuclei fixed, as points of reference, for electrons moving around; however, even simplified, it remains as a many-body problem[68].

First principles Density Functional Theory (DFT), is a supportive method that calculates (at the atomic scale) the structure of molecules and their interactions with the underlying surface and adatoms. This method uses a one-particle Schrödinger equation based on the Hohenberg-Kohn theorem, where the electronic properties are subjected to an external potential, as an alternative solution for the many body-approach [68]. In this way, a molecular system, typically based on up to 100 atoms lying on a substrate, can be simulated including many surface layers to consider a respectable electron interaction.

Based on DFT, the calculations in this thesis were performed using the Vienna Ab-initio Simulation Package (VASP) [74], [75], including van der Waals (vdW) interactions within the van der Waals density functional (vdW-dF) scheme [76]. The use of other methods such as the Tersoff-Hamann approach [8], allowed to simulate supramolecular structures based on the integration of spatially resolved density of states (DOS) in energy, from a certain applied bias potential to the Fermi level, which could be used for data interpretation by comparing with the experimental STM images. Here, DFT calculations are used as a complementary technique to determine the structure of the networks and their reaction with CO_2 and O_2. Ane Sarasola performed DFT calculations under the supervision of Prof. Andres Arnau from the Donostia International Physics Center in Spain. In this chapter, the methods were presented just with a brief descriptive overview. Further details about the theoretical background and the mathematical approaches behind, can be found in references above [68].

Chapter 3: Metal - Organic Networks formed by the direct deposition of TAPT molecules on Cu(100) and Mg(0001) substrates

Metal-organic networks (MONs) are substrate-supported 2D nano-architectures based on metallic nodes bonded to organic bridging ligands. Their physical/chemical properties can be defined by the tunability of the metal centers [39], [77], the organic linkers [19], [36], [78], [79] and pore size [17], [35], [41], [80]. These characteristics give them the potential to mimic the structures of metallo-enzymes. The formation of MONs relies on the self-assembly of metal atoms and organic molecules deposited on a substrate in separate stages [19], [29]. In many cases, the choice of metal centers is independent from the substrate material, which allows the formation of different types of networks [15]. However, metal substrates such as copper present adatoms diffusing on the surface at RT [34], [81]–[83]. Pioneering work by Lin et al. demonstrated the formation of MONs with Cu adatoms as coordination centers [83]. In particular, molecules with N end-groups (such as pyridines, amines, etc.) are good candidates for the formation of networks because the lone pair electrons from the nitrogen site form strong coordination bonds with transition-metal atoms [84], [85]. On the other hand, the formation of 2D supramolecular structures on Mg substrates remains unexplored. This is due to the reactive nature of the Mg surface, which results in the formation of undesired oxide layers. In this context, several works have reported complex cleaning procedures on these surfaces [70]–[73].

In this thesis, the use of MONs is inspired in the mimicking of the structure and the catalytic function of the active site of the RuBisCO enzyme. The aim is to study molecules with the functional groups equivalent to the ones forming the RuBisCO's active site as a route toward hetero-catalysis. Therefore, the first step is to find an analogue to the lysine molecule that contains NH_2 functional groups on its structure. The 2,4,6-tris(4-aminophenyl)-1,3,5-triazine (TAPT) is a three-fold symmetric molecule, based on a triazine ring surrounded by three phenyl groups at its periphery, ending with three equivalent NH_2 groups (inset in **Figure 3.1(a)**). This molecule is attractive for heterogeneous catalysis due to the high content of N atoms present on its structure; e.g. the N-rich triazine ring gives TAPT its photocatalytic properties for hydrogen evolution [86]. TAPT is also used as a precursor in polymers for gas absorption and selection, showing a special affinity for CO_2 [87], [88]. In such case, the N atoms from the triazine ring promote the physisorption of CO_2, which allows its easy detachment from the structure, showing reversibility for gas absorption [89]. On the contrary, the N from the NH_2 groups promote the chemisorption of CO_2, so that eventually stable compounds such as carbamates

can be formed [89]. The triazine and the phenyl groups of TAPT promote its planar adsorption on metal substrates, making it a good candidate to form 2D supramolecular structures under UHV conditions [90], [91]. As seen in molecules with a similar structure (such as melamine (1,3,5-Triazine-2,4,6-triamine)), the NH_2 groups have the potential to partially deprotonate on metal substrates at RT, leaving the nitrogen atoms free to find a coordination center [28]–[30] or, as seen with polymers, to eventually react with CO_2 to form carbamates [89]. These characteristics make TAPT a good candidate to form a 2D analog of the structure of the active site of RuBisCO.

This chapter investigates the molecular interactions of TAPT molecules deposited on Cu(100) and for the first time on Mg(0001) substrates at RT under UHV conditions. The partial or complete deprotonation of the NH_2 groups allows the coordination with the adatoms from the host substrates to form 1D or 2D supramolecular structures. These structures are studied *in situ* by a custom-build STM and HR-XPS performed at the synchrotron. The reactivity of the networks with CO_2 is also investigated, focusing on the potential formation of carbamates, the key step to turn functional the active site of RuBisCO.

3.1. Experimental Setup

The experiments were performed in a UHV chamber with a base pressure of 4.0×10^{-10} mbar. Two different single crystals were used as substrates: Cu(100) and Mg(0001). The surfaces were cleaned following the standard procedures as described in **Chapter 2**. TAPT molecules were deposited by thermal evaporation from a quartz crucible by heating it up to 513 K. During molecular deposition, the pressure in the chamber was kept below 2.0×10^{-9} mbar, while the temperature of the substrates was kept at RT. The STM images were obtained with typical tunneling current and sample bias values of 1.0 nA and -1.0 V, respectively. The XPS spectra were obtained at the PSI synchrotron facilities. The data for the N1s was acquired with a beam energy of 500 eV, the pass energy of the analyser was set at 20 eV. The spectra was referenced using the $Au4f_{7/2}$ line at 84.1 eV. All the experiments were carried out under UHV (~ 3×10^{-10} mbar) at RT.

3.2. TAPT on Cu(100)

Sub-monolayer coverages (0.15 ML) of TAPT molecules were deposited by thermal evaporation onto an atomically clean Cu(100) surface at RT. The STM images from **Figure 3.1(a)** show corrugations along the step edges. The zoom-in of the surface shown in the inset reveals triangular-shaped structures, representing the TAPT molecules interconnecting laterally to each other with a linear periodicity (indicated by the white arrows). The attachment of TAPT on the step edges suggests a direct interaction of the molecules with the surface. The analysis of the surface in a different area (**Figure 3.1(b))** shows that TAPT molecules form small 1D arrangements, which can nucleate from the step edges and from the terraces [85]. The 1D arrangements are formed by the consecutive link of small stable motifs presenting a rhombic-shaped structure. The inset image reveals that the motif is a molecular pair based on two TAPT

molecules that mirror each other in a two-fold straight interconnection. The image also identifies the three-fold rotation symmetry of the molecules, absorbed in a planar geometry with the backbones parallel to the Cu surface, as is typical for polycyclic aromatic compounds [92]–[95]. The interaction between the TAPT molecules in the pairs could be possible through a partial or complete deprotonation of the NH_2 groups. Otherwise, if TAPT is protonated, the lack of H-bond acceptor units would prevent attractive molecular interactions [91].

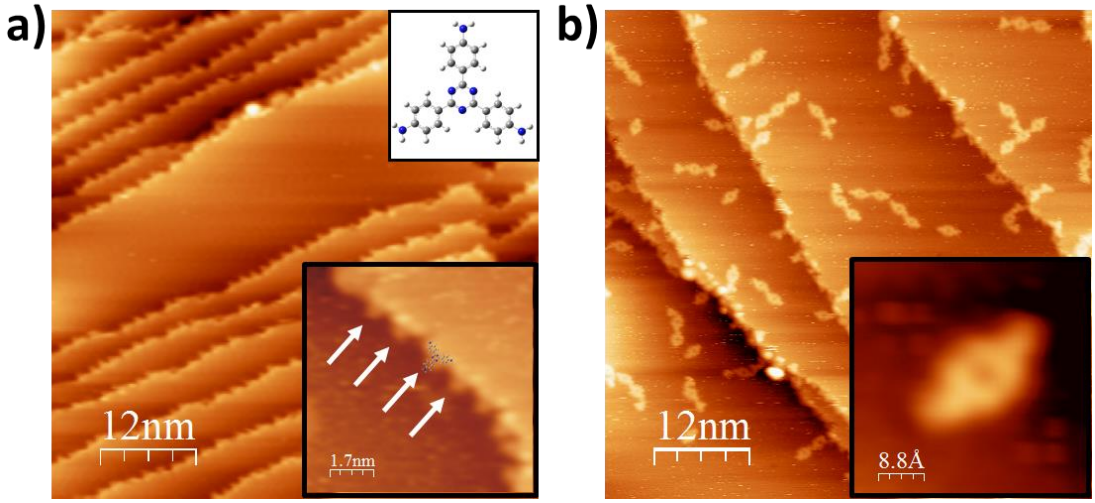

Figure 3.1: STM images show the Cu(100) surface after the deposition of 0.15 ML of TAPT. (a) TAPT molecules decorating the step edges (white arrows in the inset). (b) A different part of the surface reveals few molecules spread along the terraces forming molecular pairs (inset figure). The pairs stack to each other and show the formation of small 1D arrangements. These 1D arrangements can nucleate from the terraces or from the step edges.

A series of consecutive STM images were taken on a defined area on the surface to study the first stages and the evolution of the 1D chains over a period of time (**Figure 3.2**). Hence, this experiment could give hints to determine the nature of the molecular interactions. The stability of the molecular chains was tracked during 51 minutes. The first snapshot in **Figure 3.2(a)**, shows three small molecular chains numbered as chains 1, 2 and 3. Chain 1 is a molecular chain with only one extreme visible. Chain 2 is a complete molecular chain based on two molecular pairs. Chain 3, located at the top part of the image, is a molecular chain with four TAPT molecules. From here on, Chain 3 is taken as a model to study the process of formation of the molecular chains. The two TAPT molecules at the bottom part of the chain form a molecular pair. Whereas, the two TAPT molecules at the top part of the chain are unable to form a second pair. Their interaction (indicated by the white dashed arrow) cannot be determined by STM, but gives hints of deprotonation in the NH_2 groups. The protrusions indicated by the green arrows at both sides of the molecular chain are most likely Cu adatoms [83]. These protrusions are also seen in chains 1 and 2. This kind of metal-organic coordination can be possible if the molecules present a degree of deprotonation. At both sides of the chains, only one Cu adatom is observed attached to the TAPT molecules. The blue-colored arrows indicate the presence of Cu adatoms at the surface, which can act as a feedstock to form molecular chains. Previous works on Cu surfaces

have shown that molecules with NH_2 groups semi-deprotonate at RT [31], [32], [96], [97]. Here, the semi-deprotonation of TAPT molecules occurs when they reach the substrate due to a strong molecule-substrate interaction. Eventually, the semi-deprotonated NH_2 groups bind with Cu adatoms through metal-organic coordination [31], [32].

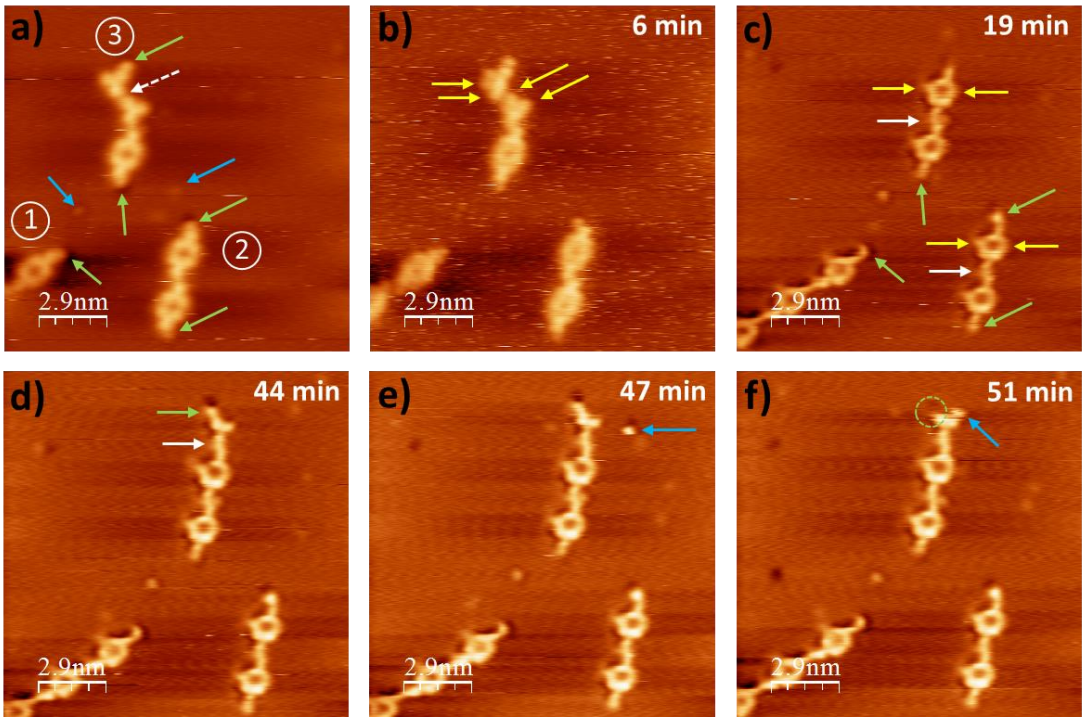

Figure 3.2: Snapshots from a time lapsed sequence of STM images for TAPT molecules on Cu(100). Three chains labelled by the numbers 1, 2 and 3 show the initial states of the formation of the 1D arrangements based on the coordination of the TAPT molecules with Cu adatoms. Solid arrows indicate the Cu adatoms. A dotted arrow in (a) indicates an interaction which is unknown. Each image was taken in a sequence of (b) 6 min, (c) 19 min, (d) 44 min, (e) 47 min and (f) 51 min after image (a).

The yellow arrows in **Figure 3.2(b)** indicate different Cu adatoms attached to the TAPT molecules at the upper part of the Chain 3. Consequently, **Figure 3.2(c)** shows that the previous coordination with the adatoms promoted the evolution of Chain 3 into a molecular chain formed by two molecular pairs. Protrusions indicated by the yellow arrows between the two TAPT molecules from the pairs correspond to Cu adatoms, which evidence a metal-organic coordination. In addition, the white arrow also indicates a Cu adatom resolved between the molecular pairs, revealing again a metal-organic coordination. The metal-organic coordination is also shown in Chain 2, with the Cu adatoms indicated by the white and yellow arrows. The green arrows at the end of the molecular chains highlight the Cu adatoms that later could coordinate additional molecules to contribute with the growth of the molecular chains. The coordination of single Cu adatoms at the three ends of each TAPT molecule (yellow, white and green arrows) evidence the semi-deprotonation of the NH_2 functional groups.

In **Figure 3.2(d)**, a Cu adatom attaches a fifth TAPT molecule on the top part of Chain 3 (white arrow). Additionally, the TAPT molecule coordinates a second Cu adatom indicated by the green arrow. In **Figure 3.2(e)** a third Cu adatom is observed approaching the molecular Chain 3, which finally coordinates (in **Figure 3.2(f)**) with the last semi-deprotonated NH_2 group available. Meanwhile, the green dashed circle shows that a previously coordinated Cu adatom left the molecule. These findings demonstrate the availability of coordination ligands in the semi-deprotonated molecules, which are required to form MONs.

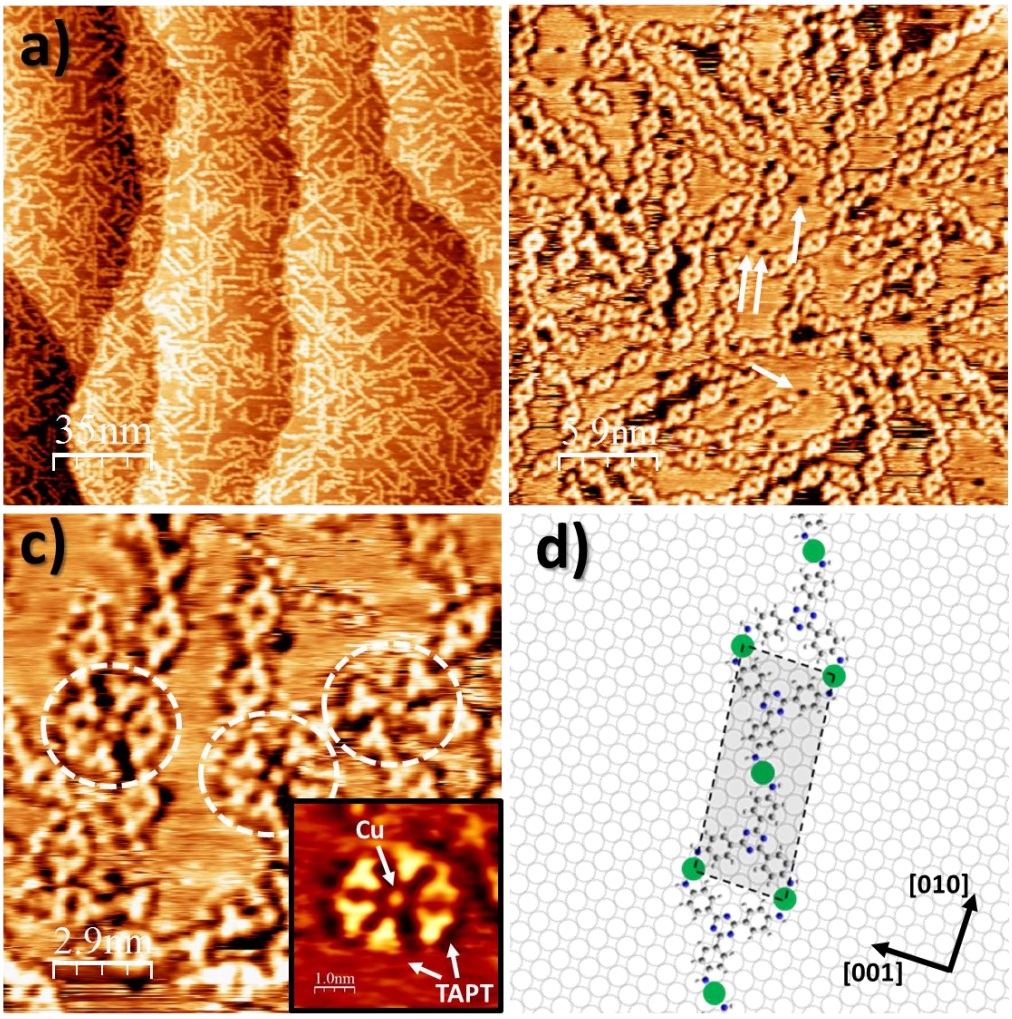

Figure 3.3: (a) Chain-like structures with a higher coverage, obtained after depositing TAPT on Cu(100). (b) The close view of the domain structure in (a) shows the 2D planar absorption of TAPT. Dark spots (as indicated by white arrows) represent the missing Cu atoms. (c) Some parts of the 1D structure collapses into 0D structures of four, five and six TAPT molecules coordinated with a single Cu adatom (dashed circles). Inset: zoomed-in image of a 6-fold coordinated Cu adatom with TAPT molecules. (d) Tentative model corresponding to the structure of the 1D chain networks. The green, blue, grey and white balls represent the Cu, N, C and H, respectively. The Cu adatoms form a metal-organic coordination with the TAPT molecules. It is considered that the NH_2 groups of TAPT are semi-deprotonated to form, thought the N sites, a coordination with Cu.

When the coverage of TAPT molecules on the surface is increased (0.5 ML), the TAPT molecules form longer 1D metal-organic chain-like structures. As with the low coverage, the chains nucleate from the step edges and from the terraces (**Figure 3.3(a)**) [85]. The zoom-in of the surface in **Figure 3.3(b)** resolves the structure of the chains, which present different lengths. Their preferential orientations follow the directionality of the N atoms. Several molecular chains converge in some points. White arrows indicate dark spots along the terraces that represent the missing Cu atoms (vacancies), found as adatoms beside the molecular chains. This shows a direct interaction of semi-deprotonated TAPT molecules with the surface [34].

The STM images from **Figure 3.3(c)** reveal the presence of metal-organic structures in a multi-fold coordination, with four, five or six TAPT molecules surrounding a single Cu adatom (white-dotted circles). This particular *n*-fold metal-organic coordination of zero-dimensional (0D) arrangements, formed by several TAPT molecules converging into a single Cu adatom, are found randomly along the surface at RT. The inset image depicts in more detail a representative six-fold structure**,** with six TAPT molecules coordinated with a single Cu adatom. The large density of TAPT molecules around the Cu adatom generates repulsive forces between the molecules, which results in large ligand-metal bond lengths (~3.0 Å) [85], compared with the small separation seen in the pairs (~2.0 Å). Surprisingly, in the 1D structure, the metal centers of Cu are not resolved clearly by STM when the coordination number of the Cu adatoms decays from six-, five- and four-fold to two-fold. This fact demonstrates the effect of the electronic resonance characteristics in STM experiments [82], [98]. That is, by decreasing the number of molecules that coordinate each Cu adatom, the electronic resonance between the states of the N and Cu atoms starts to overlap in a different fashion.

Figure 3.3(d) shows the proposed structural model of the 1D structure along the Cu(100) substrate. The structure presents a parallelogram-shaped unit cell with dimensions 10.8 x 27.1 Å, which matches with 3 and 7.5 times the lattice constant a=3.61 Å, respectively [85]. As seen by STM, this model considers the molecules lying flat on the surface. From the information obtained in **Figure 3.2**, the TAPT molecules are semi-deprotonated. Thus, the TAPT molecules from the molecular pairs present a double-joint metal-coordination between two semi-deprotonated NH_2 groups (-NH) and two Cu adatoms (2 x R-NH-Cu-NH-R). In addition, the chain is formed when two molecular pairs bind in a 1D arrangement with a lateral offset between each other. The bond is made through a third Cu atom coordinated via the N site from the third NH group left (R-NH-Cu-NH-R) in the TAPT molecules from each molecular pair. The lateral offset is due to the directionality of the bonds given by the coordination geometry of N that forms bonds at 120°. The metal-organic length (N-Cu) is estimated around 2.0 Å, in agreement to a moderate metal-organic interaction [17], [85]. In this model, the Cu adatoms that form the metal-coordination in the molecular pairs, lie into the most energetically favourable place: the hollow sites in the Cu lattice [82], [99]. Whereas, the Cu atoms responsible to link the pairs are found bridging two Cu atoms from the substrate lattice.

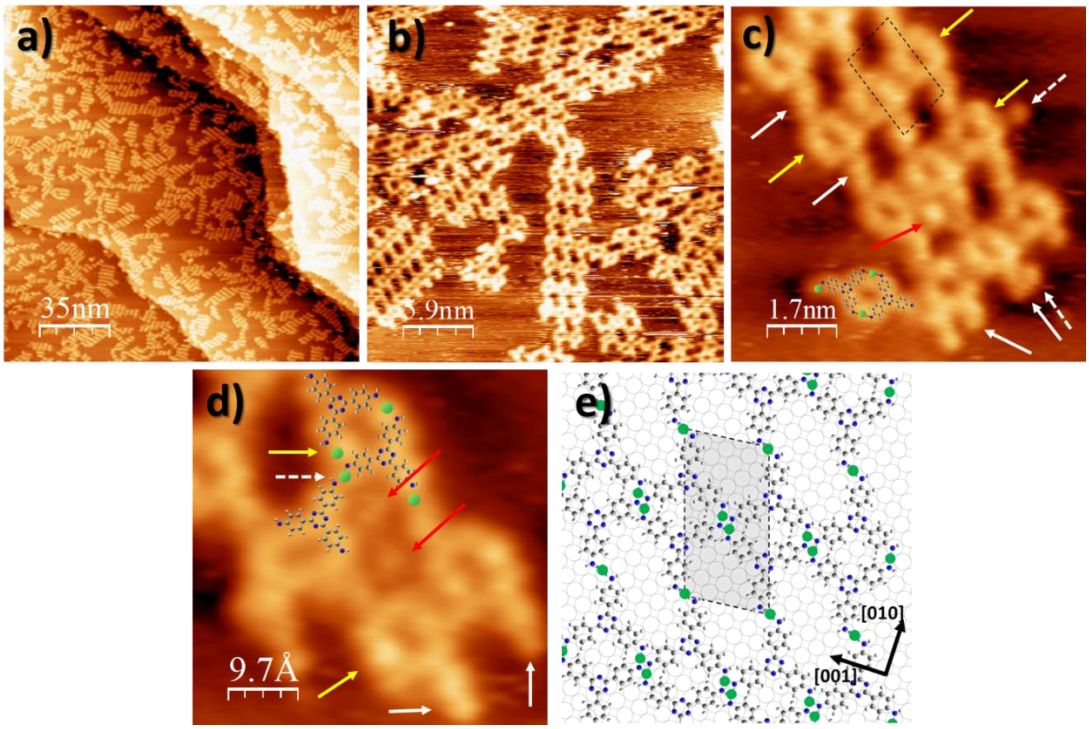

Figure 3.4: (a) Overview STM image that shows braid-shaped structures along the Cu terraces, formed after annealing at 533 K. (b) The braid-shaped MONs are the result of the coupling of several 1D chains. (c)-(d) The protrusions indicated by the yellow and white arrows correspond to the Cu adatoms acting as metal centers. The small features inside the pores (indicated by the red arrows) suggest the potential of these networks to work as trap sites for molecules or atoms. (e) Tentative model corresponding to the structure of the 2D MONs. The green, blue, grey and white balls represent the Cu, N, C and H, respectively. The dotted parallelogram represents the unit cell. The Cu adatoms form a metal-organic coordination with the TAPT molecules. Each TAPT molecule presents two semi-deprotonated NH_2 groups; each group forms a monodentate coordination with a Cu atom. A third NH_2 group is fully deprotonated and forms a bidentate coupling with two Cu atoms. The bidentate coordination is responsible of the lateral coupling between the molecular pairs from several 1D chains.

The 1D MONs were soft annealed at 533 K during 10 minutes. Surprisingly, a 2D compact structure based on rectangular braid-shaped patches appears across the terraces (**Figure 3.4 (a)**). The zoom-in (**Figure 3.4 (b)**) reveals the rhombic-shaped features based on the molecular pairs, as found in the 1D chain-like structure. It also reveals that the 2D structure is based on the coupling of several 1D metal-organic chains. A detailed analysis in **Figure 3.4 (c-d)** shows that the 2D structure is also based on the metal-organic coordination between TAPT molecules and Cu adatoms. The white and the yellow arrows indicate the presence of Cu adatoms that participate in the metal-organic coordination. The yellow arrows show the Cu adatoms between the pairs. As observed in the 1D structures, the lateral offset between two molecular pairs is an indication that the semi-deprotonation of the NH_2 groups persists (white arrows). On the other hand, additional adatoms coupled to both sides of the NH_2 groups in some molecules (indicated

by the white-dashed arrows) give hints of complete a deprotonation. The 2D structure also presents a lateral coupling between the molecular pairs. As it is discussed below, this is only possible considering the complete deprotonation in one of the NH_2 groups from the TAPT molecules involved in the double-joint metal-organic coordination of the pairs. In addition, the arrangement between molecules and adatoms in the 2D structure forms pores. In some pores contain protrusions with different contrasts, probably related to trapped Cu adatoms [37].

Figure 3.4 (e) presents the tentative structural model of the 2D structure on a Cu(100) substrate. The structure presents a parallelogram-shaped unit cell with dimensions 14.4 x 26.3 Å, which match with 4 and 7.3 times the lattice constant (a=3.61 Å), respectively [85]. The model shows the persistence of the semi-deprotonated -NH groups, as seen in the 1D structure. However, this model also implies a complete deprotonation in one of the amino groups to allow the lateral coupling between the molecular pairs. The coupling is made between two TAPT molecules from two different pairs through a metal-organic coordination between four fully deprotonated amino groups and two Cu adatoms (green circles). The average metal-organic lengths are estimated to be around 2.0 Å, as in the case of the 1D structure.

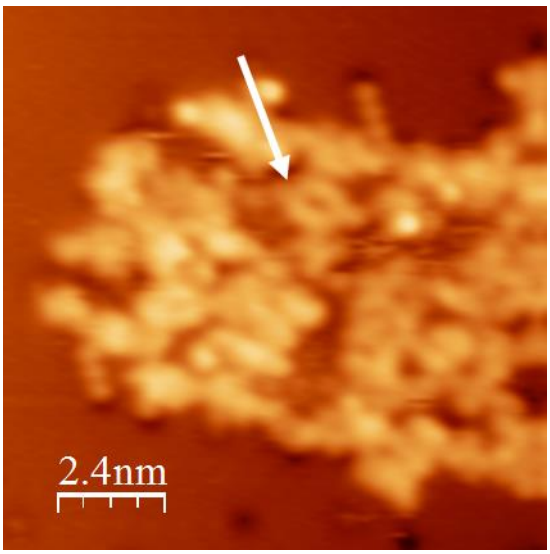

Figure 3.5: STM image of a disordered structure obtained after the post-annealing of the 2D braid-shaped metal-organic network at 573 K. The full-deprotonation of the molecules may prevent the formation of an ordered structure. The white arrow indicates a molecular pair remaining as an indication of the stability of the two-fold coordination.

There are some previous works related to changes in reactivity/structures triggered by post-annealing treatments. For example, Rodríguez-Fernandez et al. [100], show how the metal/ligand stoichiometric ratio in a metal-organic network is adjusted by the temperature of the substrate during deposition of tetracyanoethylene (TCNE) molecules on Ag(111), instead of depositing different relative amounts of metal/ligand [29]. Also, Lin et al. [101], showed that the deprotonation of COOH groups is catalyzed by an increment of the temperature of co-deposited TMA and Cu adatoms on Ag(111); and Steiner et al. [102], showed the formation of metal/ligand structures after annealing NH_2-terminated molecules on Cu(111) samples. Nevertheless, none

of these works shows the transition between two well-defined 1D to 2D structures by tuning the reactivity of the ligands and metal adatoms with the temperature of the sample. The 1D metal-organic chains have shown to have a stable structure and the Cu adatoms involved in the 2-fold coordination that form the molecular pairs, present a different electronic environment than the ones involved in the chain-like coupling of the pairs. It has been also been reported that post-annealing at moderate temperatures promotes the mobility of Cu adatoms to form metal-organic coordination networks [102]. Therefore, it is proposed that the complete deprotonation in one of the NH_2 groups would be triggered by the proximity of the Cu adatoms from different 1D metal-organic chains. Thus, the change in the electronic environment promoted by post-annealing treatment gives rise to the formation of 2D structures.

On the other hand, the further post-annealing at 573 K generated the fully-deprotonation of the remaining NH_2 groups. Consequently, the 2D structure experiences a structural dissociation and the metal-organic network finally collapses **(Figure 3.5**).

3.2.1. CO_2 and O_2 Gas injection on the Cu-TAPT networks

As seen above, the partial and complete deprotonation of the NH_2 groups of TAPT molecules allows the metal-organic coordination with Cu adatoms. In the 2D structures, the semi- or fully deprotonated NH_2 groups may expose free electron pairs. Therefore, CO_2 is introduced into the system to study its possible absorption on the Cu centers or on the deprotonated NH_2 groups as an attempt to form carbamates.

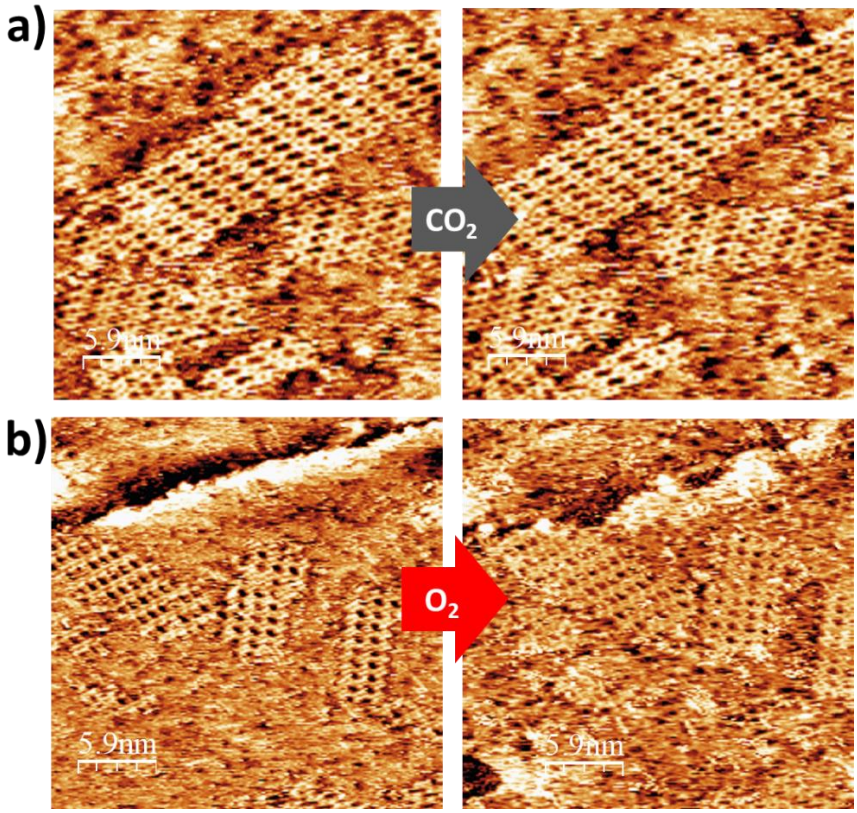

Figure 3.6: The 2D rectangular braid-shaped networks do not show incorporation neither structural changes after being exposed to 500 L of (a) CO_2 and (b) O_2.

After exposing 500 L of CO_2, the 2D structure did not show any signs of CO_2 incorporation (**Figure 3.6(a)**). To study the reaction of the MONs with other gases, a different sample with 2D networks was dosed with 500 L of O_2. However, as in the previous case, the structure of the networks remained unchanged (**Figure 3.6(b)**). Thus, no evidence of gas adsorption could be collected from the STM images since CO_2 and O_2 were neither incorporated nor promoted a structural change in the 2D networks.

3.2.2. Incorporation of Mg in Cu-TAPT networks

Inspired by the Mg^{2+} center found in the active site of RuBisCO, the effect of incorporating Mg into the structure of the metal-organic TAPT-Cu networks, was investigated. The main goal is to attempt the formation of a coordination network of TAPT molecules with a Mg center which could promote the CO_2 adsorption. Another possibility, involves the incorporation of Mg atoms on the TAPT-Cu to form bi-metal-organic structures with Mg and Cu centers, which consequently could present catalytic activity towards CO_2 [103].

Sub-monolayer coverages (<< 1 ML) of Mg atoms were deposited by thermal evaporation on a Cu(100) surface. A mild post-annealing at 353 K followed the deposition of Mg. The process continued with the co-deposition of 0.5 ML of TAPT molecules, using the same conditions to form the 1D MONs presented in the first section.

The STM images showed clusters of Mg of around 3 nm in diameter (a detailed analysis of the Mg clusters on Cu(100) will be discussed in Chapter 4). The clusters are visible as white protrusions along the surface (as indicated by the blue arrows). The STM images did not show the formation of ordered structures with Mg. TAPT molecules spread on the surface with an irregular fashion. Some molecules form molecular pairs (double-joint interconnection) and a few connect to form 1D chains (dashed circles). The presence of TAPT pairs evidences that TAPT semi-deprotonates and still prefers to bond with Cu adatoms. Nevertheless, long 1D metal-organic chains are not observed on the surface, suggesting that the molecules may also interact with the Mg atoms. Even though the STM images did not show a new ordered structure which could result from the self-assembly between Mg and TAPT; the structural dissociation is a strong evidence that Mg interacts with the TAPT molecules. The reason of the dissociation is still unclear. A proposed explanation resides in the indiscriminate coordination of TAPT molecules with both Cu and Mg atoms. The double-joint interconnection between the two TAPT molecules in the molecular pairs seems to be stronger than the single N-Cu-N coordination that takes place between two pairs. Thus, considering a small metal-organic chain formed with only two molecular pairs coordinating a Cu adatom, it is believed that Mg induces a weakening in the single N-Cu-N coordination between two pairs. As a result, one pair remains bonded to a Cu adatom, while the second one would bind a Mg atom. Consequently, the tendency of semi-deprotonated TAPT to form a bi-metallic coordination with the Cu and Mg atoms could prevent the evolution of an ordered structure. Although an ordered structure was not formed, the disordered system was dosed with 500 L of CO_2 to study the role of the Mg atoms as adsorption centers. The STM images did not give any structural evidence of CO_2 adsorption (image not shown here).

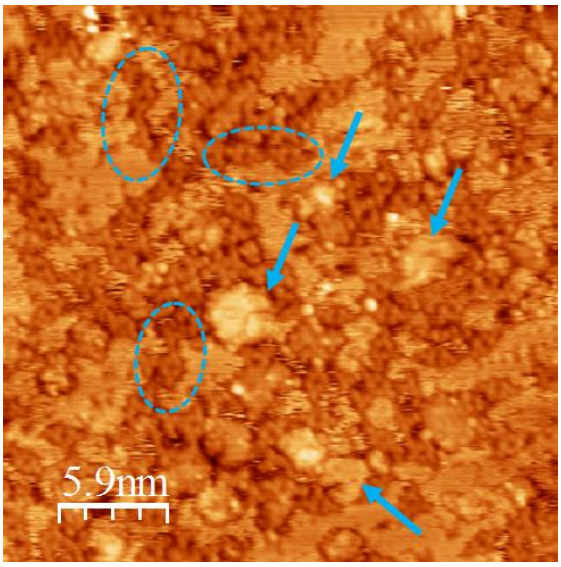

Figure 3.7: a) The co-deposition of Mg atoms with TAPT molecules did not result in an ordered structure. Clusters of Mg are spotted along the surface as white protrusions (indicated by the blue arrows).

These results suggest that TAPT molecules show their ability to form MONs with the Cu adatoms from the host substrate. However, on Cu(100), Mg is not a good candidate to form highly-ordered MONs with molecules bearing semi-deprotonated NH_2 functionalities. The presence of Mg prevents the formation of MONs with bi-metallic centers and even interferes in the formation of 1D MONs of Cu-TAPT (**Figure 3.7)**. In addition, the interaction of Mg with TAPT molecules, sparks the interest to study the deposition of TAPT molecules on a Mg(0001)surface.

3.3. TAPT on Mg(0001)

As it was shown above, TAPT molecules form MONs with the adatoms from the host Cu(100) substrate. However, in the presence of Mg atoms, the structure disassembles and collapses forming irregular arrangements. Therefore, as an attempt to form the first MONs with Mg, sub-monolayer coverages of TAPT molecules were deposited on an atomically clean substrate of Mg(0001). As seen with Cu(100), the adatoms from the Mg(0001) substrate could coordinate with the molecules to form MONs. To the best of our knowledge, there is no information regarding to molecules deposited on Mg single crystals. Thus, the lack of previous information concerning the interaction of the triazine ring and NH_2 functional groups with Mg atoms makes these experiments challenging. To identify the interactions of these chemical groups on Mg, STM and HR-XPS measurements were performed to reveal the structural and chemical configuration of TAPT molecules on the Mg(0001) surface at RT.

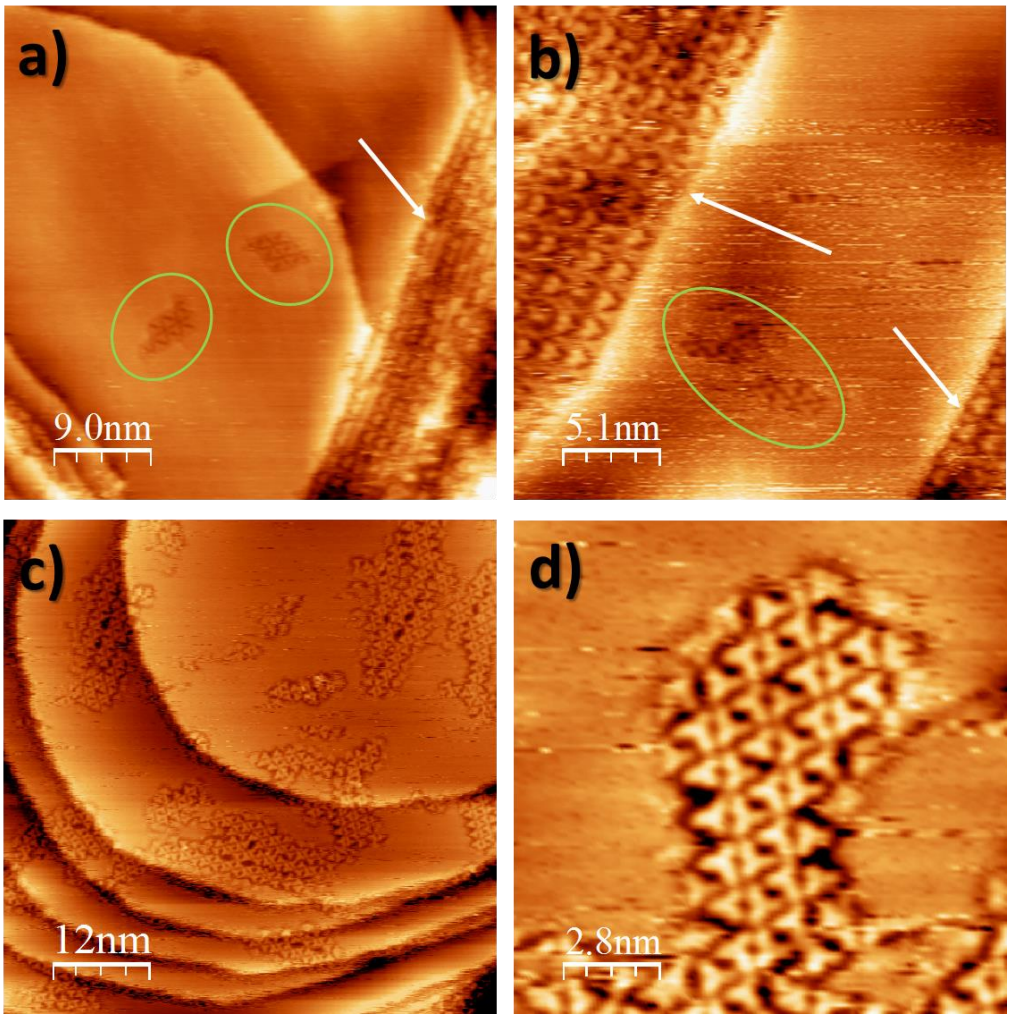

Figure 3.8: (a) TAPT molecules on Mg(0001), lying on the terraces (highlighted by the green circles) and in the step edges (indicated by the white arrows). (b) The TAPT molecules arrange along the step edges. (c) Increasing twice the deposition time of the molecules while the substrate is kept at 353 K, increases the molecular coverage on the surface. Even with a high coverage, the step edges do not get fully decorated with molecules, but larger networks grow across the terraces. (d) A typical structure showing a compact arrangement of the TAPT molecules on the Mg(0001) terraces.

TAPT molecules were deposited on Mg(0001), with the same conditions used above to obtain 0.5 ML of TAPT on Cu(100). Thus, **Figure 3.8(a))** identifies a large area of bare surface, with some TAPT molecules decorating the step edges (white arrow) or self-assembled in small 2D structures on the terraces (green circle). A closer inspection on the step edges (**figure 3.8(b)**) reveals the interconnection of the molecules with a linear periodicity, forming molecular chains along the step edges. Even though the same deposition conditions to obtain 0.5 ML on Cu(100) was used, the lower coverages (< 0.1 ML) of molecules on Mg(0001) suggests that the substrate presents a weaker interaction with these molecules. To increase the molecular coverage on the terraces, TAPT molecules were deposited by longer periods of time; the deposition period was increased

by 2 times. In addition, during deposition, the temperature of the Mg single crystal was increased to 353 K to enhance the thermal mobility of the molecules through the surface. This thermal treatment increases the density and the diffusion of adatoms across the surface. As a result, **Figure 3.8(c)** shows bigger areas of TAPT molecules on the terraces. However, the step edges are still not fully decorated with TAPT molecules and present fuzzy lines in areas without adsorbed molecules due to the adatoms' mobility. A closer inspection on the terraces (**Figure 3.8(d))** reveals that TAPT molecules are absorbed in a 2D planar geometry, with their backbones parallel to the surface, as the tentative model shall explain it.

Figure 3.9(a) shows the most repetitive structural conformation of TAPT molecules on terraces of Mg(0001). The growth of the networks on the middle of the terraces may indicate the coordination of TAPT molecules with mobile free adatoms from the surface. Because of steric impediment, triazine (-N=) N atoms of planar TAPTs molecules may not interact with fully (or semi) protonated amino groups (-NH_2/-NH) of neighboring TAPTs. Thus, their self-assembly is different than the molecular interaction between melamine [104] or heptazine [105] molecules adsorbed on Cu(001) and Au(111), respectively. According to the geometrical distribution of these TAPT molecules on the surface, there may exist H-bond interactions between the amino groups and Hs from the phenyl rings. Therefore, it is believed that amino groups are semi-deprotonated (-NH) under this deposition conditions (**Figure 3.9 (b)**). On the other hand, from **Figures 3.8 (d)** and **3.9 (a)**, at first glance it could be considered that four TAPT molecules interact by the amino groups (and other two by H-bonds with the phenyl ring). According to the geometry of adsorption (and considering the planarity of these molecules), a Mg adatom should be present in the middle of these four molecules. The tentative model shown in **Figure 3.9(b)**, suggests the formation of what to our knowledge represents the first metal-organic network reported on Mg(0001). The structure is based on the bi-coordination of Mg adatoms with the semi-deprotonated -NH_2 group of two TAPT molecules while the other two species are linked with H-bonds. The average distance of the H-bonds between N atoms from semi-deprotonated amino groups and H atoms from adjacent phenyl rings is 1.95 A; in agreement with previous works [20]. In addition, the NH groups out of the metal-organic center form also H-bonds with the phenyl rings from the adjacent molecules. According to the interactions depicted in the unit cell (green triangles), each semi-deprotonated TAPT molecule contains three different amino environments at each corner: one metal-organic coordination and two kind of inequivalent H-bonds (one close to a metal-organic center and the other forming a H-bond far from the metal-organic center). To prove the presence of adatoms in the network, an exploration of different areas (**Figure 3.9(c)**), such as domain boundaries where 2 structures collapse, shows the presence of adatoms trapped inside the pores formed between 2 incomplete unit cells (white-colored circle). Thus, these pores could also act as trapping sites for molecules or adatoms.

In contrast to the 1D chain-like structures formed on Cu(100), STM images revealed that the metal-organic coordination between TAPT and Mg results in the formation of 2D structures on Mg(0001). This could be related to the lower reactivity of the substrate with the molecules which results in the enhancement of supramolecular interactions [32], [102]. The lower reactivity of the substrate was evidenced by the longer deposition times compared to that employed on Cu(100).

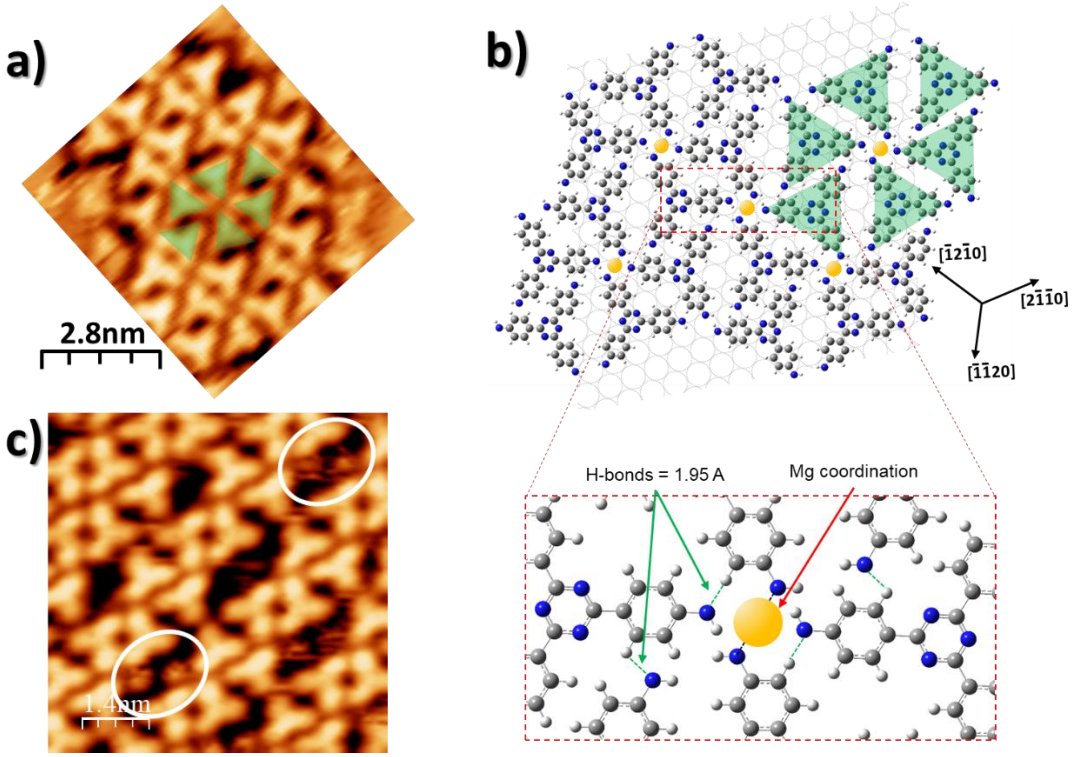

Figure 3.9: (a) The TAPT molecules form a compact structure on the Mg(0001) terraces, different to the typical chain-like structure formed Cu(100). (b) The proposed model shows a metal-organic network of TAPT molecules coordinating Mg adatoms sequestrated from the surface. The unit cell is highlighted by the six green triangles and presents semi-deprotonated molecules forming a metal-organic coordination with a Mg center and H-bonds with the adjacent molecules. (c) The incomplete unit cells form pores which can act as trapping sites for molecules or adatoms

In order to corroborate the results obtained by STM images, in this section, HR-XPS was used to identify the chemical states of the molecules adsorbed on the surface. **Figure 3.10** shows the HR-XPS spectra, focused on the N1s and C1s binding energy regions, of a sample prepared with the same deposition conditions described above (with an additional thermal treatment at 353 K). As it was described before, the chemical structure of TAPT molecules before adsorption consists of two different types of N atoms, one related to the NH_2 group and the other related to the triazine ring (-N=). Therefore, in an ideal experiment the N1s region of TAPT molecules would present only two peaks in a 1:1 ratio. A similar experiment carried out for melamine molecules in multi-layers, the molecules from the top-most layer present two peaks at around 400.0 and 399.1 eV, respectively [96], [106], [107]. Nevertheless, when triazine rings adsorb planar on metallic surfaces [107]–[109] the peak attributed to –N= atoms shifts to lower binding energies (at around 398.2 eV). Therefore, the prominent peak at 398.1 eV (**N1**) (**Figure 3.10(a)**) is attributed to the N atoms from the triazine ring of TAPT molecules (blue circles in **Figure 3.10(a)**) adsorbed on the surface [96], [110]. As it was expected, this peak represents almost the 50% (precisely 46 %, see Table 1) of the total amount of N atoms; implying that almost all the

molecules lie planar with their backbones parallel to the substrate. Thus, the 50% left should belong to the N atoms from the amino (NH_2) groups. The information from literature indicates that the partial deprotonation of the NH_2 groups and interaction with a metallic surface lowers its binding energy and, further coordination with metal adatoms, generates a peak at even lower binding energies [96]. Accordingly, the peak at 397.1 eV (**N2**) is attributed to the metal organic coordination of Mg adatoms with semi-deprotonated NH_2 group (-NH-Mg, violet circles in **Figure 3.10(a)**). This peak possesses a percentage area of 17% indicating that one third of the total N available from the NH_2 species is coordinated to Mg adatoms. The best fitting of the N1s spectrum, contains two more peaks at 399.4 eV (**N3**) and 400.0 eV, (**N3'**) representing the 22% and 14% of the total amount of N atoms, respectively. According to the tentative model presented in **Figure 3.9(b)**, where four types of N environments were found, these peaks are attributed to semi-protonated amino groups (adsorbed on the surface) interacting by H-bonds with an adjacent aromatic ring (red and green circles in **Figure 3.10(a)**). The small difference of 0.6 eV between these peaks could be attributed to the slightly different environments of these semi-deprotonated amino groups forming a H-bond near the metal-organic center. As described above in the case of melamine molecules, the peaks attributed to the three N atoms from the triazine ring (-N=) and fully protonated amino groups which do not interact with the surface are located at around 399.1 eV and 400.0 eV [96], [109], [111]–[113]. Thus, if some free TAPT molecules remain on the surface after annealing, the proportion of **N3** and **N3'** should be altered. Therefore, errors in the exact composition of the different species on the surface obtained by the analysis of the HR-XPS spectrum could be attributed to the fitting procedure and, also to the presence of fully protonated physisorbed species as contaminants. Nevertheless, taking into account that although the tentative theoretical model inspired in the STM images proposed an ideal N composition of **3:1:1:1**, the relative proportional areas (**N1:N2:N3:N4**) obtained after fitting the HR-XPS spectra is **2.8:1.0:1.3:0.9**; in good agreement with the values expected from the model.

On the other hand, considering the C atoms in free TAPT molecules, an ideal C1s spectrum should contain 4 peaks (depending on the resolution of the analyzer): **C1**, belongs to the C1s transition of the 12 equivalent C atoms in the middle of the 3 phenyl rings (yellow circles in **Figure 3.10(b)**); **C2**, 3 C atoms in the phenyl rings directly bonded to the C atoms from triazine ring (green circles in **Figure 3.10(b)**); **C3**, 3 C atoms in the phenyl rings directly bonded to the semi-deprotonated amino groups (red and brown circles in **Figure 3.10(b)**); and **C4**, the 3 C atoms in the triazine ring (cyan circles in **Figure 3.10(b)**). Therefore, the ideal proportion of the C1s peaks **C1:C2:C3:C4** should be **4:1:1:1**. However, in the theoretical model one semi-protonated amino group is coordinated with Mg while the other two with H-bonds. Hence, the **C3**-feature of an ideal spectrum should be divided into two sub-features: **C3** (brown circles in **Figure 3.10(b)**) and **C3'** (red circle in **Figure 3.10(b)**) with a **0.33:0.66** relative composition. Thus, according to the theoretical model, the relative composition of C atoms should be **4:1:0.66:0.33:1**. The best fitting of C1s spectrum of the same sample is shown in **Figure 3.10(b)**, where 4 peaks with a relative composition of **3.6:1.3:0.8:0.6:0.8** is obtained. Again, the agreement with the composition in the theoretical model is reasonable, considering the presence of non-adsorbed species on the surface and uncertainties in the fitting procedure.

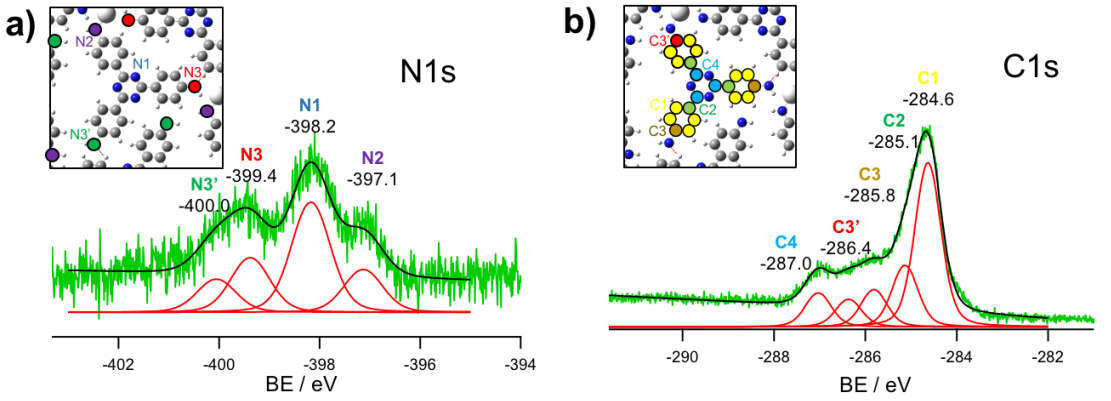

	N1	N2	N3	N3'
Theoretical model	3	1	1	1
HR-XPS	2.8	1.0	1.3	0.9

	C1	C2	C3	C3'	C4
Theoretical model	4	1	0.66	0.33	1
HR-XPS	3.6	1.3	0.80	0.59	0.8

Figure 3.10: HR-XPS spectra in the (a) N1s and (b) C1s region for TAPT molecules deposited on a Mg(0001) substrate after annealing at 353 K. In the insets, the different kinds of N and C atoms of the model are depicted by circles with different colors. The tables at the bottom show the comparative relative composition of every specie.

A new experiment was performed under the same deposition conditions but without heating the substrate (at 353 K), to analyze the effect of a thermal treatment with the composition of the species on the surface. Within this experiment, the change in the proportion of the peaks could help in the corroboration of the adsorbed species. **Figure 3.11** shows the N1s spectra before **(a)** and after **(b)** thermal treatment, where the changes in the composition is followed by the change in the relative composition of every feature **(c)**.

Figure 3.11 shows that the **N1** feature remains almost constant after annealing. Thus, it can be interpreted that the amount of TAPT molecules adsorbed on the surface is the same before and after annealing. Nevertheless, there is an increment in the signal attributed to semi-protonated amino groups coordinated with Mg (**N2**) by 2% and a decrease in the signal **N3'**. As it was described above, the **N3** and **N3'** signals are in the region of binding energies where the N1s transition of weakly adsorbed or fully deprotonated species takes place. Therefore, it can be concluded that the process of annealing at 353 K induces the semi-deprotonation of amino groups and consequently the formation of metal-organic coordination.

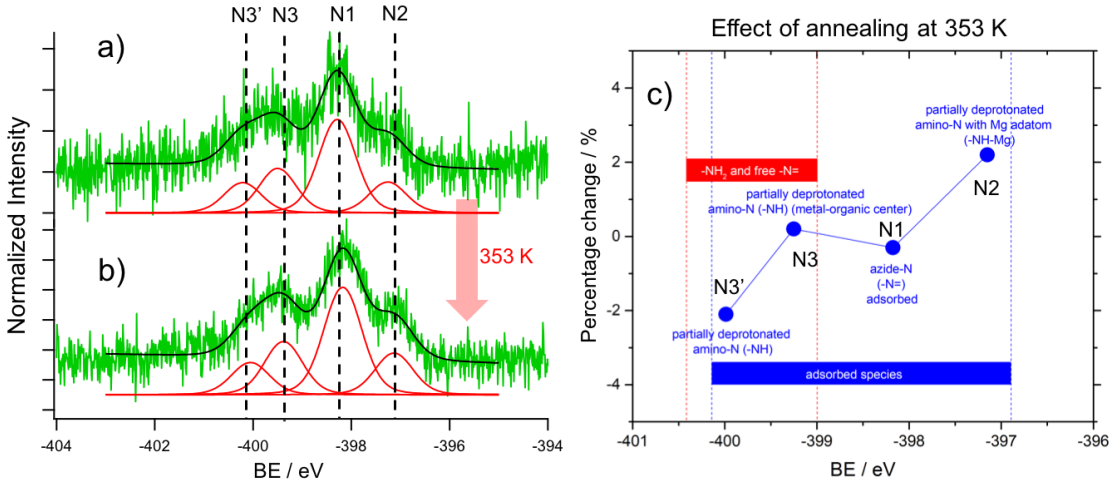

Figure 3.11: HR-XPS spectra in the N1s region, corresponding to the interaction of TAPT molecules deposited on a Mg(0001) substrate (a) before and after (b) annealing at 353 K. (c) Graph showing the variations in the relative percentage area of the peaks at each binding energy. The blue line shows the direct effect of the annealing on the system based on TAPT molecules on Mg(0001).

From the observations above, it can the concluded that the deposition of TAPT molecules on Mg(0001) at RT, generates the semi-deprotonation of the NH_2 groups; in agreement with previous studies of molecules with NH_2 groups semi-deprotonated in different surfaces at RT [114]–[117]. The semi-deprotonation promotes the metal-organic coordination of TAPT molecules with the Mg adatoms from the host substrate and could be improved by a subsequent annealing of the surface at 353 K.

3.3.1. CO_2 Injection on the Mg-TAPT networks

The formation of MONs on Mg(0001) opens new avenues in the challenge of mimicking the RuBisCO active center. Here, the Mg-TAPT coordination mimics the amino environment given by the Lysine molecules around the Mg center. To investigate the reactivity of the bioinspired networks, the analysis of the CO_2 interaction was performed by HR-XPS and STM experiments under UHV conditions.

Figure 3.12 (a-b) shows the photoemission spectra in the N1s region before (a) and after (b) the interaction of TAPT molecules on Mg(0001) sample with CO_2. After CO_2 exposure (red-colored spectra), the peak **N3** attributed to the N atoms in semi-deprotonated NH_2 groups forming H-bonds on the vicinity of the metallic center, shifts slightly to lower binding energies (-0.3 eV) and its intensity decreases by almost 8% compared with the same peak before CO_2 exposure (see **Table 3.1**). This would be related to the disassembly of TAPT molecules from the network structure, evidencing their reactivity with CO_2. Indeed, this is an indication that the semi-deprotonated NH_2 groups near the active metal-organic center are more reactive to the presence of CO_2 than the rest of the network. In fact, the amount of triazine N atoms (**N1**) related

to the presence of TAPT molecules adsorbed flat on the surface, is almost invariant after the interaction of CO_2 with the network. In addition, the injection of CO_2 promotes also a slight increment by 2.4% of the **N2** component, assigned to –NH-Mg coordination (peak at 397.1 eV). However, the most noticeable change (together with the decrease of **N3**) in the composition of the different N environments derived from the assignation of every peak in the HR-XPS spectrum, is an increment by almost 8% of the **N3'** feature (**N4** after CO_2 interaction). Despite before CO_2 exposure, the **N3'** component has been attributed to semi-deprotonated amino groups interacting with H-bonds from adjacent phenyl rings, the increment of this peak and the shift to lower binding energies (-0.25 eV) is consistent with the possible formation of carbamates species (R-NH-CO_2) after CO_2 exposure. This assignment is in complete agreement with previous studies on the interaction of CO_2 with amines adsorbed on a copper surface [52]. The changes in the percentage values at each binding energy, related to the effect of the incorporation of CO_2 in the system, are shown and summarized in **Figure 3.12(c)** and in **Table 3.1**, respectively.

Table 3.1: HR-XPS peak positions and their relative areas for TAPT molecules on Mg(0001), before and after annealing or after CO_2.

Peak assignation	**TAPT on Mg(0001) before annealing**		**TAPT on Mg(0001) after annealing**		**TAPT on Mg(0001) after CO_2**	
	BE (eV)	**Rel. area (%)**	**BE (eV)**	**% change**	**BE (eV)**	**% change**
N2 (-NH-Mg)	397.2	15.6	397.1	2.2	397.1	2.4
N1 (-N=)	398.3	46.9	398.2	-0.3	398.2	-2.2
N3 (-NH···H)	399.4	22.3	399.4	0.2	399.1	-7.7
N3' / **N4** (-NH···H) / (-NH-CO_2)	400.1	15.2	400.05	-2.1	399.8	7.5

The presence of carbamate species could also be followed by the presence of a peak at around 289 eV in the C1s binding energy region. Because of the experimental conditions and the number of carbamates species compared with the total amount of C-containing species, this new feature could not be detected in the spectrum taken after CO_2 exposure (not shown here). Nevertheless, after CO_2 injection, the O1s binding energy region detected a new component together with the presence of **O1** peak assigned to spurious O_2 adsorption (**Figure 3.12 (d)**). This new feature (**O2**) should be associated to the 1s transition of O atoms from carbamates on the surface, in agreement with previous works [52].

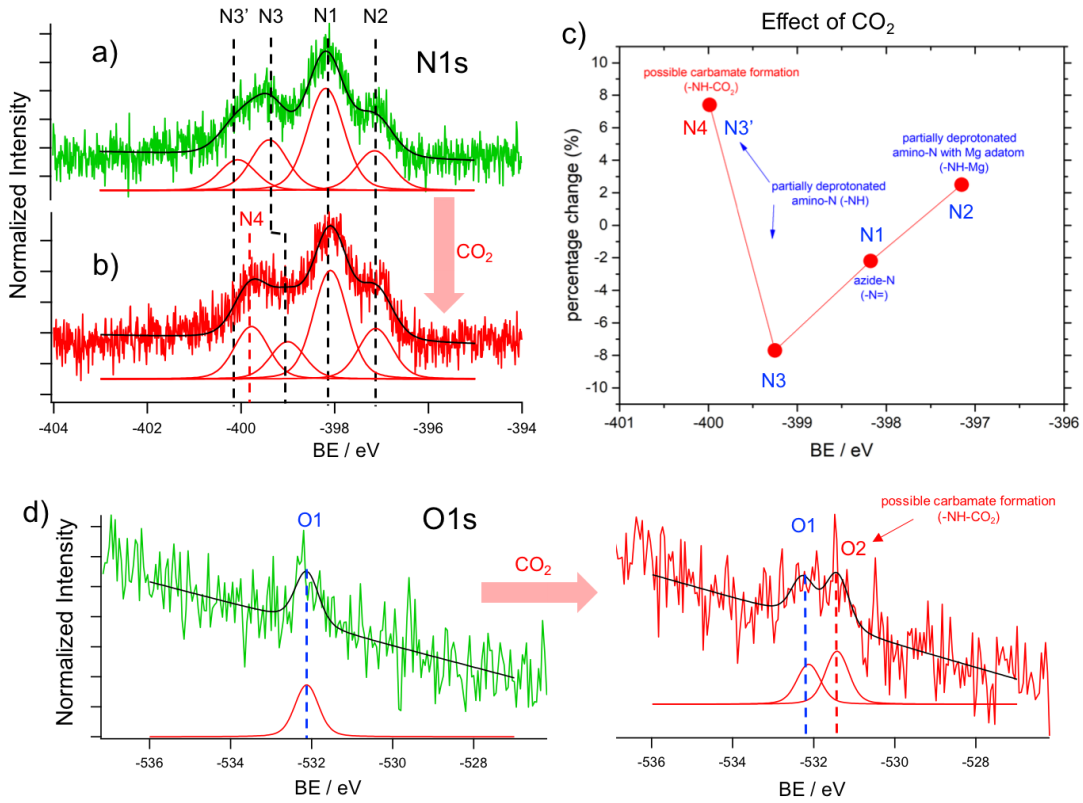

Figure 3.12: A comparison of the HR-XPS spectra in the N1s region of TAPT molecules deposited on Mg(0001) (a) before and (b) after CO_2 exposure. (c) Graph showing the variations in the relative percentage area of the peaks at each binding energy. The red line shows the direct effect of CO_2 on the system based on TAPT molecules on Mg(0001). (d) A comparison of the HR-XPS spectra in the O1s region of TAPT molecules deposited on Mg(0001) before (green) and after (red) CO_2 exposure.

The interaction of the TAPT-Mg networks with CO_2 was also analyzed by STM images (**Figure 3.13(a)**). Before CO_2 exposure, the metal-organic structure of four TAPT molecules coordinating the Mg center is observed. However, after CO_2, the STM images confirm that CO_2 promotes the disassembly of some TAPT molecules from the network. The molecules change their orientation and show the tendency to form chain-like structures, similar to the 1D networks formed on Cu(100). In **Figure 3.13(b)** the proposed scheme shows how the interaction of CO_2 with the Mg centers unbinds the H-bonds near the metal-organic coordination center, rearranging the structure into a different configuration. This model agrees very well with the analysis of the results provided by HR-XPS measurements in **Figure 3.12** and with the STM images shown in **Figure 3.13(a)**.

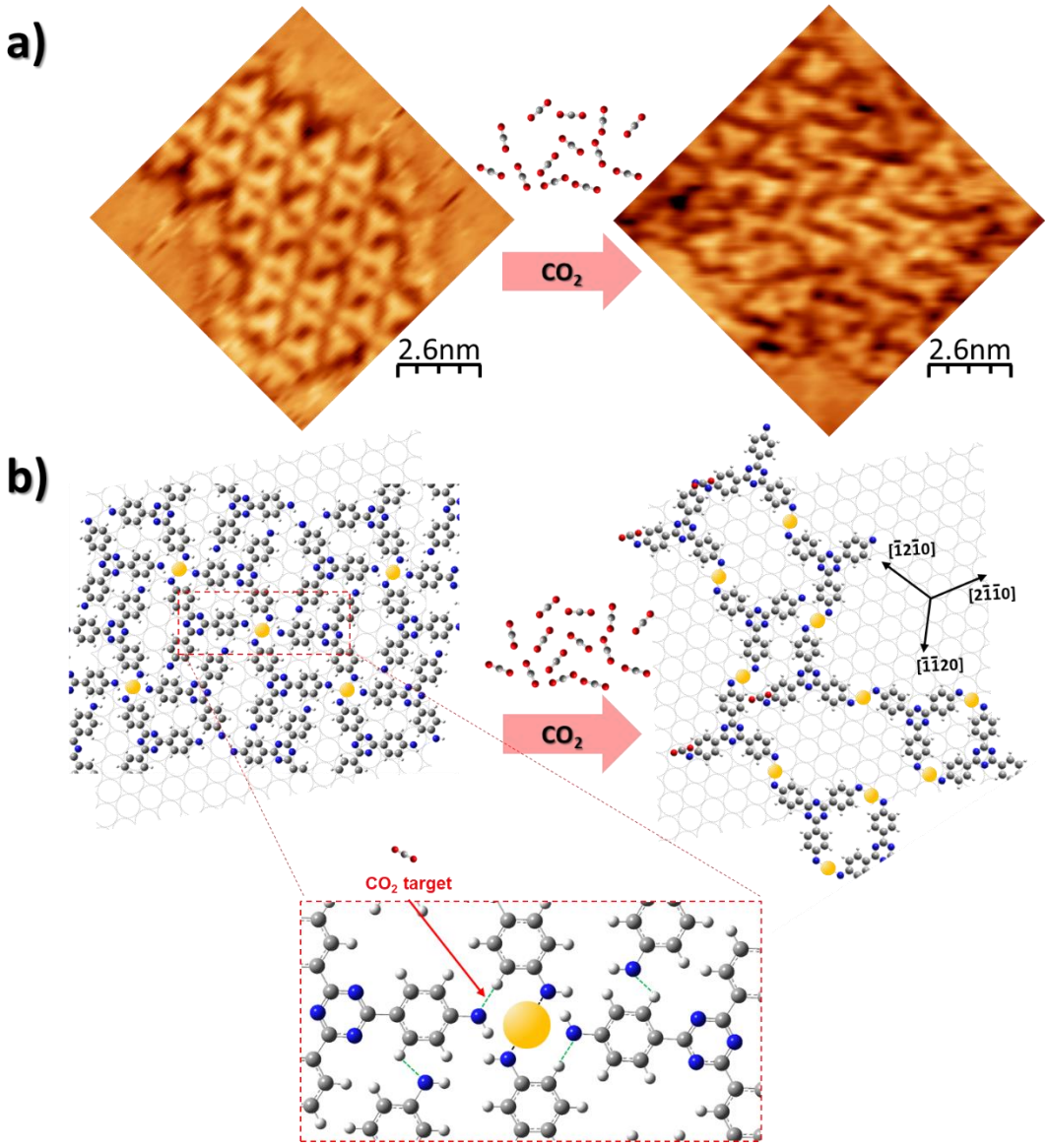

Figure 3.13: (a) STM images of TAPT molecules deposited on Mg(0001) showing the reordering of molecules into a chain-like structure as the result of their exposure to CO_2. (b) Proposed scheme of the structural evolution of the networks when CO_2 is incorporated. The inset at the bottom shows in detail the H-bond that is broken to allow the adsorption of CO_2 on the N from the semi-deprotonated NH_2 group. This scheme suggests the formation of carbamates and is supported by the XPS and STM experiments.

These results suggest that the interaction of CO_2 with the Mg-TAPT network can form carbamate species, as analogs of the carbamate of lysine in the active site of RuBisCO. Thus, these findings are a crucial step towards a 2D mimic of the RuBisCO active center.

3.4. Conclusions

In summary, this chapter presents a simple preparation method to fabricate MONs through the deposition of TAPT molecules on atomically clean surfaces of Cu(100) or Mg(0001), under UHV and at RT.

When TAPT molecules are deposited on Cu(100), the surface contributes to semi-deprotonate the NH_2 groups of the molecules. Thus, the adatoms on the surface coordinate the semi-deprotonated NH_2 groups to form 1D MONs. At higher coverages, some parts of the metal-organic chains show n-fold coordination of molecules around a Cu center. In addition, a thermal post treatment at 353 K promotes the complete deprotonation in one of the NH_2 groups of TAPT molecules, thus reorganizing the structure from a 1D to a 2D conformation. Theoretical models propose that Cu adatoms act as single and double metal centers in the 1D and 2D structures, respectively. The 2D network shows an appreciable thermal stability with (an extra) post annealing up to 533 K. Higher annealing temperatures (573K) lead to the full deprotonation of the molecules with the dissociation of the structure. The 2D MONs did not show any evidence of gas adsorption. The introduction of CO_2 or O_2 did not trigger any change in the structure of the networks. Nevertheless, this is not conclusive and future experiments using XPS could reveal other interactions which may have not been clearly perceived by STM.

On the other hand, Mg is not a good candidate to promote the formation of MONs with TAPT on Cu(100). The reason could be related to the presence of Cu adatoms that tend to form MONs with TAPT. Nevertheless, TAPT molecules also semi-deprotonate on Mg(0001), and self-assemble with the surface adatoms to form MONs. As seen in the active center of RuBisCO, the Mg adatoms act as metal centers surrounded by semi-deprotonated NH_2 groups. Thus, these networks demonstrate their potential to resemble the structural configuration of a lysine molecule around the Mg center. On Mg(0001), the MONs present a 2D structure, in contrast to the 1D structures formed on Cu(100). This could be related to the lower reactivity of the Mg(0001) substrate, which produces a weaker molecule-substrate interaction compared to Cu(100). Finally, after the injection of CO_2 into the Mg-TAPT network on Mg(0001), STM images detect a change in the structure that, according to HR-XPS measurements, would be related to the formation of carbamates.

These MONs have the potential to work as 2D biomimetic structures, analogues to the active site of RuBisCO towards CO_2 capture to form carbamates. In addition, the structure of the MONs of Mg-TAPT and Cu-TAPT presents pores that can act as trap sites for atoms or molecules. The importance of the formation of these supramolecular structures relies on the joint of several characteristics, such as self-assembly of molecules including adatoms in the adlayer, formation of pores acting as molecular/metal adatoms traps and the flexibility for structural reconfiguration. Also, the control of the dimensionality by temperature represents an interesting tool to control the design of supramolecular architectures adsorbed on metal surfaces.

Chapter 4: Reactivity of Metal-Organic Networks of TPA and Mg towards CO_2 and O_2

Photosynthesis is the model system for energy conversion and uses CO_2 as its starting reactant to transform solar energy into chemical energy, *i.e.* the energy is stored as chemical bonds in organic molecules or biomass [1]. The first and rate-determining step of this process is the immobilization and activation of CO_2; a carboxylation reaction catalyzed by the enzyme RuBisCO. The catalytic activity of RuBisCO is performed on a metal ion embedded on its active site. Thus, the nature and the oxidation state of the metal center defines the catalytic properties of the enzyme. The most common ion found in the active site is Mg^{2+}.

In this chapter, we explore the rational design of metal-organic networks (MONs), to mimic the active site of RuBisCO. As seen in the previous chapter, MONs were formed after the deposition of molecules with NH_2 groups, such as TAPT, on metallic surfaces. However, molecules with carboxylic functional groups (COOH) can also work as excellent building blocks in the design of molecular nanostructures. One characteristic is the deprotonation of COOH into a carboxylate group (COO^-) on metal surfaces at RT, which confers them the ability to form robust MONs with co-deposited transition [20], [29], [41], [99], [118], [119], and alkali metal atoms [23], [24], [27], [120]. Thus, terephthalic acid (1,4-benzenedicarboxylic acid, TPA) is a model molecule with COOH groups that easily deprotonates on Cu surfaces at RT and often forms MONs with co-deposited adatoms [24]. The COO^- groups act as ligands that control the redox potential and the distribution of metal centers [29], [30]. This particular feature encouraged the use of COO^- - Fe networks for O_2 dissociation [15], [58], aimed to resemble the catalytic function of enzymes specialized in O_2 reduction [61].

The catalytic function for CO_2 adsorption has recently being studied on MONs. One of the few examples involves the use of metal-organic chains of 1,4-phenylene diisocyanide molecules bonded to Au adatoms on Au(111), to promote CO_2 capture at 77 K [121], [122]. Just recently, networks formed by molecules with COO^- groups bonded to Fe centers have shown adsorption of CO_2 at 100 K [65]. Nevertheless, to the best of our knowledge, no CO_2 driven phase transition has been reported at RT for any 2D metal-organic array.

Therefore, inspired on the structure of the active site in RuBisCO, this chapter presents a method to replicate the carboxylate environment around a Mg^{2+} ion. In contrast to the method presented in Chapter 3, here the ionic networks with Mg^{2+} are designed by the self-assembly of TPA molecules with Mg atoms deposited on substrates of Cu(100) and Mg(0001) at RT. Finally, to study the reactivity of the structures, high partial pressures of CO_2 and O_2 are exposed on the

system at RT. The stability and chemical changes in the networks related to gas adsorption are studied by different techniques such as STM, HR-XPS and DFT.

4.1. Experimental setup

The experiments were carried out in a UHV (~ 3 x 10^{-10} mbar) chamber. The Cu(100) surface was cleaned following the standard procedures described in Chapter 2. TPA molecules were deposited by organic molecular beam epitaxy from a Knudsen cell at 448 K. During deposition, the substrate was kept at RT. During the dosage of CO_2 or O_2, the pressure in the chamber was kept at a partial value of P~1.0x10^{-7} mbar, while the temperature of the sample was kept at RT. The STM images were obtained with typical tunneling current and sample bias values of 1.0 nA and -1.0 V, respectively. The XPS spectra were obtained in the PSI synchrotron facilities. The data for the Mg2p, C1s and O1s were acquired with a beam energy of 160, 370 and 675 eV, respectively, and the pass energy of the analyser was set at 20 eV. The spectra were referenced using the $Cu3p_{3/2}$ line at 75.1 eV. All the experiments were also carried out under UHV at RT.

4.2. Mg Atoms Deposited on Cu(100) and their Reactivity towards CO_2 and O_2

The study of the behaviour of Mg atoms on a Cu(100) surface, was taken as the first step in the strategy towards the formation of ionic networks with Mg. Thus, a sub-monolayer (ML) coverage of Mg atoms was deposited by thermal evaporation on a Cu(100) surface at RT. The distribution of Mg on the surface was studied by STM at RT. During the scans, the diffusion of Mg adatoms prevented the observation of the surface due to their constant attachment to the STM tip. This issue was solved annealing the sample at 353 K for 5 minutes; a process that induced the formation of Mg clusters. The STM image in **Figure 4.1** shows bright protrusions with an average diameter of 1.5 nm, which represent the isolated clusters of Mg (0.03 ML) on the terrace. Their reactivity was studied by the introduction of either 450 L of CO_2 or O_2. Nevertheless, during the scans, the gas molecules of CO_2 or O_2 and the Mg adatoms react strongly with the tip. For this reason, it was impossible to detect any interaction of gas molecules with Mg atoms with this technique; only fuzzy images were obtained (not shown here).

In order to understand the system better, HR-XPS was used to assess the chemical changes after the injection of CO_2 and O_2 at RT (**Figure 4.2**). The first step was to study the chemical states of the Mg clusters before gas injection (green-colored spectra). Thus, a new sample was prepared using the same conditions as stated above. The Mg2p energy region shows two sharp peaks at lower binding energies: One peak at **50.0 eV** characteristic of metallic clusters of Mg (Mg^0) [123]–[125], and a second peak at **50.4 eV** related to smaller Mg clusters [125]–[130]. This increment in the binding energy is attributed to the local charge transfer of a low coverage of Mg clusters with the substrate, which results in the increment of its binding energy due to the lower screening of the core electrons from Mg atoms. The broad peak observed at higher

binding energies (**51.4 eV**) is related to ionic Mg^{2+} species, such as magnesium oxide (MgO) [126]–[128], [131]. The presence of this peak would be the consequence of spurious CO_2 or O_2 molecules inside the chamber reacting with the Mg clusters. Indeed, these species could be assigned as dimmed traces close to the noise level in the O1s region, with the peaks at **533.0** (Mg(OH), MgO_2 or $Mg(OH)_2$) [123], [126], [131] and **530.7 eV** (O_2^- chemisorbed) [126], [132].

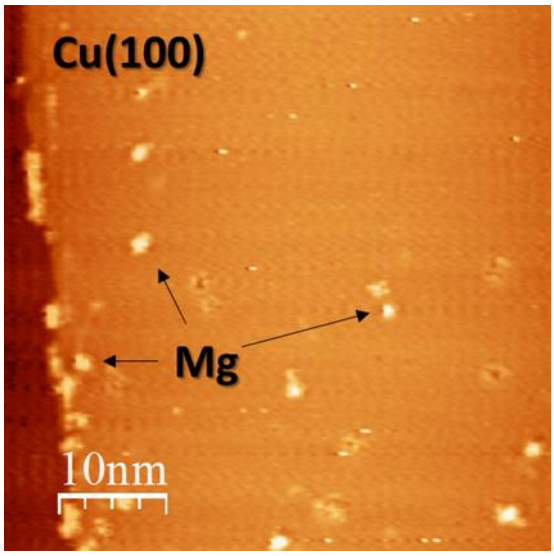

Figure 4.1: STM image of Mg clusters on a Cu(100) surface at RT under UHV.

The second step was to address the chemical changes after CO_2 injection. The red-colored spectra in **Figure 4.2** belong to the Mg clusters exposed to 540 L of CO_2. In the Mg2p energy region, the line shape broadens and shifts towards higher binding energies. The deconvolution of the Mg2p signal, reveals that the presence of metallic clusters vanishes (peak at 50.0 eV) while the peak attributed to Mg^{2+} species at **51.4 eV** increases significantly. This increment would be related to magnesium carbonates ($MgCO_3$) formed as a consequence of the CO_2^- chemisorption [123], [133]. According to Thomsen et.al, the chemisorption of CO_2^- on an alkaline-supported Cu substrate would result in: $2CO_2^- \rightarrow CO_3^{2-} + CO_a$ [134]. The by-product of the reaction, CO, is not observed in the O1s spectra because it is desorbed from the Cu surface that is held at a relative high temperature, RT [134]. In agreement to the previous analysis, the spectrum in the O1s region shows the increment of the peak at **532.7 eV** as a result of the contribution of the chemisorption of CO_2^- on Mg, to the pre-existent spurious signal (Mg(OH), MgO_2 or $Mg(OH)_2$), resulting in [122], [132], [135]–[137]. Finally, the peak at **530.1 eV** shows the presence of O_2^- species on Mg [126], [130].

A different sample was prepared was to address the chemical changes after O_2 injection. The blue-colored spectra in **Figure 4.2** belong to the Mg clusters exposed to 450 L of O_2. Interestingly, the Mg 2p spectra shows a peak at **49.7 eV**, which lies in the region of metallic Mg^0. Nevertheless, this interpretation is not self-consistent since the typical metallic signal is characterized by a sharp peak [123]–[125]. In addition, because of the well-known high reactivity of Mg with O_2, the formation of MgO species is expected in this system. Nevertheless, the Mg2p

feature related to MgO species, usually appears at higher binding energies [123]. Aballe et al. reported a shift from high to lower binding energies when Mg grows from a sub-ML to a 1 ML coverage on W(110) [129]. They explained this trend as the stronger atomic interactions present in 1 ML of Mg, which induces the screening of the core electrons due to the higher electronic density. Therefore, the peak observed at low binding energy (**49.7 eV**) would be attributed to the formation of big MgO clusters and the effect of the oxidized Cu substrate, as it will be shown in the O1s region [138]. Up to now, this statement was not confirmed by STM due to the high reactivity of O_2 with the tip, as explained above. In connection therewith, the line shape in the O1s region shows a broad peak at **531.6 eV** that confirms the presence of clusters of MgO [130], [137]. In addition, the strong signal at **529.7 eV**, is attributed to the oxidation of the bare Cu surface [71], [139], [140]. The low relative peak area of MgO compared with CuO, is related to the low quantity of Mg species (sub-ML coverage) on the Cu surface (bulk). These findings would indicate that MgO clusters lie on a CuO surface, which in fact would also contribute to shift the MgO peak in the Mg2p region to lower binding energies.

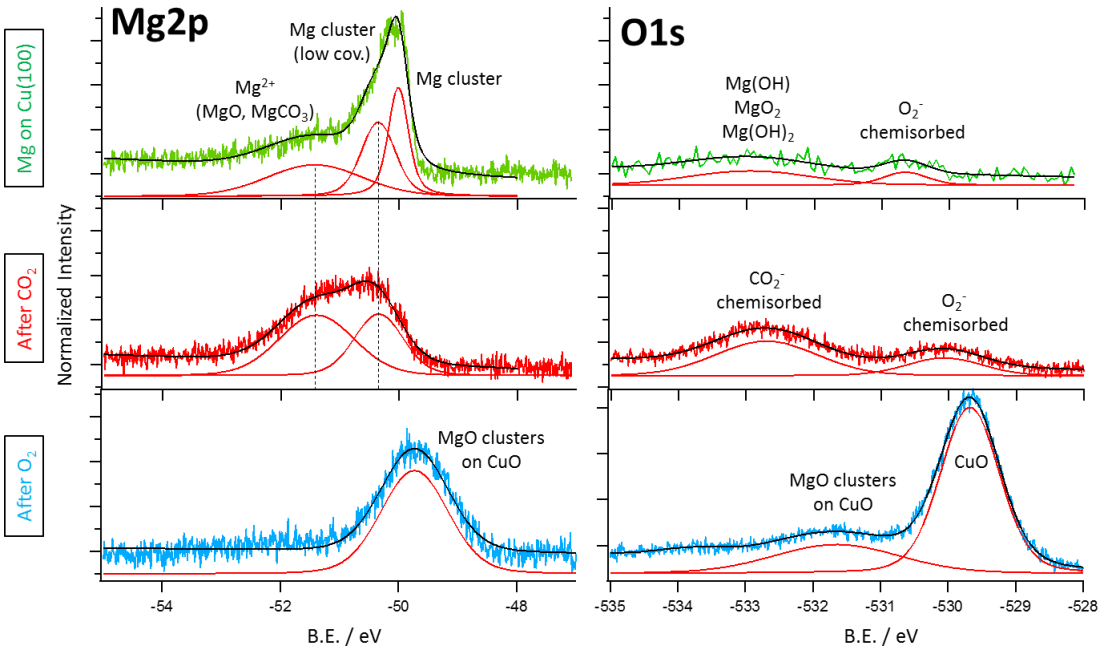

Figure 4.2: HR-XPS spectra in the Mg2p and O1s regions, showing the effect of the gas molecules on Mg atoms deposited on Cu(100). The green lineshape corresponds to Mg clusters on Cu(100). The red and blue lineshapes correspond to the effect of CO_2 and O_2, respectively.

DFT calculations were used to study the pathway of the reaction between single atoms of Mg with molecules of CO_2 or O_2 (**Figures 4.3**). Ane Sarasola performed the calculations under the supervision of Prof. Andres Arnau from the Donostia International Physics Center in Spain. The experiments were modelled as systems based on one and two Mg adatoms (represented by green circles), both lying on a slab of Cu atoms (represented by orange circles). A molecule of CO_2 or O_2 was introduced in the calculations to test the reactivity of the systems. **Figure 4.3(a)**

depicts the top and side views of the modelled systems exposed to CO_2. It shows that CO_2 is physisorbed in the presence of one Mg atom, while it chemisorbs with the characteristic sp2 conformation in the presence of two Mg atoms [48]. The CO_2 adsorption generates an energy gain of -0.36 and -1.30 eV for the systems with one and two Mg atoms, respectively. In both cases, the Mg centers lose the two valence electrons from the upper shell 2s, and turn into Mg^{2+} cations. Then, the charge is distributed between the oxygen atoms from CO_2 and the Cu atoms from the substrate. On the other hand, **Figure 4.3(b)** depicts the top and side views of the modelled systems exposed to O_2. In this case, the interactions turn stronger; O_2 is chemisorbed in the presence of one Mg atom, while it is dissociated in the presence of two Mg atoms. The adsorption of O_2 produces energy gains of -2.54 eV and -5.09 eV, respectively. These energy values are high enough to form strong bonds between O_2 and Mg, hence to promote the formation of MgO, as observed by XPS experiments.

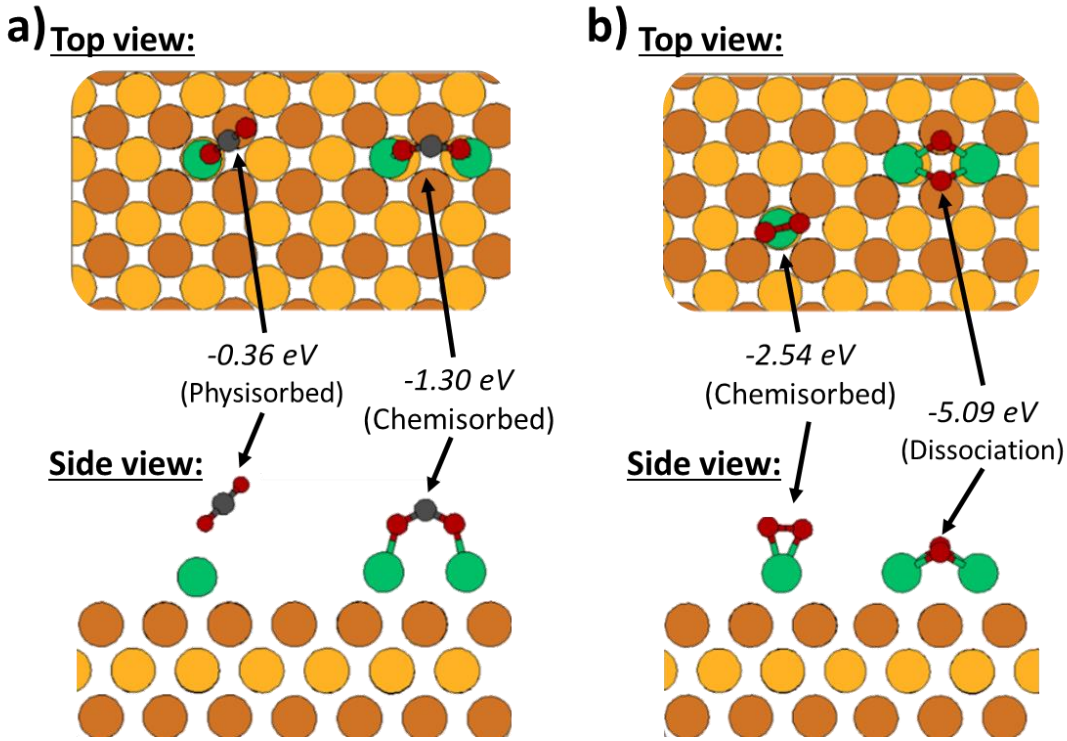

Figure 4.3: Top and side views of model systems that evaluate the adsorption of CO_2 and O_2 on Mg atoms (represented by the green circles) lying on a Cu(100) surface (represented by the orange circles). (a) CO_2 physisorbs and chemisorbs in the presence of one and two Mg atoms, respectively. (b) O_2 chemisorbs and dissociates in the presence of one and two Mg atoms, respectively.

These findings confirm the results analyzed by XPS in **Figure 4.2**, regarding to the chemisorption of CO_2 and O_2 on systems with more than one Mg atom (Mg clusters). Understanding the chemistry behind the interaction of gas molecules with Mg clusters or single Mg atoms is crucial for the study of more complex systems including organic molecules.

4.3. TPA Molecules Deposited on Cu(100) and their Reactivity with CO_2 and O_2

The second step in the strategy towards the formation of ionic networks with Mg, is to study the self-assembly process of the organic linkers. At first, TPA molecules (coverage = 0.4 ML) were deposited on an atomically clean Cu(100) surface at RT. As reported in earlier studies and represented in the scheme of **Figure 4.4(a),** the TPA molecules fully deprotonate on a Cu surface at RT [141], [142]. Indeed, the typical STM image of this system **Figure 4.4(b)**, shows the self-assembly of fully-deprotonated TPA molecules into a homo-molecular patch of TPA molecules with a 3x3 structure [141], [142]. The chemical identity of the molecules was confirmed by the HR-XPS spectra in **Figure 4.4(c)**. The XPS spectrum in the C1s region, shows the typical profile of a homo-molecular network of fully-deprotonated TPA molecules: an intense peak at **284.6 eV** attributed to carbon atoms from the phenyl ring (C6) and a small peak at **287.6** eV, characteristic of carboxylate groups ($-COO^-$) [141]. The dotted peak at **285.1 eV** was not fully identified but could be related to the different chemical environment around the aromatic carbons. The 3x3 structure is also confirmed by the analysis of the XPS spectrum in the O1s region, which contains a single peak at **531.3 eV** attributed to carboxylate oxygens ($-COO^-$).

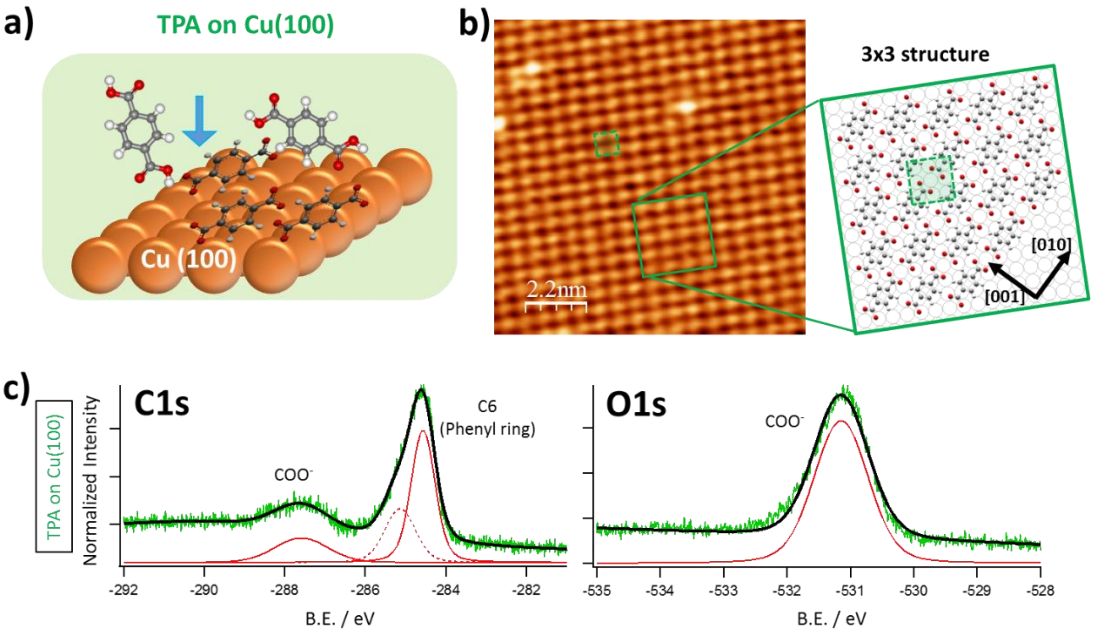

Figure 4.4: (a) Scheme that represents the deposition and the consequent deprotonation of TPA molecules deposited on Cu(100) at RT. (b) STM images of a typical TPA network on Cu(100) at RT. The inset shows the structural model of the full-deprotonated molecules arranged in a typical 3x3 configuration. c) The HR-XPS spectra in the C1s and O1s energy regions show the characteristic peaks regard to the homo-molecular 3x3 phase.

In separate experiments, the 3x3 structure was exposed to 470 L of CO_2 or 450 L of O_2, to study its gas reactivity. In both cases, the STM images did not show any structural change (Figures are

not shown here). The HR-XPS technique was also used, to study any possible chemical changes that could not be detected with STM. **Figure 4.5**, shows the HR-XPS spectra of TPA on Cu(100) samples exposed to CO_2 (red spectra) and O_2 (blue spectra). In both cases, the C6 ring and COO^- signals in the C1s region did not present any variation compared to the sample before gas exposure (grey spectra). These experiments confirm that the TPA molecular phase is not reactive under the presence of CO_2 nor O_2 exposure. Conversely, in the O1s region, the exposure to O_2 molecules generates a peak at **529.7 eV** characteristic of O^{-2} chemisorbed on bare surfaces [137], whereas the peak at **531.3 eV** remain unchanged, confirming that the COO^- groups do not react with O_2 nor CO_2.

These results are important in the pathway toward the formation of MONs. The deposition of TPA on Cu(100) at RT using the conditions stated in this section, guaranties the full deprotonation of the molecules. The full deprotonation is important because COO^- oxygens are needed to bind and to control the redox potential of the metallic centers. In addition, the unreactive character of the COO^- groups with CO_2 and O_2 is crucial to discard the possible role of these groups as active centers.

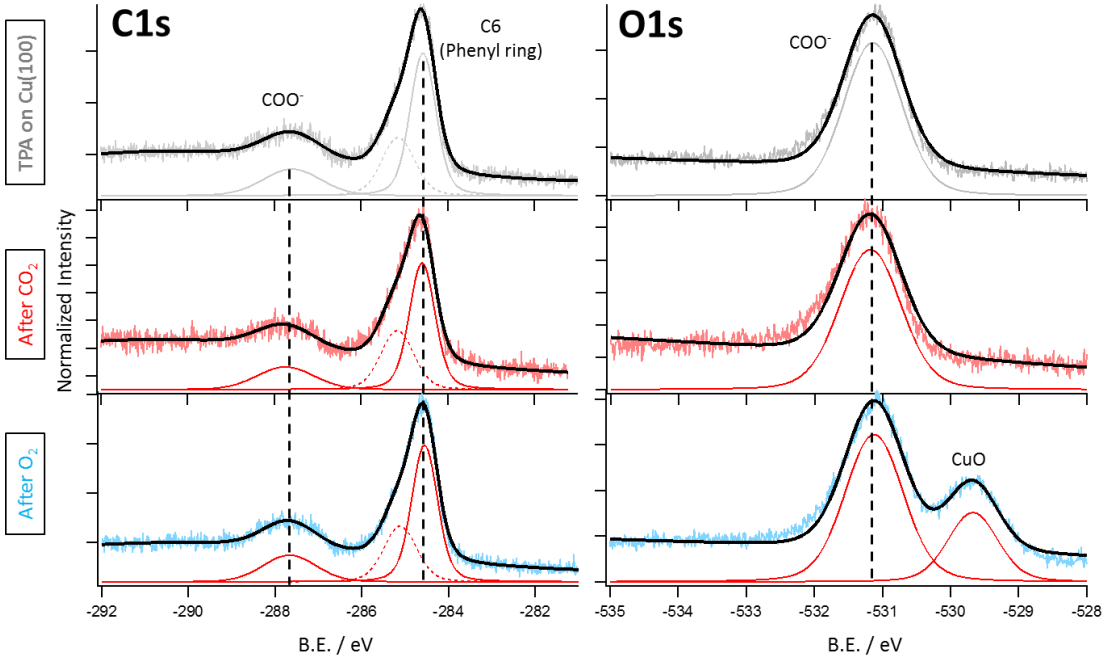

Figure 4.5: (a) HR-XPS spectra in the C1s and O1s energy regions showing that the homo-molecular 3x3 phase (grey spectra) does not react in the presence of CO_2 (red spectra) nor O_2 (blue spectra) molecules. In O1s, the peak characteristic of CuO appears as a consequence of the oxidation of the Cu(100) surface with O_2.

4.4. Formation of Mg-TPA Networks on Cu(100)

Inspired in the structure of the active site of RuBisCO, the fabrication of 2D ionic networks with a Mg^{2+} center is taken as a strategy to mimic its catalytic function. Studies in surface science have shown that the catalytic activity of metal particles is boosted when they are reduced to single atoms [143]. In this context, MONs can control the chemical environment around single atoms and their distribution along a metal surface [29], [30]. This characteristic makes them candidates to study hetero-catalysis.

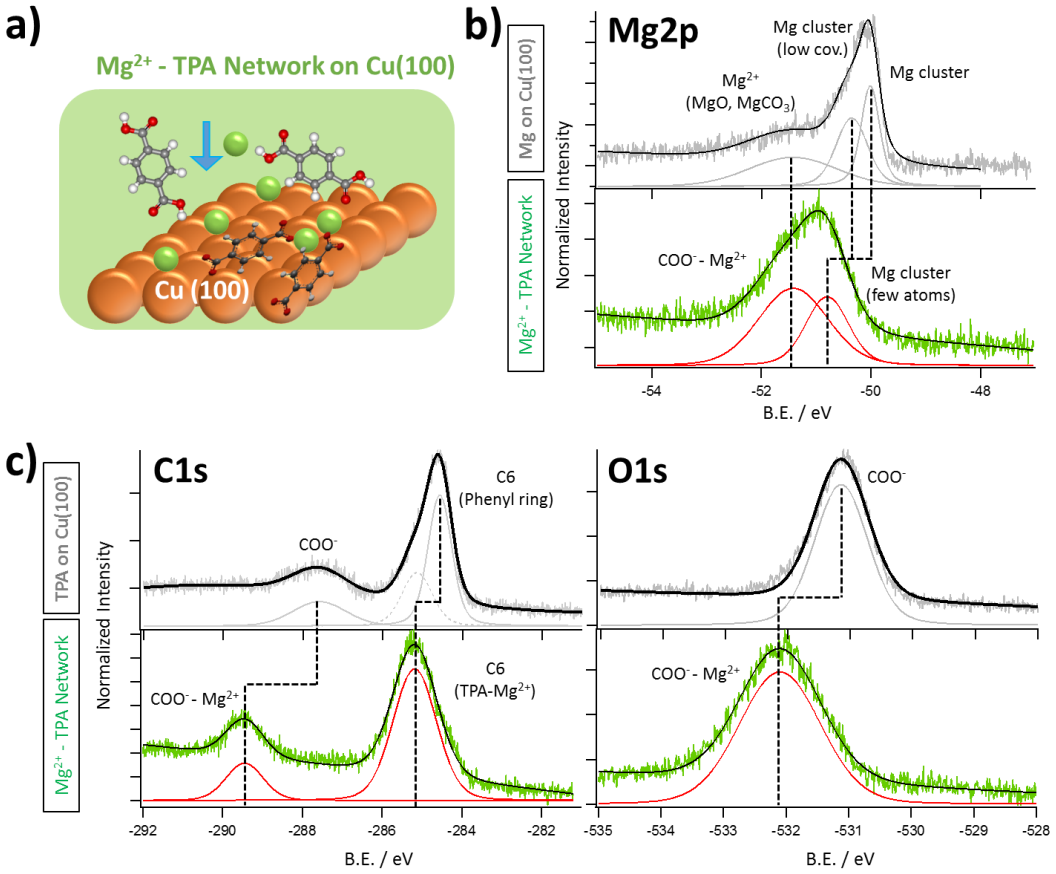

Figure 4.6: HR-XPS spectra for a typical ionic network. (a) Schematic representation of the ionic network prepared by the co-deposition of TPA molecules and Mg atoms. The interaction of (b) Mg clusters (grey spectrum in the Mg2p region) with (c) TPA molecules (grey spectra in the C1s and O1s regions), forms an ionic network (green spectra at the bottom of the images in (b) and (c)). The shift of the green spectra at the bottom respect with the grey spectra on top evidences the electrostatic interaction between Mg^{2+} and TPA.

Hence, the third and final step of the strategy is the study of the 2D self-assembly process of TPA molecules with Mg atoms. The preparation process begins co-depositing sub-ML coverages of Mg atoms and TPA molecules on an atomically clean Cu(100) surface at RT **(Figure 4.6(a))**. The deposition of each adsorbate followed the same preparation procedures presented in **sections 4.2 and 4.3**. The process was finalized with a post-annealing at 353 K for 5 minutes to

ensure the deprotonation of the TPA molecules and to favor the diffusion of the adsorbates on the surface.

The chemical interactions of the system is analyzed by HR-XPS. In the Mg2p binding energy region (**Figure 4.6(b)**), the green spectrum shows a broad peak shifted to higher binding energies with respect to the grey spectrum on top (note that the grey spectrum belongs to Mg clusters on Cu(100) before gas exposure, as presented in **Figure 4.2**). The peak splits in two components: One peak at **50.8 eV** that reveals the complete segregation of big clusters into clusters with smaller sizes; and a second peak at **51.4 eV,** in the region that belongs to the ionic form of Mg (Mg^{2+}). These two peaks suggest that the role of TPA molecules is to sequestrate Mg atoms from the clusters to form eventually ionic networks with Mg^{2+} cations. This fact, explains the absence of the peak assigned to big Mg clusters at lower binding energies. This mechanism may occur in a similar way as seen in ionic networks formed with alkali compounds [144]. In the C1s and O1s energy regions, the main peaks from the sample formed by the co-deposition of TPA molecules and Mg adatoms on Cu(100) (green spectra in **Figure 4.6 (c))**, also shift to higher binding energies compared to the peaks from a homo-molecular TPA layer (grey spectra). These shifts, are consistent with TPA molecules acquiring a protonated character on Cu(100) [141]. However, TPA molecules must be fully-deprotonated as they were deposited using the conditions stated in section 4.3. Therefore, the protonated character of the negatively charged COO^- groups would be given by the Mg^{2+} cations, thus evidencing the formation of ionic networks. The detailed analysis in the C1s region reveals a small peak at higher binding energies at **289.4 eV**, attributed to the electrostatic interaction between the COO^- group and the Mg^{2+} cations. Finally, the intense singlet at **285.2 eV**, is attributed to the C6 ring of the fully-deprotonated TPA interacting with Mg^{2+}. The high binding energies are associated to the charge migration from the C atoms towards the oxygens in COO^- [23]. In addition, the O1s lineshape shows a dominant peak at **532.1 eV**, related to a relative less negatively charged COO^- group due to the low electronic density around the core electrons during the electrostatic COO^- - Mg^{2+} interaction [23].

The STM image (**Figure 4.7(a)**), reveals a structure different from the typical squared-like 3x3-phase characteristic of molecular networks of TPA. The image shows white protrusions and the characteristic circular units that evidence the presence of TPA molecules. The inset in **Figure 4.7(a)** shows the zoom-in of the surface and reveals the convergence of TPA molecules around the white protrusions. In addition, smaller circular features are observed in between, related to Mg atoms that confirm the interaction between Mg and TPA. The nature of the white protrusions could be related either to the agglomeration of few Mg atoms or a single TPA molecule. Nevertheless, the agglomeration of few Mg atoms would be in agreement with the XPS characterization in the Mg2p region in **Figure 4.6(b)**. Indeed, the zoomed-in image in **Figure 4.7(b)** shows that the molecules are grouped in consecutive trigonal-planar arrangements evidencing their electrostatic coordination with Mg^{2+}. The model superposed in the inset (confirmed by the DFT calculations), presents a structure based on a Mg^{2+} ion, represented as a green solid circle, coordinated by three TPA molecules through at least one of their carboxylate moieties. Thus, two types of Mg-carboxylate coordination are present: one TPA forming a bidentate carboxylate coupling to Mg, and two TPA forming a monodentate coordination with Mg. From here on, this structure will be referred as Mg-3TPA.

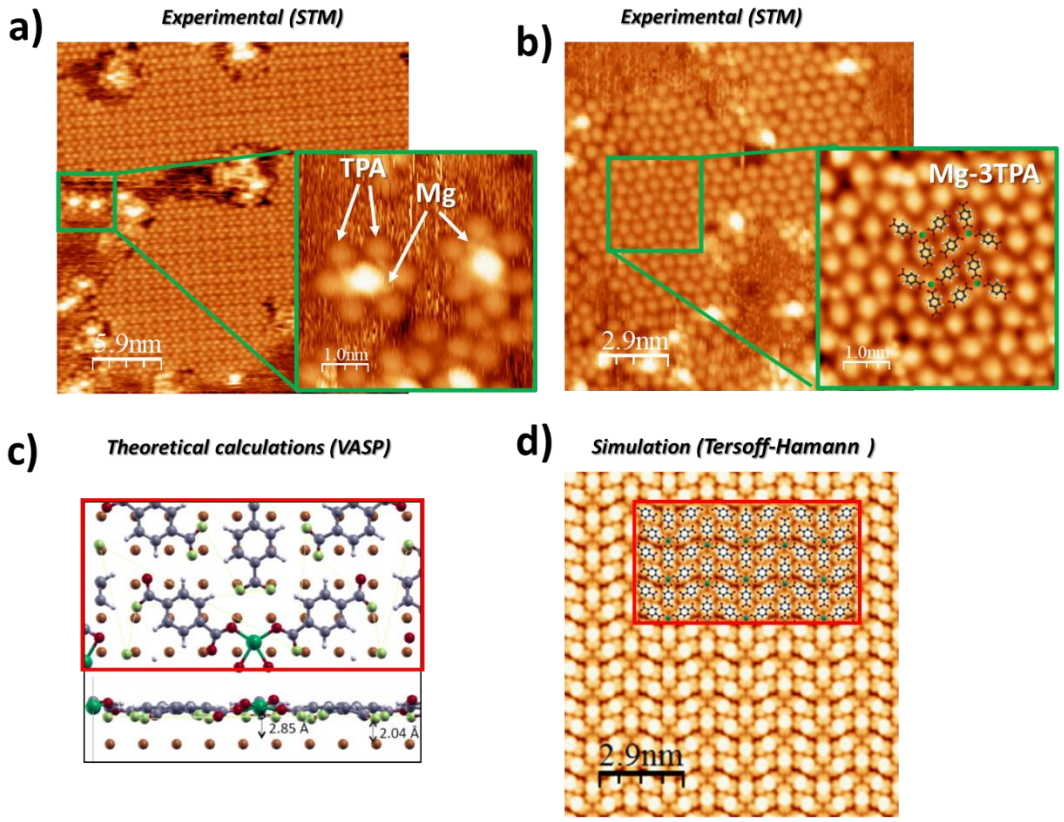

Figure 4.7: (a) Overview STM image that depicts a structure formed by the co-deposition of TPA molecules and Mg atoms. The zoom-in in the inset shows white protrusions surrounded by Mg atoms and TPA molecules. (b) A STM image whose inset shows the configuration between the TPA and Mg^{+2} into a Mg-3TPA structure. The TPA molecules are characterized by the circular motifs while the Mg^{+2} centers (represented by green circles in the superposed model), are visible as smaller circular protrusions. (c) The DTF calculations (VASP package) show a relaxed ionic network on top of a Cu(100) layer and confirms the preferential geometry of the structure: a Mg^{+2} ion coordinating three TPA molecules. The unit cell consists of one Mg^{+2} cation coordinating four carboxylate oxygens from three different TPA molecules. (d) The simulated STM image of the system using Tersoff-Haman Approach with a bias voltage of -2 *V* resembles very well the experimental STM images from (a) and (b).

The precise configuration of the Mg-3TPA structure is described also by DFT calculations. The calculations were performed using the Vienna Ab-initio Simulation Package (VASP) [74], [75], including vdW interaction within the vdW-dF scheme. A Cu(100) slab of one layer was included in the simulations, while the forces of the atoms from the organic overlayer were relaxed up to 0.05 eV/Å. As a result, a relaxed Mg-3TPA ionic network was simulated on top of a Cu(100) layer. A Bader charge analysis [145], [146], revealed a charge transfer of 5.25 e^- from the Cu layer to the organic overlayer and to the Mg^{2+} centers. As seen in **Figure 4.7(c)**, the unit cell consists of a Mg^{+2} cation coordinated by four atoms of O from three different TPA molecules. In agreement with crystallographic database for the average bond distance in Mg-carboxylate networks [54],

the distances O-Mg^{2+} for the monodentate and bidentate coordination present values of 2.03 and 2.20 Å, respectively. In addition, each TPA molecule forms H-bonds (O···H-C) between two of their uncoordinated carboxylate moieties and the aromatic rings from adjacent molecules. To confirm the reliability of the model, the Tersoff-Hamann approach [147], [148] simulated STM images of a typical Mg-3TPA network. The simulation was based on the integration of spatially resolved density of states (DOS) in energy, from a certain applied bias potential (-2.0 eV) to the Fermi level. The results plotted in **Figure 4.7(d)** reproduced the zigzagging inversely ordered trigonal-planar arrangements seen in the experimental STM images. An overlayer of the modeled Mg-3TPA structure was superimposed on the image to show in detail the geometry of the ionic network. Thus, DFT gave a model that agrees well with the structural features and chemical interactions observed previously by STM and XPS, respectively.

This section showed that upon deposition of TPA molecules and Mg adatoms on Cu(100), a 2D structure (Mg-3TPA) is formed. The structure stabilizes through ionic interactions between the COO^- groups from TPA (anion) and the Mg^{2+} centers (cation), thus resembling the carboxylate environment of the Mg^{2+} ion present in the active site of RuBisCO. The next section studies the reactivity of these ionic networks for gas adsorption.

4.4.1. Reactivity of Mg-3TPA Ionic Networks with CO_2

A typical ionic network with a Mg-3TPA configuration was prepared using the standard preparation procedure stated above. **Figure 4.8** shows a series of consecutive STM images taken on a defined area on the surface over different periods. The first two images, tracked the Mg-3TPA structure during a period of 67 minutes and it did not show any structural change. Thus, the Mg-3TPA network was suitable to test its reactivity in the presence of CO_2. The interaction with CO_2 was tracked during almost 2 hours. The first image with the black-colored borders (snapshot with t=0 min), corresponds to the moment when CO_2 is first released on the system. After only 22 L of CO_2 (10 minutes), the surface area of the network decreases, providing the first evidence of reactivity. Nevertheless, structural changes appear after 99 L of CO_2 (22 minutes), related to a significant decrease of the Mg-3TPA network domain at expenses of a new phase forming at the bottom right side of the snapshot. The new phase presents a different configuration and it turns predominant after 256 L of CO_2 (57 minutes). This structure presents a square-shaped unit cell (highlighted in yellow), and organizes the molecules in a particular fashion (one Mg adatom surrounded by four TPA molecules) that lead to the formation of pores (**Figure 4.8 (b)**). From here on, this structure will be referred as Mg-4TPA. The new arrangement suggests only one type of Mg-carboxylate coordination: monodentate couplings (O-Mg) of the Mg center with each TPA molecule [29]. In addition, each TPA molecule forms H-bonds (O···H-C) between two of their uncoordinated carboxylate moieties and the aromatic rings from adjacent molecules. The pores in the network result from the convergence of four uncoordinated carboxylate oxygens from four TPA molecules. After 473 L of CO_2 (105 minutes), the coverage of the predominant Mg-4TPA phase increases while the former Mg-3TPA structure vanished completely. Finally, the CO_2 injection was stopped and the images were tracked during the next 17 minutes to observe if the structure could reverse from the Mg-4TPA to a Mg-3TPA

configuration. The last snapshot at 122 minutes shows the stability of the Mg-4TPA structure with no signs of structural reversibility. Thus, this experiment shows that CO_2 catalyzed a new phase transition: from a Mg-3TPA to a Mg-4TPA configuration.

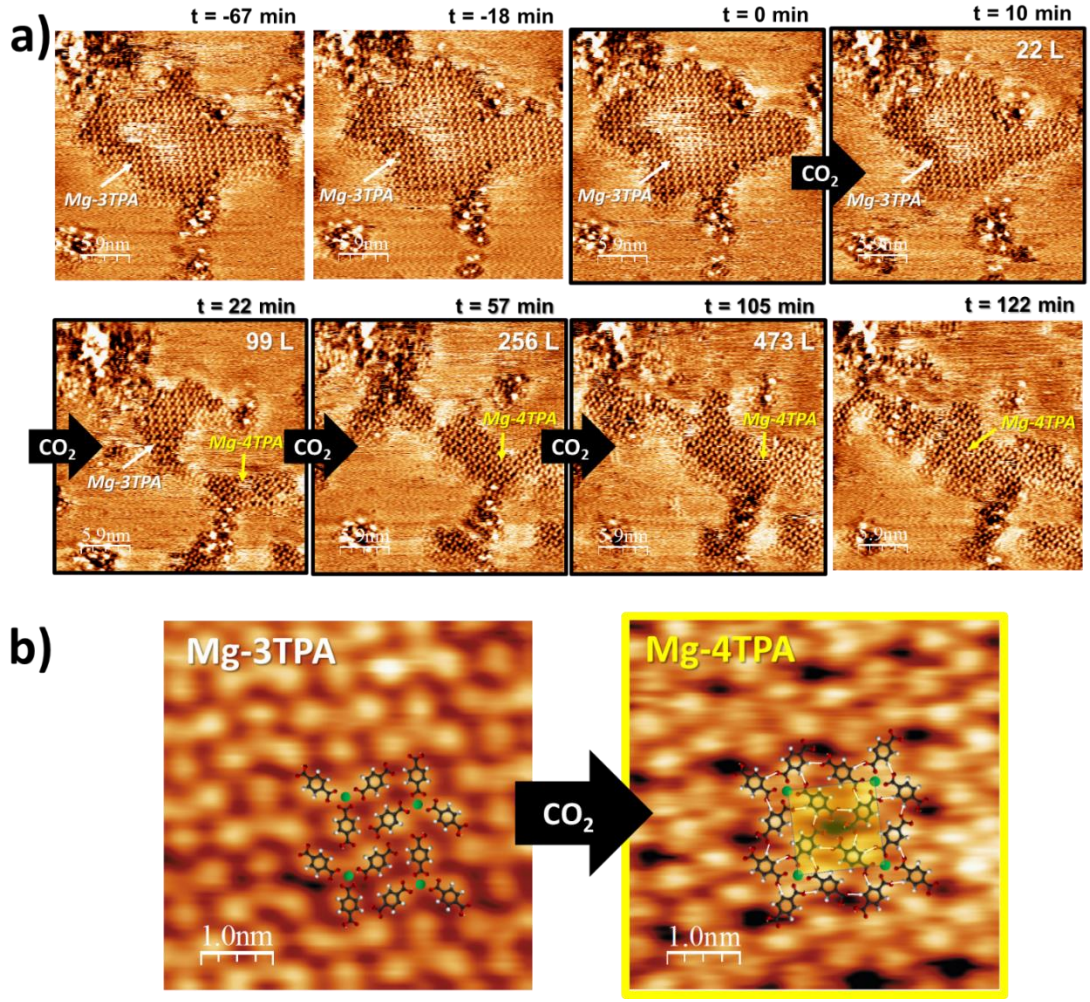

Figure 4.8: (a) Snapshots from a time lapsed sequence of STM images, for a Mg-3TPA ionic network on Cu(100), taken before, during (images with a black-colored border) and after being exposed to CO_2. A transition from a Mg-3TPA to a Mg-4TPA structure, is observed. (b) The unit cell of the new Mg-4TPA structure is based on a Mg^{+2} cation coordinating four carboxylate oxygens from four different TPA molecules. Each TPA molecule links to three adjacent molecules by H-bonds between two of their uncoordinated carboxylate oxygens and their aromatic rings. The pores in the structure are formed by the convergence of four uncoordinated carboxylate oxygens from four TPA molecules.

The structural changes observed by STM encouraged the use of DFT calculations to study in detail the local charge distribution when CO_2 interacts with the ionic networks. The results showed that the presence of CO_2 distorts the local bonding in the Mg-3TPA structure, induced by a charge redistribution. The DFT calculation in **Figure 4.9** shows that CO_2 binds to Mg^{2+} in a linear configuration. This configuration is related to a physisorption of CO_2, with a charge

transfer weaker than a bended sp2 configuration related to a chemisorption [65]. Nevertheless, the adsorption of CO_2 on Mg^{2+} in the Mg-3TPA network was calculated as -0.69 eV, which is almost twice the value of the physisorption of CO_2 on a single atom Mg on Cu (-0.36 eV, as seen in **section 4.2**). Considering the previous results by STM, this interaction is high enough to induce a weakening in the strength of the bonds between Mg^{2+} and the carboxylate oxygens from TPA to form the Mg-4TPA structure.

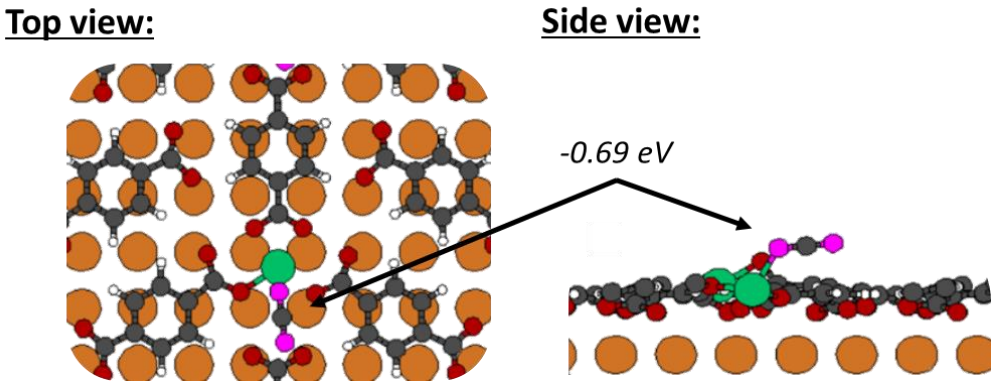

Figure 4.9: Top and side views that evaluate the local detail of the CO_2 adsorption on the Mg-3TPA ionic network. DFT reveals that CO_2 adsorbs on top of the Mg^{2+} center.

The chemistry of CO_2 adsorption in the ionic networks was also studied using HR-XPS (**Figure 4.10**). As represented in the scheme of **Figure 4.10(a)**, the typical Mg-3TPA ionic network was exposed to 945 L of CO_2 and measured immediately by HR-XPS. The red-colored spectra in **Figures 4.10(b)-(d)** do not show large changes in the Mg2p, C1s and O1s energy regions, compared to the grey-colored spectra shown on top (the grey spectra correspond to the Mg-3TPA network presented in **Figure 4.6**). As studied by STM and DFT, CO_2 physisorbs on the Mg^{2+} center to generate a phase transition from a Mg-3TPA into a Mg-4TPA structure. Therefore, the slight difference of the COO^- - Mg^{2+} coordination between both structures may produce changes in the chemical environment around the Mg and O atoms. In connection to this, the detailed analysis of the Mg2p region (**Figure 4.10(b)**), revealed the increment in the relative peak area at **51.4 eV** (COO^- - Mg^{2+}) at expenses of the peak at **50.8 eV** (Mg cluster formed by few atoms). This evidence probes the action of CO_2 to enhance the segregation of the remaining small Mg clusters into Mg atoms that eventually coordinate with deprotonated TPA molecules to form bigger patches of ionic networks. Indeed, the segregation of the Mg clusters can be related to the joint action of CO_2 and deprotonated TPA molecules. As seen in **section 4.2**, the sole interaction of CO_2 with Mg clusters forms $MgCO_3$ as a by-product. On the other hand, **section 4.4** showed that fully- deprotonated TPA species could segregate the clusters into single atoms of Mg, whose distribution on the surface is controlled by the COO^--Mg^{2+} coordination. Thus, it can be concluded that the single Mg^{2+} ions present in the ionic network promote only the physisorption of CO_2, thus preventing the formation of $MgCO_3$. Nevertheless, the reason that explains why CO_2 enhances the formation of the Mg-4TPA structure and the sequestration of Mg adatoms is not well understood yet.

In connection, the fate of CO_2 is unknown. In **Figure 4.10(c)**, the red-colored lineshape in the energy region of C1s was analyzed to find out the presence of CO_2. However, it does not show any variation respect to the grey spectra. The peaks related to the carbon from the COO^- groups and the C6 rings from the TPA molecules that form a COO^- - Mg^{2+} coordination, remain at **289.4** and **285.2 eV**, respectively. Hence, the presence of adsorbed (physisorbed or chemisorbed) species of CO_2 is imperceptible. The presence of absorbed CO_2 is also elusive in the O1s region (**Figure 4.10(d)**). The difficulty to observe the peaks related to CO_2, lead to consider also the possibility that CO_2 may have left the system. Nevertheless, the red spectrum shows the peak at **532.2 eV** (Mg^{2+}-COO^-) slightly shifted by about **0.1 eV** to higher binding energies compared with the spectrum in grey. This shift could be related to the different coordination environment of the COO^- oxygens present in the recently formed Mg-4TPA configuration.

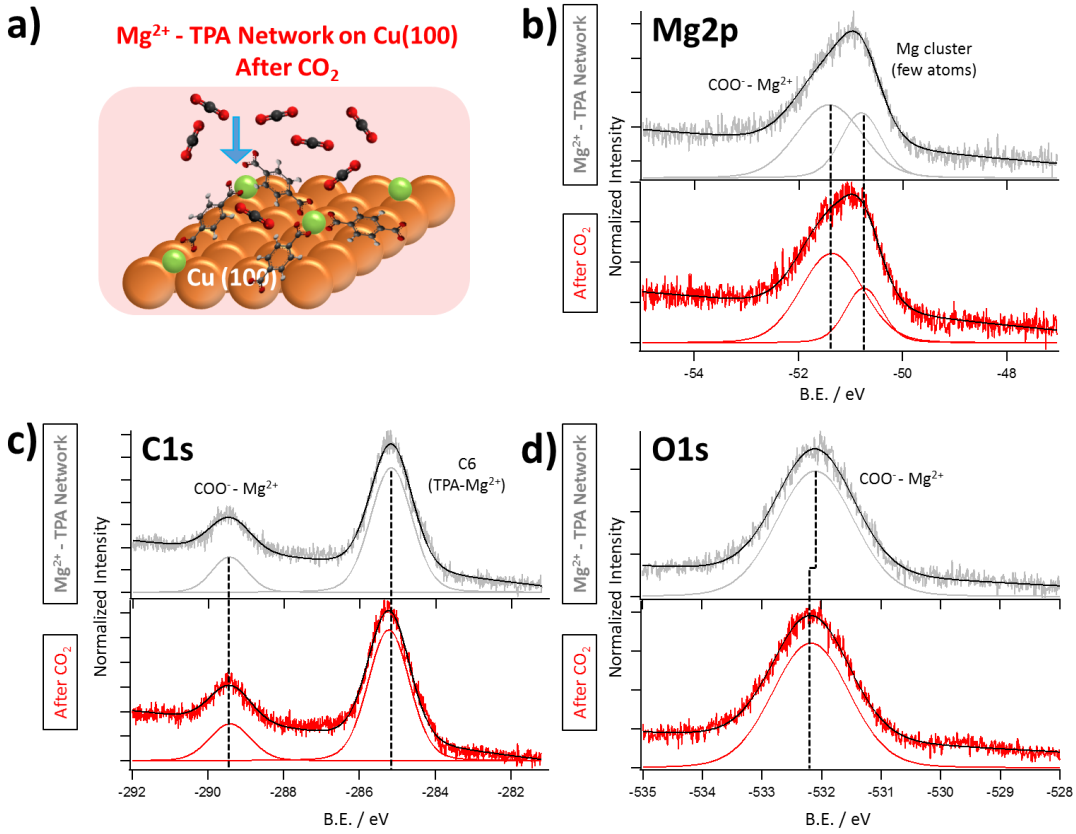

Figure 4.10: (a) Schematic representation of the typical Mg-3TPA network exposed to CO_2 molecules. (b) HR-XPS spectra of the sample before (grey lineshape) and after (red lineshape) being exposed to 945 L of CO_2 in the (b) Mg2p, (c) C1s and (d) O1s energy regions.

Summing up, even though XPS is not very conclusive regarding to the CO_2 adsorption, these spectra aimed to be explorative and a more detailed analysis on very specific binding energy regions may be required. However, STM and DFT showed that the interaction of CO_2 is strong enough to reorganize the charge around Mg^{2+} hence triggering a transition from a Mg-3TPA to a Mg-4TPA coordination. Thus, the ensemble of the results obtained by STM, DFT and XPS

conclude that CO_2 interacts with the system through a temporary physisorption on Mg^{2+}. It is worth to consider that the feeble CO_2 interaction with the Mg^{2+} centers in the ionic networks could lead to unperceivable changes in the XPS spectra, thus hindering the presence of physisorbed CO_2.

4.4.2. Reactivity of Mg-3TPA Ionic Networks with O_2

A new experiment was conducted to study the interaction of the ionic networks with O_2 molecules. The new sample was prepared following the standard procedure stated in **section 4.4.** Consecutive STM images were taken on a defined area on the surface over different periods of time **(Figure 4.11)**.

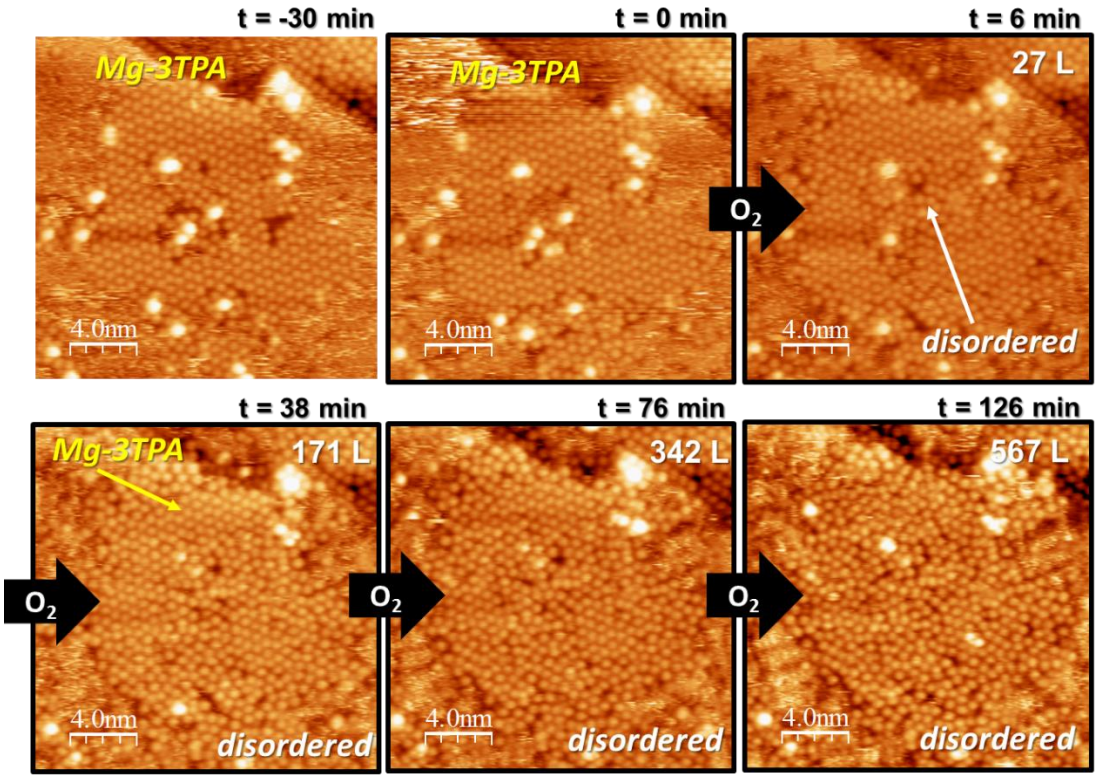

Figure 4.11: Snapshots from a time lapsed sequence of STM images for a TPA-Mg ionic network on Cu(100) taken before, during (images with a black-colored border) and after exposure to O_2. The Mg-3TPA transitions to a disordered molecular phase.

The first snapshot revealed the presence of the Mg-3TPA ionic network. As seen in the second snapshot, the ionic network did not show any structural changes during an interval of 30 minutes. Thus, this ionic network was found suitable to study its reactivity with O_2. The snapshots highlighted on black correspond to consecutive STM images taken during the exposition of O_2 for a period up to 2 hours. The first image with the black-colored borders (snapshot with t=0 min), corresponds to the moment when O_2 is released on the system. The first structural change is observed after the exposure of 27 L of O_2 (6 minutes). The ionic network

begins to disassemble from its center and this tendency continues while more O_2 is introduced. Hence, after 171 L of O_2 (38 minutes), most of the Mg-3TPA structure disassembles. The disassembly is more evident after 342 L of O_2 (76 minutes) while the borders of the terraces present also strong signals of oxidation. Finally, a fully disordered structure is observed after 567 L of O_2 (126 minutes). Contrary to the case with CO_2, the structure never shows reorganization into an ordered configuration. These observations evidence the direct interaction of O_2 with the system that provokes the complete and irreversible detachment of the components involved in the Mg^{2+}-COO^- coordination.

In contrast to the phase transition from Mg-3TPA to Mg-4TPA promoted by CO_2, the phase transition of Mg-3TPA to a disordered structure is rather specific to O_2. Thus, DFT calculations were used to study in detail the local charge distribution when O_2 interacts with the Mg-3TPA network. The results showed that O_2 also binds through one of its oxygen atoms to the Mg^{2+} center of the ionic networks. As shown in **Figure 4.12** the absorption energy of O_2 on Mg^{2+} was calculated as -0.79 eV. This value is almost one third of the value related to the chemisorption of O_2 on a single Mg atom (-2.54 eV, as seen in **Figure 4.3**). Nevertheless, this low absorption energy is enough to generate the reconfiguration of the charge around Mg^{2+} and destabilization of the COO^- - Mg^{2+} interactions to finally lead to the dissociation of the Mg-3TPA structure.

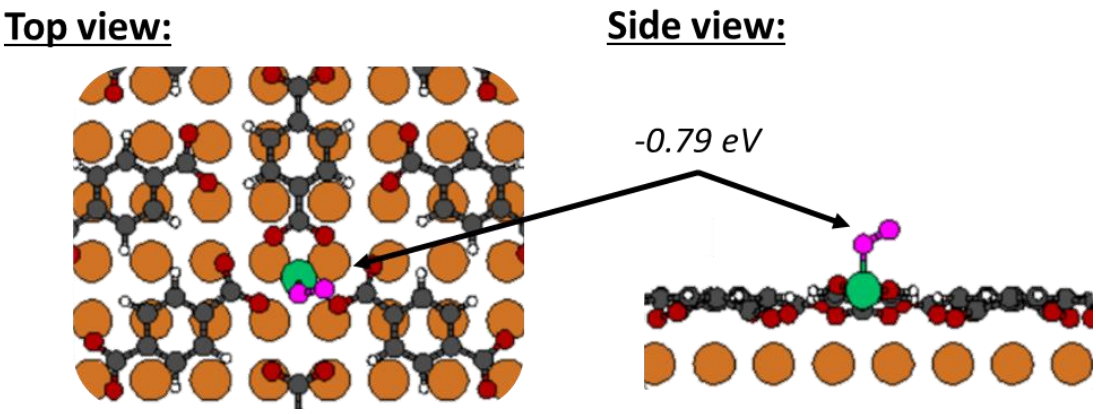

Figure 4.12: Top and side views of model Mg-3TPA system used to evaluate the local detail the O_2 adsorption on the Mg-3TPA ionic network. DFT showed that O_2 adsorbs on top of the Mg^{2+} center.

HR-XPS studied the chemistry of O_2 adsorption in the ionic networks (**Figure 4.13**). As represented in the scheme of **Figure 4.13(a)**, a typical Mg-3TPA ionic network was exposed to 500 L of O_2. **Figures 4.13(b-d)**, show the Mg2p, C1s and O1s energy regions of a Mg-3TPA network after O_2 exposure (blue-colored spectra). The peaks in all the energy regions shifted to lower binding energies compared to the Mg-3TPA network before O_2 exposure (grey-colored spectra).

The O1s binding energy region shows an intense peak at lower binding energy (**529.7 eV**) related to CuO, as a consequence of the reactivity of O_2 with the Cu(100) surface. However, the broader peak arising at a higher binding energy, whose deconvolution reveals two peaks at 531.1 and

531.6 eV, evidences the reactivity of O_2 with the ionic network. As studied by STM and DFT above, O_2 quenches the charge in the Mg^{2+} center and consequently disassembles the COO^- - Mg^{2+} interactions. In fact, the peak at **531.1 eV** is characteristic of the COO^- group of TPA molecules (see **Figure 4.5**) [141] and thus confirms the disassembly of the TPA molecules from the ionic network. Accordingly, the peak at higher binding energy resembles the peak characteristic of MgO on CuO. Therefore, **531.6 eV** is attributed to the oxygen atoms involved in the COO^- - MgO interaction between the TPA molecules surrounding MgO centers (formed by the chemisorption of O_2^- on Mg^{2+}).

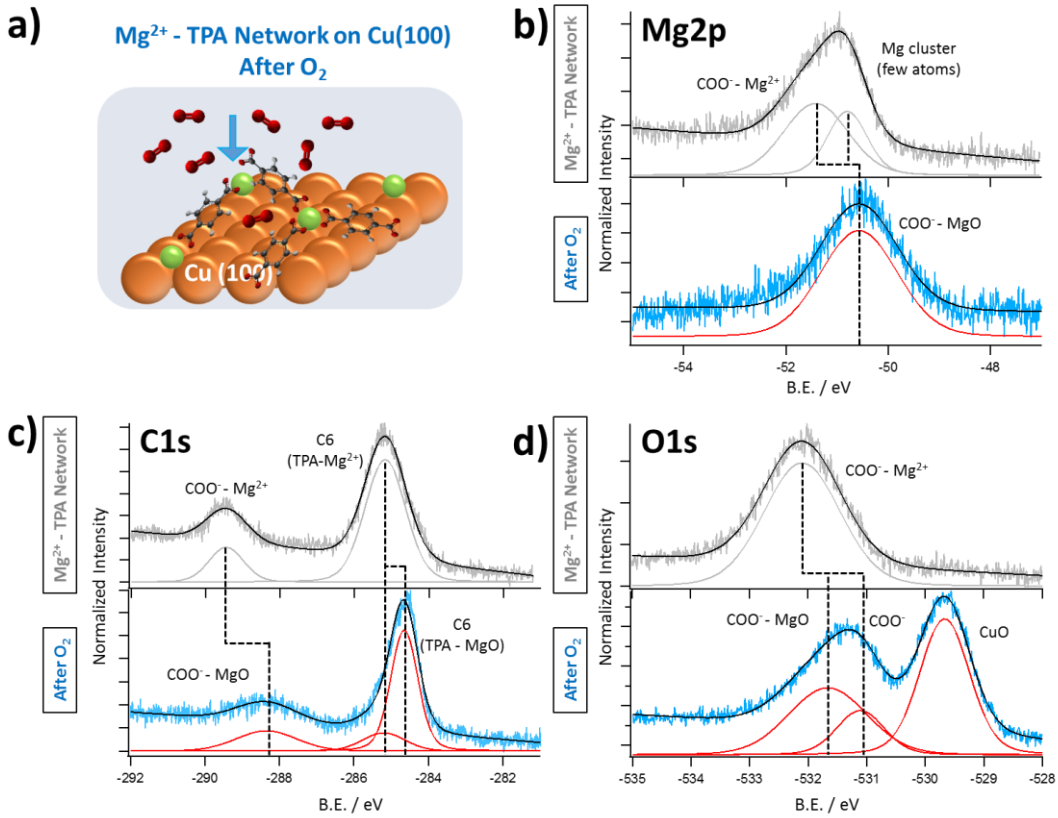

Figure 4.13: (a) Schematic representation of the typical Mg-3TPA network exposed to O_2 molecules. (b) HR-XPS spectra of the sample before (grey lineshape) and after (blue lineshape) being exposed to 500 L of O_2 in the (b) Mg2p, (c) C1s and (d) O1s energy regions.

The two peaks present in the C1s region are related also with the disassembly of the TPA molecules from the network. The prominent peak at lower binding energies is split in two peaks at **284.7** and **285.2 eV**. Thus, the peak at **284.7 eV** is characteristic for the carbons of the C6 ring in fully-deprotonated TPA molecules surrounding the MgO sites. This peak presents a higher relative area compared to the smaller peak at **285.2 eV** characteristic of the ionic networks, whose presence evidences the remaining of small domains with COO^--Mg^{2+} coordination. Hence, the broad peak at higher binding energies at **288.4 eV** is attributed to the wide range of contributions of the COO^- groups from the free molecules surrounding in a disordered fashion the MgO sites (as seen above in **Figure 4.11**). Finally, the Mg2p region shows a broad peak at

50.6 eV attributed to MgO species**.** Its shift to a lower binding energy would result from the effect of the CuO substrate [138], in a similar way as seen with bigger Mg clusters exposed to O_2 in **section 4.2**.

The results obtained by XPS agree well with the observations by STM and the DFT calculation. O_2^- chemisorbs on the Mg^{2+} centers and induces quenching of the charge without a total breakdown of the COO^--Mg^{2+} coordination. This implies that TPA molecules remain in a disordered configuration around the MgO sites, but they do not completely segregate to form a homo-molecular network.

4.5. TPA Molecules Deposited on Mg(0001)

As seen in the previous sections, the co-deposition of TPA molecules and Mg atoms on a Cu(100) surface forms ionic networks. The experimental and theoretical calculations shown that the structure was stabilized by electrostatic interactions of anionic TPA molecules (COO^-) surrounding a cationic center (Mg^{2+}). In addition, these ionic networks revealed that the Mg^{2+} center acts as an adsorption site for molecules of CO_2 or O_2.

In this regard, this section focuses in the use of a substrate of Mg(0001) as a different strategy to form ionic networks. The interest is to study the self-assembly of TPA molecules on the Mg surface. **Figure 4.14(a)** shows the scheme of a sub-monolayer coverage of TPA molecules deposited by thermal evaporation on an atomically clean surface of Mg(0001) at RT. HR-XPS measurements analyzed the chemical environment of the adsorbed species, **Figure 4.14(b)**. The spectrum in the C1s binding energy region shows two small peaks at **289.3** (C1) and **288.0** (C2) **eV**, characteristic of the carbon atoms from the carboxylic (-COOH) and carboxylate ($-COO^-$) groups, respectively [141]. Hence, the prominent peak at lower biding energies splits in two contributions at **285.0 eV** (C3) and **284.6** (C4)**,** attributed to the carbon atoms from the C6 ring from protonated and fully-deprotonated TPA molecules, respectively [141]. The peak areas between C1 and C3 present a 1:2.8 ratio, while between C2 and C4 present a 1:3.5 ratio. These values agree well with the expected 1:3 ratio between the carbon contributions in protonated or fully-deprotonated TPA molecules. Thus, these findings suggest the presence of at least two different molecular structures: a structure related to the self-assembly of protonated molecules (peaks C2 and C4), and a second structure based on the self-assembly of fully-deprotonated molecules (peaks C1 and C3).

The analysis of the spectra in the O1s energy region reveals three peaks related to different oxygen environments in the molecules. The two peaks at higher binding energies at **533.7** (O1) and **532.4 eV** (O2) are attributed to the hydroxyl (-OH) and carbonyl (-C=O) groups, respectively [141], [149]. These peaks are part of the COOH groups and indicate that some molecules remain protonated on the substrate. The energy gap difference of 1.3 eV evidences the formation of H-bonds between the COOH groups and confirms their molecular self-assembly [149]. Since O1 and O2 are the result of the two inequivalent oxygens from the COOH groups of TPA, their peak areas should present a 1:1 ratio [141], [149], [150]. Nevertheless, the O2 peak shows a slightly higher intensity than O1, giving a peak area ratio of 1:1.6. Fuhr et al., reported this increment as

the result of an additional contribution related to the H-bonding between the -OH and the -COO^- groups [142]. In fact, the -COO^- group is identified by the peak at lower binding energies at **531.1 eV** (O3) and evidences the deprotonation of some TPA molecules [141], [142], as a result of their interaction with the surface at RT.

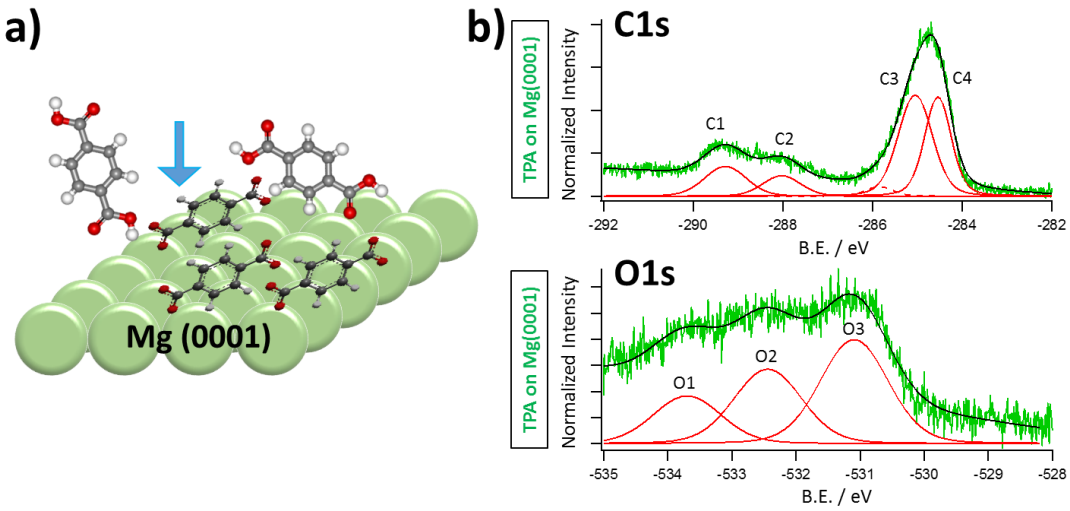

Figure 4.14: (a) Schematic representation of the deposition of TPA molecules on a Mg(0001) surface at RT. (b) The analysis of the HR-XPS spectra of TPA molecules deposited on Mg(0001) in the O1s and C1s energy regions, suggests the presence of protonated phase that turns into a fully-deprotonated phase.

Several works have reported that TPA molecules remain with their protonated COOH groups when they are deposited on low reactive surfaces such as a Ni(111) supported graphene layer, Al foil, Au(111) and Ag(111) at RT [150]–[153]. On the other hand, on more reactive surfaces such as Cu(100) and Pd(111), the full-deprotonation of the COOH groups of TPA occurs at RT (**Figure 4.4)** [141], [154]. Interestingly, some works reported the coexistence of the fully-deprotonated and the semi-deprotonated phase on Cu(100) at RT [141], [142]. Nevertheless, the semi-deprotonated phase is meta-stable and eventually the molecules fully-deprotonate after some minutes [141], [142] or with a slight increase in the temperature of the substrate [118]. Here, the existence of only a semi-deprotonated phase would imply that the peaks C1 and C2 would have a peak area ratio of 1:1; however, the intensity of C1 is 1.6 times higher than C2. Thus, the disproportions between C1/C2 and O1/O2 in the C1s and O1s regions respectively, evidence the presence of TPA in three states: protonated, semi-deprotonated and fully-deprotonated.

Figure 4.15 shows the typical STM image of the TPA molecules deposited on Mg(0001) at RT. The image reveals circular motifs characteristic of TPA molecules lying flat on the surface and forming big regular domains along the terraces. The detailed analysis of the structure shows the molecules arranged in a six-fold rotation symmetry characteristic of the hexagonal lattice. The proposed model on the right side shows fully-deprotonated molecules lying flat on the surface, with their molecular axis parallel to each other. The open circles represent the Mg atoms from

the Mg(0001) surface with a nearest neighbor distance of 3.19 Å [155]. The structure presents a squared-shaped unit cell (2x2) highlighted in green, with dimensions 6.4 x 6.4 Å that match twice the lattice constant (3.19 Å). The TPA molecules are bonded through eight H-bonds between the COO^- oxygens and the hydrogens from the C6 rings with the typical ionic coordination O···H-C. Although, in this model the unit cell shows three of the aromatic rings lying on the hollow sites and a fourth ring lying on the top site position of the Mg atoms from the substrate, this structure recalls a similar arrangement of the TPA molecules on Pd(111) [154]. In addition, this model also resembles the structure of the 3x3 phase formed on Cu(100) (**see Figure 4.4(b)**) [141].

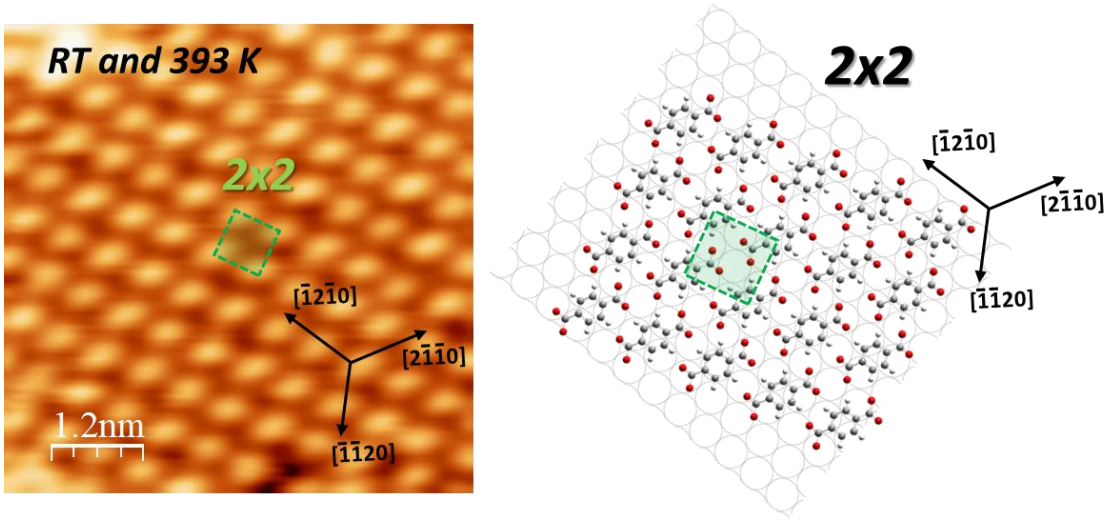

Figure 4.15: Typical STM image of the 2x2 phase obtained at RT. The tentative model shows the coordination of fully-deprotonated TPA molecules lying flat on the surface. The black, red and white balls represent the C, O and H atoms, respectively. The open circles represent the Mg atoms from the Mg(0001) surface. The unit cell is highlighted by the green square. The intermolecular interactions are formed through H-bonds between the COO^- oxygens and the hydrogens from the C6 rings. This structure can be found also after post-annealing up to 393 K.

From the observations above, it is implied that in comparison with other hexagonal surfaces, Mg(0001) presents a slight lower reactivity than Pd(111) [154], but a higher reactivity than Au(111) and Ag(111) [152], [153]. Thus, TPA remains intact when is deposited on Mg(0001) at RT and eventually the COOH groups fully-deprotonate with time to form homo-molecular networks. These observations agree well with the HR-XPS results shown in **Figure 4.14(b)**. As the semi-deprotonation of TPA molecules forms a metastable phase, its transition could occur sporadically by uncontrolled thermal variations in the surface by few degrees above RT [141]. Thus, the fully-deprotonation is induced by a slight thermal variation in the Mg(0001) surface above RT. This is confirmed by a post-thermal treatment of the sample up to 393 K that shows the presence of the fully-deprotonated 2x2 structure, as a predominant phase on the terraces. In contrast to the NH_2 group in TAPT molecules, the COO^- groups does not sequestrate adatoms from the substrate to form ionic networks. As a final test, the fully-deprotonated phase was exposed to 450 L of CO_2 (image not shown here). However, as also observed on Cu(100), the TPA

molecules on Mg(0001) did not show evidences of gas adsorption. This demonstrates that the COO^- groups do not act as active centers for CO_2 adsorption.

4.6. Conclusions

Inspired in the structure of the active site of RuBisCO, this chapter presented a method to synthesize a system based on a Mg^{2+} center stabilized by a carboxylate environment. In a similar way as it occurs in RuBisCO, the reactivity of the system was tested under high relative pressures of CO_2 and O_2 at RT.

The STM images showed that the deposition of Mg atoms on Cu(100) leads to the formation of Mg clusters. HR-XPS revealed that the exposure of the Mg clusters to a relative high pressure of CO_2 generates $MgCO_3$. On the other hand, a relative high pressure of O_2 oxidizes both the Mg clusters and the Cu surface. Aside, the full-deprotonation of TPA molecules on Cu(100) at RT, turned them into candidates to provide the carboxylate environment around a center of Mg^{2+}. Then, the analysis from STM and XPS experiments revealed that the fully-deprotonated TPA molecules do not react upon relative high-pressures of either CO_2 or O_2.

The co-deposition of TPA molecules with Mg atoms on Cu(100) at RT, resulted in the formation of a 2D ionic network. The typical unit cell is formed by a single Mg^{2+} cation surrounded by three deprotonated TPA molecules (Mg-3TPA). The structure was stabilized by the electrostatic interaction between Mg^{2+} cations and anionic TPA molecules. The ionic networks show structural evidence of gas adsorption upon exposure to either CO_2 or O_2. The CO_2 molecules physisorb temporarily on Mg^{2+}, producing a charge imbalance that produced a phase transition into a different configuration (Mg-4TPA). On the other hand, O_2 chemisorbs on the Mg^{2+} center, giving rise to a distortion in the metal-organic bonds that eventually leads to the collapse of the structure. In both cases, the phase transitions were irreversible in the period of few hours.

Finally, the deposition of TPA on a Mg(0001) surface was studied as an alternative route to form ionic networks. Nevertheless, after deposition the molecules remained intact on the surface. Eventually, the effect of the substrate turn them into a fully-deprotonated state that could be achieved also after post annealing at 393 K. Indeed, the fully-deprotonated TPA molecules formed homo-molecular networks but they did not show reactivity with CO_2, as expected from the chemistry of the COO^- groups.

The 2D ionic networks presented here are good model systems for surface reactivity studies at RT. These 2D biomimetic analogues of RuBisCO are expected to be a versatile structure, which could allow interactions with further NH_2 groups to form a more accurate replica of the active site of RuBisCO. For instance, the ability of TAPT to coordinate with adatoms from the host substrate, could form novel ionic structures with two different functional groups on Mg(0001). The next chapter studies these possibilities.

Chapter 5: Formation of Hybrid Metal-Organic Networks with TAPT and TPA molecules on metal surfaces

The study of supramolecular systems formed by the interaction of two different molecular species is attractive because of their flexibility to form a wide variety of structures which can perform diverse tasks in organic electronics [108] or host-guest assembly [156]. These hetero-molecular structures are formed by the strong interaction between molecules with H-bond acceptors and donors, which can overcome the structural effects of the underlying substrate [40], [157], [158]. Molecules with NH_2 functional groups act as H-bond donors, while their semi-deprotonated state (NH) gives them the additional behavior of H-bond acceptors. These characteristics allow them to form homo-molecular networks on metal surfaces at RT [78]. On the other hand, molecules with COOH functional groups can act as H-bond donors and acceptors, while their fully-deprotonated state (COO^-) allows them to act only as H-bond acceptors. Thus, they can also form homo-molecular structures on metal-surfaces at RT [141], [142].

As it was presented in the first Chapter, the active site of the RuBisCO enzyme is based on amino acid residues whose structures mostly terminate in COOH and NH_2 functional groups, and that is why it is desired to study hetero-molecular systems formed by the joint interaction of both functional groups. Even though the NH_2 or COOH groups can form hetero-molecular networks with other molecular functional groups [91], [157], [159]–[162], there are few reports studying their direct interaction [159]. Interestingly, in some cases the NH_2 groups can dehydrogenate to sequestrate and coordinate with adatoms from the host substrate [32], [96], [116]; as has been presented in Chapter 3. Whereas, in the presence of metal adatoms, the COO^- groups can form either metal-organic coordination [29], [30] or ionic networks [23], [24]; as has been presented in Chapter 4. These particular features encourage the formation of metallic-hetero-molecular systems, which indeed include COO^- and NH_2 functional groups as well as a metal adatom in the structure. Few reports have shown that the co-deposition of two molecules with COOH groups and pyridyl groups forms metallic-hetero-molecular networks with the adatoms of the host metal surfaces. These arrays show that the molecules form a mixed phase that involves H-bonds (molecule-molecule) and the metal-organic (molecule-adatom) coordination [163], [164].

The main goal of this thesis is focused in the replication of the active site of RuBisCO whose structure presents: a lysine molecule with an NH_2 group (before its carboxylation with a CO_2 molecule) and molecules with COO^- functional groups electrostatically bonded to a Mg^{2+} center [3], [11]. **Chapter 3** showed that a molecule with NH_2 groups such as TAPT, can semi-

deprotonate (NH) and coordinate adatoms from the host substrate. Whereas **Chapter 4** showed that a molecule with COOH groups such as TPA, can deprotonate into COO^- and form ionic bonds with Mg^{2+} cations. These characteristics encourage their use to mimic the structure and the catalytic function of RuBisCO for the absorption and transfer of CO_2 into organic molecules [165], [166]. Therefore, in this chapter, the self-assembly of TPA and TAPT molecules co-deposited on substrates of Cu(100) or Mg(0001), is studied under UHV at RT conditions.

5.1. Experimental Setup

The experiments were performed in an UHV chamber with a base pressure of $5.0x10^{-10}$ mbar. Single crystals of Cu(100) or Mg(0001) were used as substrates. Their surfaces were cleaned following the standard procedures as described in **Chapter 2**. TPA and TAPT molecules were co-deposited by thermal evaporation from a quartz crucible by heating it up to 448 and 513 K, respectively. During molecular deposition, the pressure in the chamber reach a maximum of $2.0x10^{-9}$ mbar, while the temperature of the substrate was hold at RT. The analysis of the surface was performed in situ using a homemade STM operating in constant current mode at RT. The STM images were taken with a tungsten tip, applying a sample bias of -1V and a tunneling current of 1.0 nA.

5.2. Hetero-molecular networks of TPA and TAPT on Cu(100)

Sub-monolayer coverages (0.08 ML) of TPA and (0.2 ML) TAPT molecules were sequentially deposited by thermal evaporation on an atomically clean Cu(100) surface at RT. The STM image in **Figure 5.1(a)** reveals small 2D structures while the black arrows indicate their tendency towards 1D arrangements (inset image). A closer inspection of the surface (**Figure 5.1(b)**) reveals complex structures formed by the interaction of TAPT and TPA molecules, identified by the three-spoked and rounded-shape geometries, respectively. These features suggest that both molecules are absorbed in a planar geometry with their backbones oriented parallel to the surface (see **Chapters 3** and **4**).

The area highlighted with the green rectangle shows some TAPT molecules forming a 1D structure; however, this arrangement differs from the characteristic chain-like structure observed in **Chapter 3**. The difference is centered in the presence of TPA molecules along the backbone of the 1D arrangement, which suggests the interaction between both molecules. In fact, these interactions are evidenced by the 2D corral-like structure formed at expenses of a 1D chain, as highlighted with the yellow circle. On the other hand, the structure enclosed by the white-dashed rectangle is analyzed in detail in **Figure 5.1(c)**. The presence of two typical TAPT pairs forming a small 1D chain evidences the semi-deprotonation of NH_2 groups (NH) from TAPT molecules and their coordination with Cu adatoms. Hence, the modeled structure superimposed on top of the image agrees well with the structural characteristics of the metal-organic structure (TAPT-Cu) studied in **Figure 3.3** in **Chapter 3**. In fact, the Cu adatoms (green circles) are distinguished by the protrusions besides the functional groups of the TAPT molecules (indicated by the white arrows).

Hence, the attachment of TPA to TAPT molecules does not prevent the formation of the metal-organic TAPT pairs. This would be related to a deficit in the amount of TPA molecules that leave

some TAPT molecules free to interact with the adatoms from the substrate. Thereby, increasing the amount of TPA molecules may prevent the formation of metal-organic chains of TAPT-Cu.

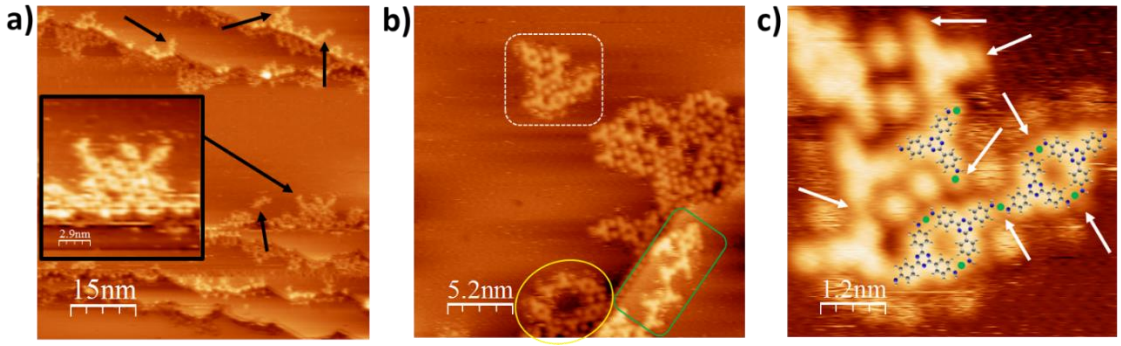

Figure 5.1: (a) The co-deposition of TPA and TAPT molecules on Cu(100) at RT results in 2D structures with a tendency to form 1D arrangements (black arrows and inset image). (b) A closer look reveals the complexity of the structures formed by the interaction of TAPT and TPA molecules. The green rectangle highlights a 1D arrangement formed with TAPT molecules, while some TPA molecules attach to the backbone. The yellow circle highlights the interactions between both molecules, which forces the TAPT molecules to form a corral-like structure. (c) Zoom-in of the area highlighted by the white square in (b). The metal-organic features indicate that the TAPT molecules are semi-deprotonated and coordinate Cu adatoms (structure superimposed on top of the image).

Accordingly, sub-monolayer coverages (0.4 ML) of TPA and (0.3 ML) TAPT molecules were sequentially deposited on an atomically clean Cu(100) surface at RT. **Figure 5.2** reveals extended networks nucleating either from the step edges or from the terraces. As the preparation of the sample started with the deposition of TPA molecules, then the COOH groups of TPA are expected to be fully deprotonated (COO^-). However, after several scans, the formation of the typical 3x3 homo-molecular structure (TPA-TPA) was not observed (**Figure 4.4** in **Chapter 4**) [141]. On the other hand, the images did not show the presence of metal-organic TAPT-Cu chains, as an indication that the NH_2 groups of TAPT molecules remain intact. In fact, the zoom-in of the surface, on the right side of the image, reveals two well-differentiated 2D hetero-molecular structures labeled as **TPA_3TAPT_2** and **TPA_8TAPT_2**. The structure of **TPA_3TAPT_2** presents a unit cell (purple parallelogram) with a TPA:TAPT molecular ratio of 3:2. Whereas the structure **TPA_8TAPT_2** presents a unit cell (green parallelogram) with a TPA:TAPT molecular ratio of 8:2. This confirms that the excess of TPA with respect to TAPT molecules prevents the semi-deprotonation of TAPT and thus, the formation of TAPT-Cu. In this regard, the characteristic 3x3 structure is not observed because the C-O···H bonds are weaker than the N-H···O bonds (TPA-TAPT > TPA-TPA) [167]–[169].

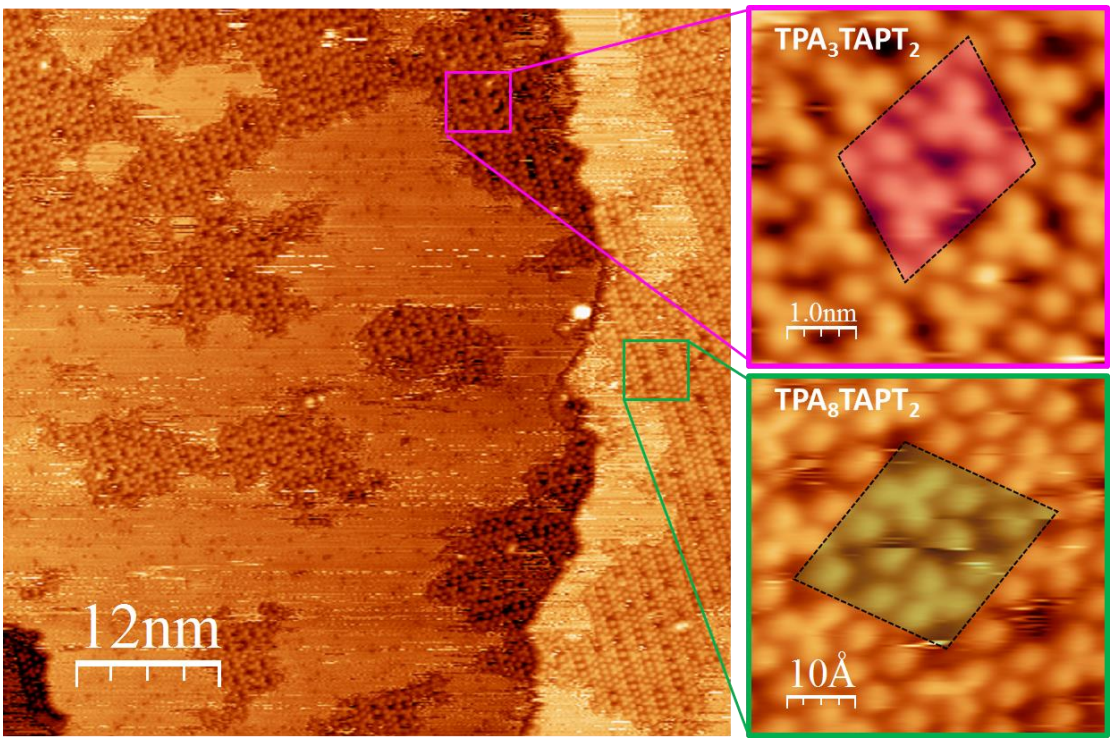

Figure 5.2: Overview STM image of the Cu(100) surface covered by extended networks across the terraces at RT. The inset images at the right side show the zoom-in of the surface that reveals the formation of two hetero-molecular structures: TPA_3TAPT_2 and TPA_8TAPT_2, whose unit cells are represented by the purple and green parallelograms, respectively. In both cases, there exist an excess of TPA respect to TAPT molecules.

Details of the **TPA_3TAPT_2** model are shown in **Figure 5.3(a)** and we propose a structure with fully deprotonated TPA molecules and intact TAPT molecules. In the unit cell, the NH_2 groups of the TAPT molecules present one bi-dentate and two mono-dentate couplings with the carboxylate O from three different TPA molecules (N-H···O); whereas, TPA molecules additionally bind among them through C-O···H bonds. White arrows in **Figure 5.3(b)** indicate small circular features with a diameter of 0.3 nm, which do not form part of the main structure and lie trapped between the molecules. To determine their nature, the image was analyzed in three different areas labeled as Area (i), Area (ii) and Area (iii). Area (i) shows the collapse of the structure and the presence of a TAPT pair with two small protrusions in between. This feature is typical of a metal-organic coordination and evidences the semi-deprotonation of the NH_2 groups. In this regard, Area (ii) shows the presence of two protrusions in the missing part of a TPA molecule. The closeness of each protrusion to the TAPT molecules is related to the coordination of a Cu adatom with the N from the semi-deprotonated NH_2 group. Finally, Area (iii) shows the protrusions (Cu adatoms), trapped in between the pores of the structure.

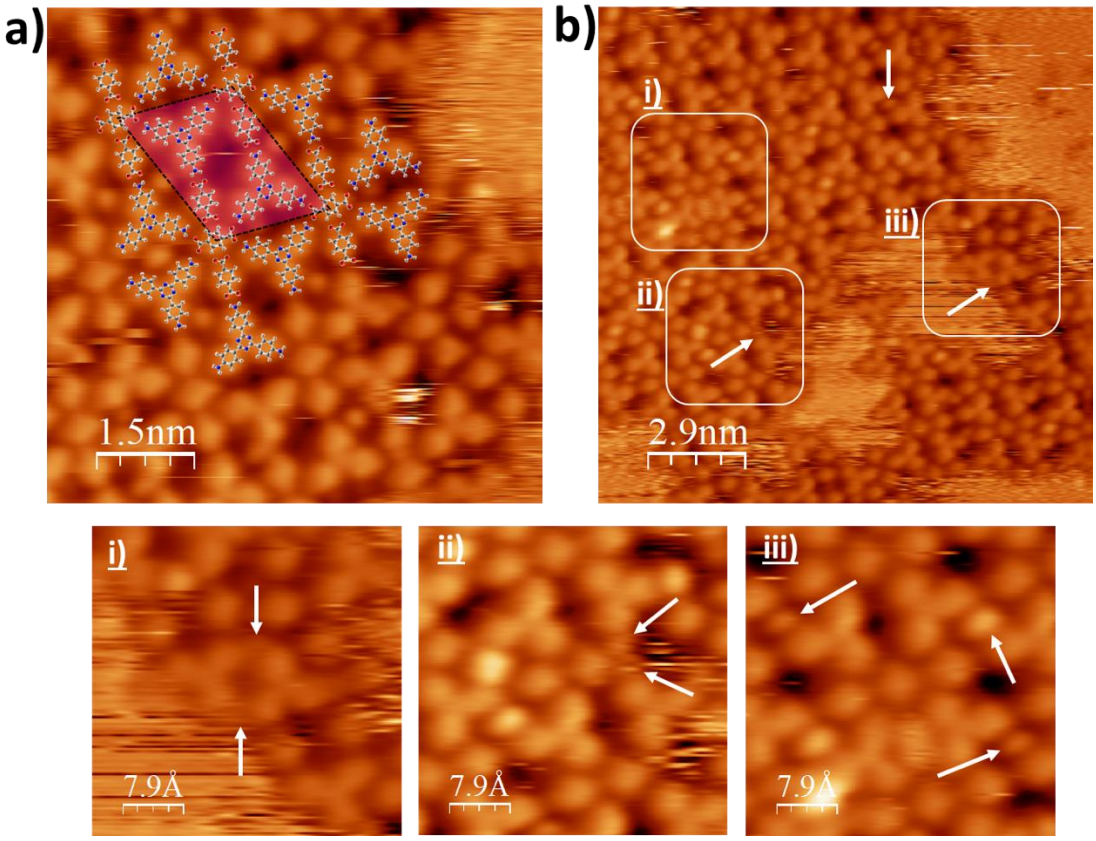

Figure 5.3: (a) Proposed model of **TPA_3TAPT_2** that includes fully-deprotonated TPA and protonated TAPT molecules interacting through H-bonds. (b) Zoom-in of the surface reveals that the structure can contain Cu adatoms indicated by the white arrows. (i) The Cu adatoms are observed between two semi-deprotonated TAPT molecules and form the typical metal-organic TAPT pair. (ii) Two semi-deprotonated TAPTs lose their H-bond with a TPA molecule to coordinate with two Cu adatoms (iii) The Cu adatoms are observed lying inside the pores of the structure.

On the other hand, **Figure 5.4(a)** proposes the model of the more complex **TPA_8TAPT_2** structure. This structure is also stabilized purely by H-bonds between the COO^- and the NH_2 groups of TPA and TAPT molecules, respectively. In the unit cell, the NH_2 groups of the TAPT molecules present four mono-dentate couplings with the carboxylate O from four TPA molecules (N-H···O) and each TPA, additionally binds with other TPA molecule through four C-O···H bonds. The **TPA_8TAPT_2** structure contains more TPA molecules and more C-O···H bonds (compared to the **TPA_3TAPT_2** structure). The high content of TPA molecules evidences the first stages in the formation of the hetero-molecular networks, towards a thermodynamic stability; which involves the introduction of TAPT molecules into the previously formed homo-molecular networks of TPA molecules [168]. The white arrows in **Figure 5.4(b)** show that this structure contains also Cu adatoms trapped between the molecules. Thus, the structure was analyzed in three different parts: labeled as Area (i), Area (ii) and Area (iii). Area (i) shows that the semi-deprotonation of the NH_2 group in two TAPT molecules replaces a missing TPA molecule by two Cu adatoms. On the other

hand, Area (ii) shows two Cu adatoms trapped in the gap formed between two TAPT molecules. Whereas, Area (iii) shows a bigger rounded feature with an average diameter of 0.7 Å, which suggest that the pores can also trap TPA molecules.

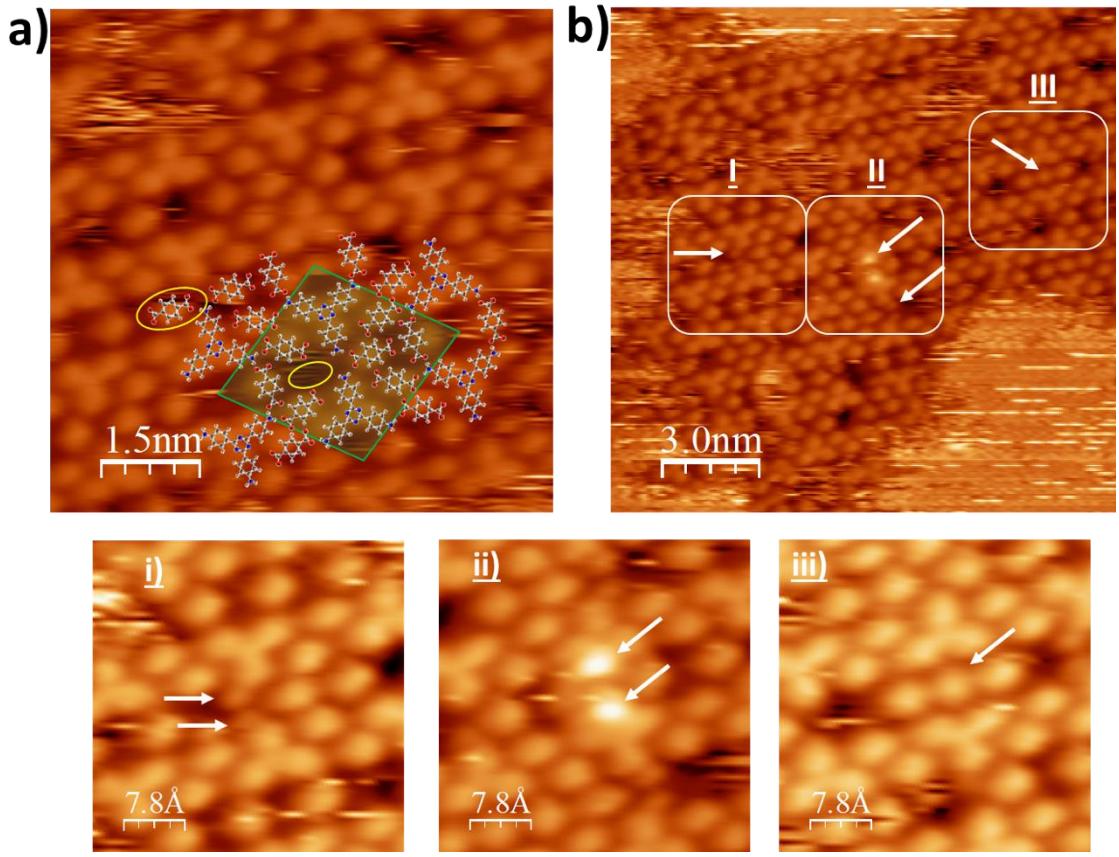

Figure 5.4: (a) Proposed model of **TPA_8TAPT_2** that includes fully-deprotonated TPA and protonated TAPT molecules interacting through H-bonds. The yellow circle indicates a TPA molecule missing inside the unit cell. (b) Zoom-in of the surface revealing that the structure can contain Cu adatoms, as indicated by the white arrows. (i) Two semi-deprotonated TAPT leave behind their H-bond with a TPA molecule to coordinate with two Cu adatoms. (ii) The Cu adatoms are lying inside the pores of the structure. (iii) The pores can also trap TPA molecules.

These observations confirm that the molecular interactions are through H-bonds [168]–[170]. Interestingly, some TAPT molecules semi-deprotonate and lose the N-H···O bond with a TPA molecule which is replaced by the incorporation of Cu adatoms coordinated with NH groups. In addition, the structures of these hetero-molecular networks present pores which can act as trapping sites for guest molecules [171], [172] or metal adatoms [43], [173]–[175] without leading to the collapse of the network.

Finally, these structures were exposed to 500 L of CO_2; however, there was no evidence of CO_2 interaction with the hybrid network (images not shown). This was expected as neither COO^-, NH_2 nor the Cu adatoms act as active centers, as it was described in Chapters 3 and 4.

5.2.1. Incorporation of Mg adatoms in the hetero-molecular structure

The characteristic of these hetero-molecular networks to trap metal adatoms without the breakdown of the structure makes them attractive to study the incorporation of Mg atoms. As we described above, the main goal is to form a structure with a Mg center that resembles the structure of the active center of RuBisCO.

TPA_3TAPT_2 was chosen as a model structure because of the proportionate TPA/TAPT ratio. Nevertheless, as shown in **Figure 5.5(a)**, the addition of Mg atoms promotes the partial dissociation of the network. A closer look reveals that the former structure remains in some areas, as highlighted by the white square. The partial disassembly is attributed to the affinity of Mg^{2+} to the COO^- groups from TPA molecules, which produces agglomerations (indicated by white arrows). According to this evidence, the ionic coordination Mg-TPA seems to be stronger than the H-bonded TPA-TAPT interactions (Mg-TPA > TPA-TAPT). In fact, **Figure 5.5(b)** shows that the lower availability of TPA leaves TAPT molecules spread randomly on the surface and free to semi-deprotonate and coordinate with Cu adatoms to form metal-organic TAPT pairs or small 1D chains (as indicated by the white arrows). Finally, as seen above in **Figure 3.7** on **Chapter 3**, it is worth to consider that TAPT may also show affinity to the Mg atoms, which prevents the formation of longer TAPT-Cu metal-organic chains. The formation of a hetero-molecular structure with a Mg center on a Cu(100) surface is not likely to happen due to the selectivity of each molecule to a certain metal center (a competence between the Cu and Mg adatoms), which leads to a phase separation [176]. This shows the incapacity of Mg to form a well-defined structure with both TPA and TAPT molecules on Cu(100). However, these results confirm that Mg is a good candidate to form ionic networks with TPA, and also that it shows affinity to the TAPT molecules on Cu(100).

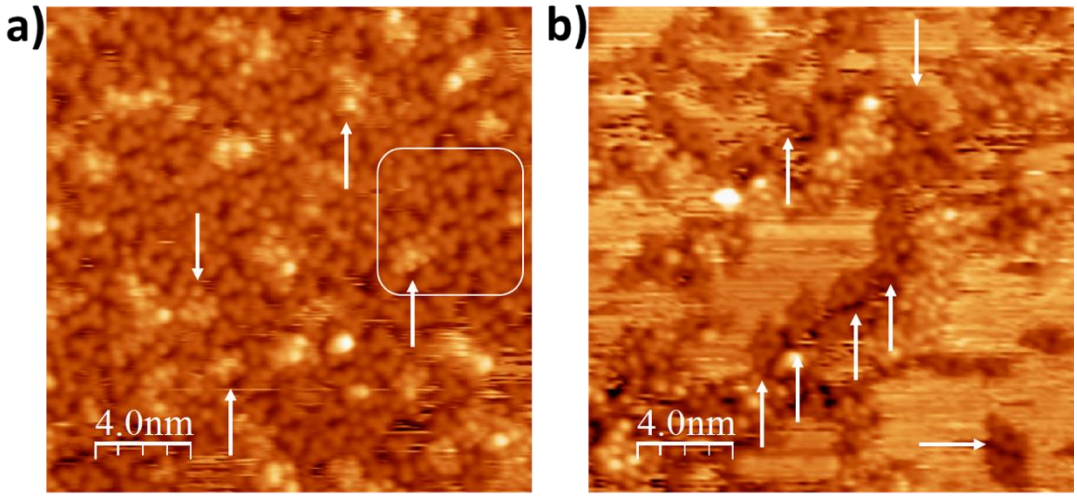

Figure 5.5: (a) The deposition of Mg atoms on the hetero-molecular network **TPA_3TAPT_2**, promotes the partial disassembly of the structure (White Square). The formation of agglomerations (indicated by the white arrows) evidences the preference of Mg to form a COO^--Mg^{2+} ionic coordination. (b) The TAPT molecules are left behind and semi-deprotonate to form metal-organic coordinated chain-like structures with the Cu adatoms (Indicated by the white arrows).

5.3. Metal-organic networks of TPA with TAPT on Mg(0001)

The previous section showed that the co-deposition of TPA and TAPT molecules on Cu(100) forms H-bonded hetero-molecular networks. Nevertheless, the introduction of Mg atoms formed Mg-TPA ionic networks while the TAPT molecules preferred to coordinate with the Cu adatoms from the Cu(100) substrate. This resulted in the disassembly of the structure. Hence, to prevent the effect of the Cu adatoms from the surface, this section studies the co-deposition of sub-monolayer coverages of TPA and TAPT molecules on an atomically clean Mg(0001) substrate at RT, followed with a post-annealing at 403 K for 30 minutes.

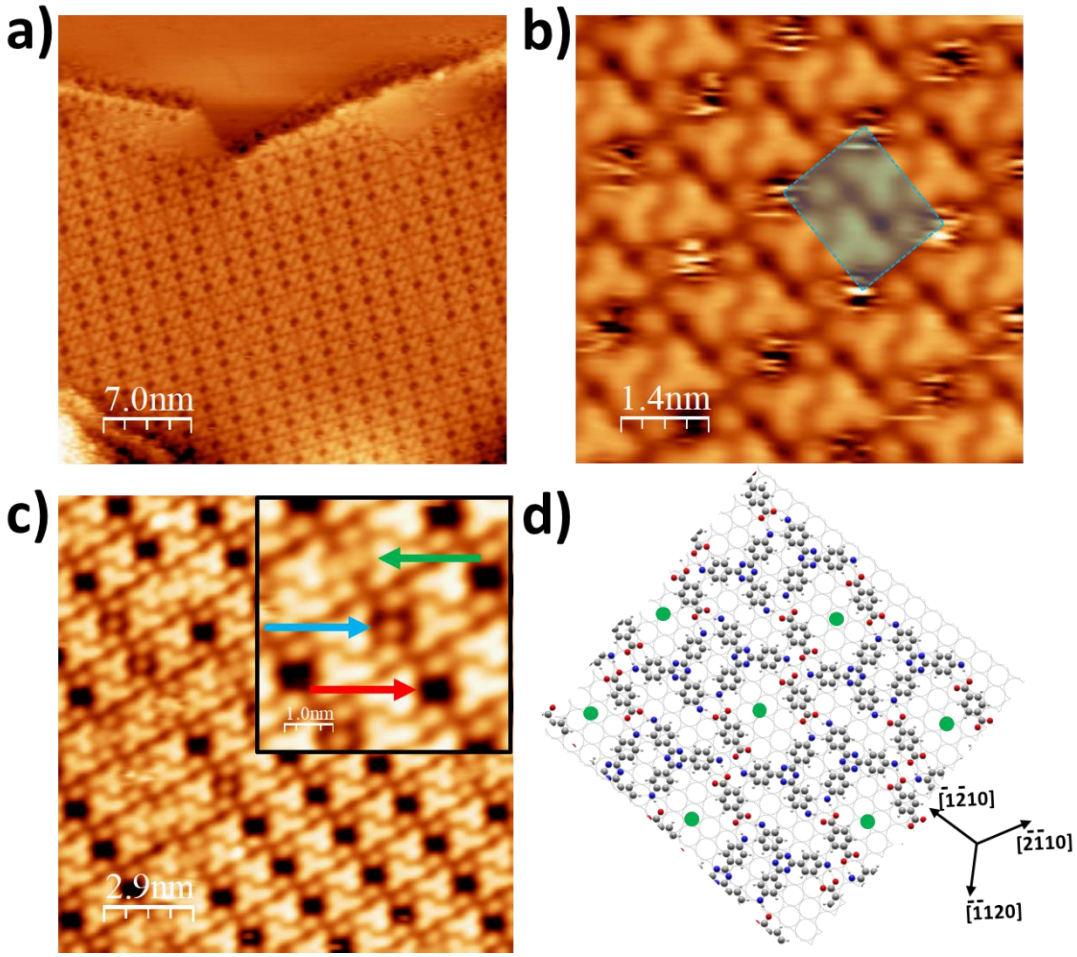

Figure 5.6: (a) Overview STM image showing that the co-deposition of TPA and TAPT molecules on Mg(0001) forms large, uniform and porous domains, covering big extensions of the surface. (b) The zoom-in identifies a rectangular unit cell with a TPA:TAPT ratio of 2:2, highlighted by the blue square. The fuzzy lines correspond to Mg^{2+} cations trapped inside the pores (c) Depending of the tip conditions, the Mg^{2+} cannot be detected and therefore the pores are presented as black hollows (red arrow). The Mg^{2+} can be immobilized by the presence of a second Mg^{2+} or a TPA molecule (green and blue arrows, respectively). (d) The model of the **$[Mg_1(TPA)_2(TAPT)_2]$** network proposes a structure formed by semi-deprotonated TAPT and fully-deprotonated TPA molecules interacting through H-bonds. The molecular arrangement of the NH and COO^- groups forms a high electronegative environment that traps the Mg adatoms from the surface.

The STM image in **figure 5.6(a)** reveals the formation of extended and highly ordered supramolecular 2D structures covering large surface areas (0.7ML). The zoom-in of the structure presented in **Figure 5.6(b)** reveals the presence of TAPT and TPA molecules, identified by their characteristic three-fold rotation symmetry and the rounded-shape features, respectively. Both molecules interact with each other to form a complex structure referred as **$[Mg_1(TPA)_2(TAPT)_2]$**. This structure presents a rectangular unit cell (highlighted in blue) with a TPA:TAPT molecular ratio of 2:2. The most remarkable feature is the presence of pores resulting from the molecular arrangement [177]. The fuzzy lines inside the pores are attributed to trapped Mg adatoms [174], [175] in a resonant state, where delocalization prevents a clear observation. Thus, depending on the tip conditions, the Mg adatoms may seem invisible inside the pores **(Figure 5.6(c))**. The red arrow in the inset image indicates the pores presented as black hollows that indeed are filled with one Mg adatom. An extensive analysis shows that the Mg trapped inside the pore can be immobilized by either a second Mg adatom (green arrow), or an adsorbate such as a TPA molecule (blue arrow). These findings show that the pores can act as active sites to fix different adsorbents. Thus, the co-deposition of TPA and TAPT molecules forms porous metal-hetero-organic networks with trapped Mg adatoms, evenly spaced along the structure.

The information extracted from the previous chapters helped to define the nature of the molecular interactions. TPA and TAPT molecules can fully- and semi-deprotonate on Mg(0001), respectively at RT. **Chapter 4** showed that in the case of TPA, the fully-deprotonated molecules are unable to form a Mg-TPA coordination on Mg(0001), but they can assemble into a H-bonded homo-molecular structure (TPA-TPA). Whereas, **Chapter 3** showed that the semi-deprotonated TAPT molecules sequestrate Mg adatoms to form a structure stabilized by both N-H···N and metal-organic coordination (TAPT-Mg). In previous chapters, it was also shown that a post-annealing at 373 K enhanced the fully- and semi-deprotonation of both TPA and TAPT molecules, respectively. However, when both molecules are co-deposited on Mg(0001) and post-annealed at 373 K, none of these homo-molecular or metal-organic structures were observed along the terraces. This suggests the existence of a stronger interaction than the TPA-TPA and TAPT-Mg. Considering the information from the previous section, the **$[Mg_1(TPA)_2(TAPT)_2]$** structure presents a balanced amount of TPA and TAPT molecules (2:2 ratio) which may enhance the H-bond interactions (N-H···O). Therefore, taking also into consideration that the substrate of Mg(0001) presents low reactivity, the N-H···O interactions between TPA and TAPT molecules turn predominant [167].

The tentative model shown in **Figure 5.6(d)** presents a structure stabilized by H-bonds between fully-deprotonated TPA (COO^-) and semi-deprotonated TAPT (NH) molecules. Thus, every TPA forms five H-bonds with the molecules around. Three of the four carboxylate O from every TPA molecule form H-bonds with the NH groups from three different TAPT molecules (O···H-N). A fourth carboxylate O forms an additional H-bond via the phenyl ring of a TAPT molecule (O···H-C) and finally one more H-bond is formed through the phenyl ring of TPA and the NH group of a fourth TAPT (H···N-C). Indeed, the functional groups of the molecules provide a high electronegative environment to the pores. Therefore, the delocalized Mg atom trapped inside the pores should be in its cationic form (Mg^{2+}). The deposition order of the molecules was not considered as an important factor since a post annealing always followed the self-assembly

process. The fact that TPA and TAPT molecules interact cooperatively with each other instead of forming isolated homo-molecular networks of TPA or metal-organic networks (MONs) of Mg-TAPT, demonstrates the robustness of this structure.

5.4. Studying the action of Mg as an active center in the networks

The co-deposition of TPA and TAPT molecules on Mg(0001) forms a metal-organic network with pores containing Mg^{2+} cations, which can eventually adsorb TPA molecules. Thus, the pores could also work as adsorption sites for gas molecules. Therefore, this section evaluates the catalytic function of this metal-hetero-molecular network.

5.4.1. Metal-hetero-molecular Networks exposed to O_2

A typical **$[Mg_1(TPA)_2(TAPT)_2]$** structure was exposed to high relative pressures of O_2. As observed in **Figure 5.7**, the main structure barely changes upon 650 L of O_2; only small structural changes are seen in the domain boundaries, where the bare surface oxidizes and displaces the molecules (regions indicated between the yellow arrows). In contrast to the Mg-3TPA ionic networks that show a phase transition when they interact with either CO_2 or O_2 molecules (**Chapter 4**), the **$[Mg_1(TPA)_2(TAPT)_2]$** networks do not show evidence of O_2 adsorption as the structure remains invariable in an O_2 environment. Hence, these networks could act as passivation layers to prevent oxidation on the surface.

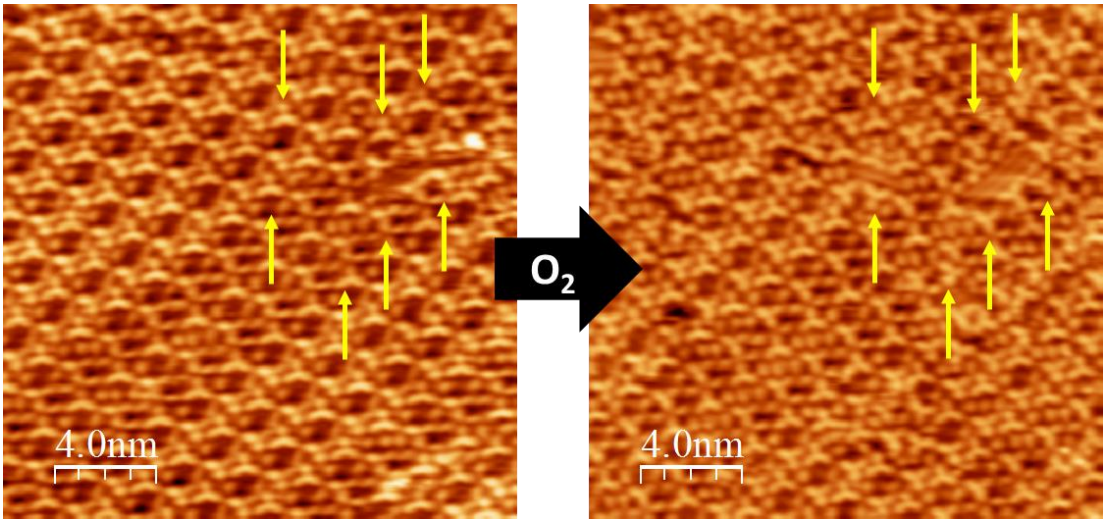

Figure 5.7: **$[Mg_1(TPA)_2(TAPT)_2]$** structure after 650 L of O_2. The main structure does not change but a displacement of the molecules related to the oxidation of the bare surface (not covered by the molecules) at the domain boundaries, is observed.

5.4.2. Metal-hetero-molecular Networks exposed to CO_2

Figure 5.8 shows the typical **[$Mg_1(TPA)_2(TAPT)_2$]** structure exposed to a relative high pressure of CO_2. After 760 L of CO_2, the areas indicated by white arrows show structural changes. The zoom-in of the surface (images in the inset) shows that CO_2 promotes the disassembly and the re-orientation of a TAPT molecule toward the pore of the network.

A similar behaviour was observed in **Chapter 3**, where the interaction of CO_2 with the NH groups of TAPT formed carbamates, which triggered the mobility of carboxylated TAPT molecules towards a phase transition. In addition, it was shown in **Chapter 4** that both a CO_2 molecule and the COO^- groups of TPA have affinity to Mg^{2+} ions. Despite the fact that the mechanism behind the interaction of CO_2 with the **TPA-TAPT@Mg-I** network is not well established yet, it is proposed that CO_2 breaks the weakest H-bond between two TAPT molecules (N···H-N), and coordinates with the free NH group to form eventually a carbamate. Thus, the re-orientation of the TAPT molecule is regarded to the ionic attraction of the COO^- group of the carbamate to the Mg^{2+} center in the pore. This behavior is similar to the mechanism found in the active site of RuBisCO: a CO_2 molecule binds the NH group of a lysine molecule to form a carbamate that is electrostatically bound to the Mg^{2+} center.

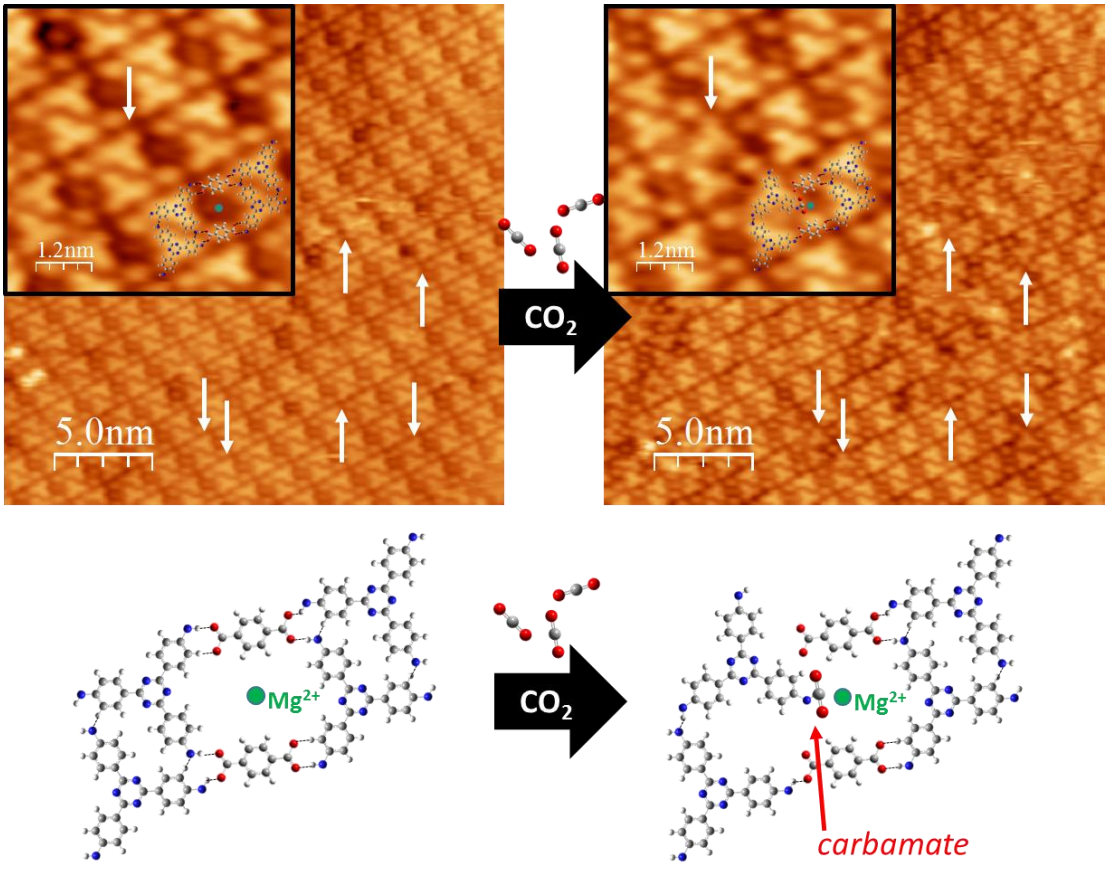

Figure 5.8: A **[$Mg_1(TPA)_2(TAPT)_2$]** network exposed to 760 L of CO_2. Local changes in the structure gives some evidences that a carbamate is formed and it further interacts electrostatically with the Mg^{2+} center.

5.5. Formation of 3D metal-hetero-organic structures for gas adsorption

As it was shown above, the Mg^{2+} ions inside the pores can be immobilized by the presence of adsorbents such as gas and organic molecules. This presents the pores as active sites as well as precursors of 3D structures, which can be utilized as model systems for gas storage in MOFs.

A **$[Mg_1(TPA)_2(TAPT)_2]$** network was used as a template to deposit 0.35 ML of extra TPA molecules. **Figure 5.9(a)** shows that TPA molecules deprotonate and form the typical 2x2 homo-molecular structure on the empty areas of the bare surface. However, the most outstanding observation is that TPA molecules lie on the network to fill the pores **(inset image)**. This structure will be referred as **$[Mg_1(TPA)_3(TAPT)_2]$**. It is observed also that some pores did not get fill and the Mg^{2+} is still resonating inside the pores (fuzzy lines). A seen in the proposed model of **Figure 5.9(b)**, a TPA molecule can barely fit inside in a planar configuration due to the high electronegativity of the pore. In addition, the TPA molecules that is trapped inside the pore presents a different contrast with the surrounding TPA molecules. Thus, the model proposes the apical attachment of the TPA molecule on the Mg^{2+} ion. This apical coordination gives insight in the formation of 3D networks.

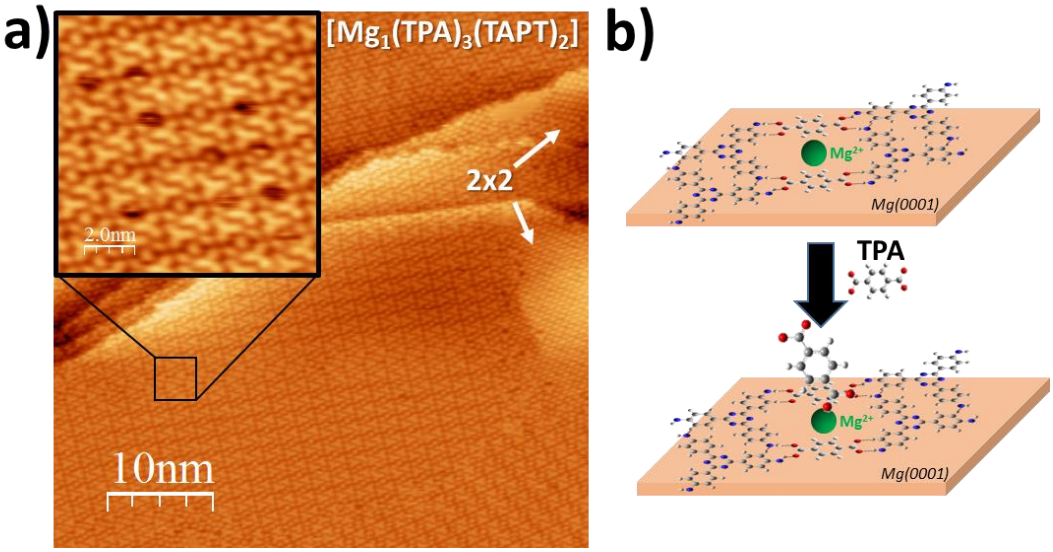

Figure 5.9: (a) Typical **$[Mg_1(TPA)_3(TAPT)_2]$** structure formed by the deposition of TPA molecules on a pre-existing **$[Mg_1(TPA)_2(TAPT)_2]$** network. The excess of TPA molecules does not alter the structure but either forms 2x2 homo-molecular networks on the bare Mg surface or adsorbs on the pores (inset image). (b) The model proposes the apical attachment of the TPA molecules on the Mg^{2+} sites trapped inside the pores.

Following, additional 0.35 ML of TAPT molecules were deposited on the **$[Mg_1(TPA)_3(TAPT)_2]$** structure, followed by a post annealing at 403 K. Thus, **Figure 5.10(a)** shows the structure obtained after two deposition cycles on Mg(0001): each cycle refers to the standard process to

form the **[$Mg_1(TPA)_2(TAPT)_2$]** structure which involves the co-deposition of TPA and TAPT with a post annealing at 403 K. The STM image shows domain boundaries that segregate different molecular organizations. The analysis of the domains reveals the presence of the pre-existing structure **[$Mg_1(TPA)_3(TAPT)_2$]** and two more different structures which may grow in a topmost layer.

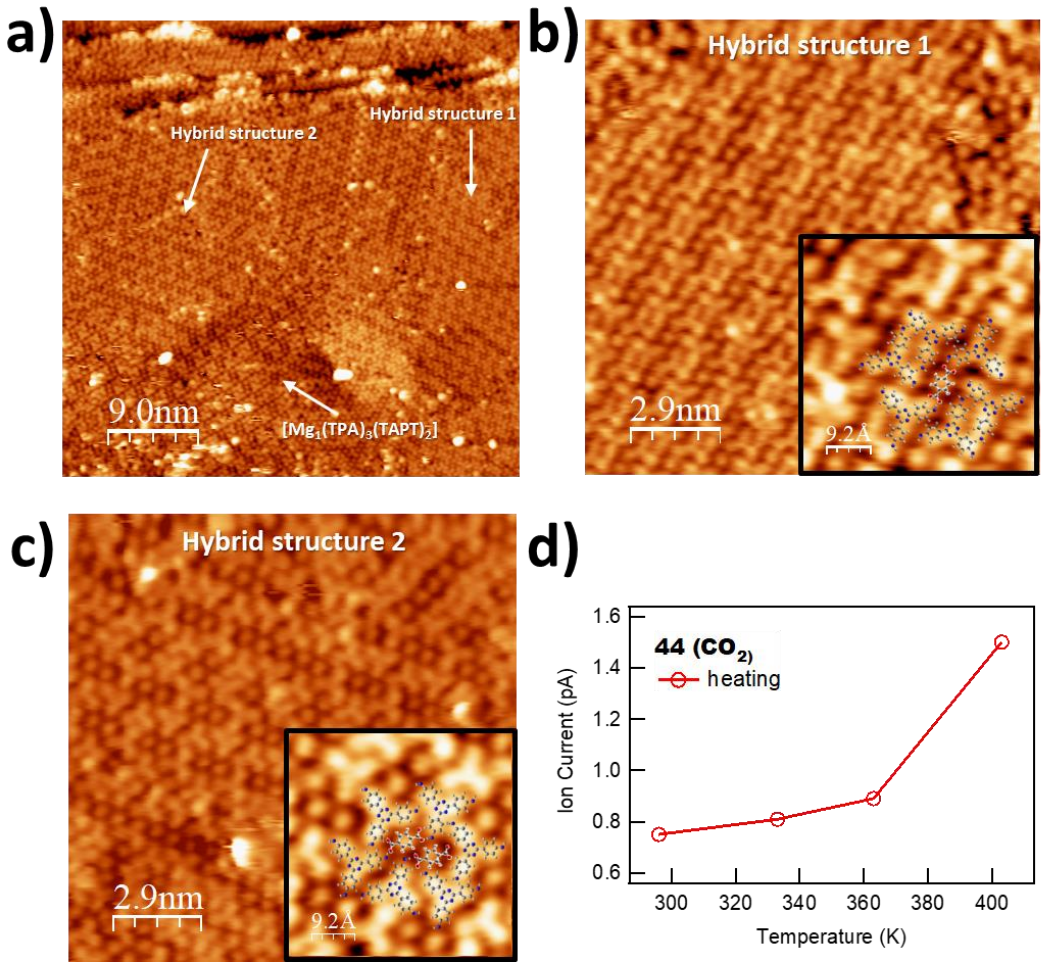

Figure 5.10: (a) Multi-layered structures formed by two deposition cycles of TPA and TAPT molecules. Hybrid structures are formed on top of the **[$Mg_1(TPA)_3(TAPT)_2$]** network. The zoom-in of the surface shows two hybrid structures based in six TAPT molecules surrounding (b) one and (c) two TPA molecules, respectively. (d) Induced temperature-desorption curve that shows the CO_2 (mass 44) desorption at 400 K. The red curve corresponds to the heating up of the sample.

The structural analysis of both structures referred as "**Hybrid network 1"** (**Figure 5.10(b)**) and "**Hybrid network 2"** (**Figure 5.10(c)**) reveals a recurring motif of six TAPT molecules surrounding one and two TPA molecules, respectively. The proposed models are depicted at the bottom right side of each image and suggest that the TAPT molecules on the topmost layer have their NH_2 groups' semi-deprotonated (induced by the post annealing processes). If the TAPT molecules would remain intact, the lack of acceptor units would prevent any sort of interaction. The TAPT

molecules are coordinated by H-bonds between the N (semi-deprotonated NH_2) and the H from the phenyl ring of each TAPT molecule (N···H-C), which arranges them in pairs towards a structure with hexagonal geometry [168]. In addition, the circular features inside the hexagons would correspond to fully-deprotonated TPA molecules, which form multiple H-bonds with the TAPT molecules to contribute in the stability of the hexagonal shape motif. Since the molecules deposited on top of the first layer cannot sequestrate adatoms from the bare substrate, then it is proposed that the interaction of these structures is only through H-bonds.

As seen in MOFs, a structure with high amount of material may enhance the capture of gases [53], [54]. Therefore, the sample was exposed to a third deposition cycle and then, the 3D structures were exposed to 760 L of CO_2. Following, the sample was heated-up to induce the CO_2 desorption with temperature and the desorbed species were tracked by a mass quadrupole. The curve shown in **Figure 5.10(d)** shows that the complete desorption of CO_2 occurs at around 400 K (red curve). This indicates that the formation of multi-layers of TAPT and TPA holds the promise to act as reservoirs for molecules, and to work as model systems for gas storage such as CO_2 [178].

5.6. Conclusions

The co-deposition of TAPT and TPA molecules either on atomically clean surfaces of Cu(100) or Mg(0001) at RT formed highly-ordered supramolecular hetero-structures. The balance in the quantity of the TPA and TAPT molecules plays a key role in the formation of the hetero-structures. Hence, a TPA:TAPT molecular ratio lower than 1 let the TAPT molecules free to sequestrate and coordinate the adatoms of the host substrate. On the other hand, a TPA:TAPT molecular ratio higher or equal to 1 enhances the formation of H-bonds between the molecules.

The deposition order of the molecules influences the formation of the hetero-molecular structures on Cu(100). Thus, the sequential deposition of TPA and TAPT allows the fully-deprotonation of TPA to form a homo-molecular network. Therefore, when TAPT is introduced on the system, the COO^- groups present an affinity to the NH_2 groups of TAPT, which prevents their deprotonation. This shows that the N-H···O are stronger than the C-O···H interactions (N-H···O > C-O···H). Once in the structure, if a TAPT molecule semi-deprotonates, a TPA molecule is replaced by the incorporation of Cu adatoms, which do not lead to the collapse of the structure. In addition, the structure presents pores which act as trapping sites for Cu adatoms. This shows that these structures can incorporate or trap metal adatoms, which could act as active sites. Nevertheless, the further incorporation of Mg does not induce the formation of an ordered structure because Mg competes with the Cu adatoms from the host substrate.

On Mg(0001), the co-deposition of TPA and TAPT formed a metallic-hetero-organic network with a Mg^{2+} center from the substrate. The post-annealing treatment ensured the semi-deprotonation and fully-deprotonation of the TAPT and TPA molecules, respectively. The structure was stabilized by H-bonds between the COO^- and NH groups of TPA and TAPT molecules, respectively. In this case, the lower reactivity of the substrate enhanced the N-H···O bonds (TAPT-TPA) rather than the metal-organic Mg-N-H coordination (TAPT-Mg). CO_2 induced

the partial restructuration of the structure, thus giving evidence that CO_2 could form carbamate species whose COO^- group interacts electrostatically with the Mg^{2+} center from the pore. This configuration gave hints in resembling the structure and the catalytic function (for the CO_2 absorption) of the active site of RuBisCO. On the other hand, this network showed promising features as a passivating layer against oxidation as there were no structural evidences of O_2 adsorption. Finally, this structure showed the ability to incorporate TPA and TAPT molecules in multilayers to form a 3D structure, which could store (adsorb and desorb reversibly) CO_2.

In this chapter we demonstrate that porous structures can accommodate organic molecules (such as TPA) or can act as trapping sites for metal adatoms which in fact can work as active sites for gas adsorption and storage, encouraging their use for hetero-catalysis.

Chapter 6: Summary and Outlook

This thesis took inspiration in the structure and catalytic function of RuBisCO to design 2D supramolecular structures and study their reactivity towards CO_2 and O_2. The building blocks included Mg adatoms, a molecule with COOH functional groups (TPA) and a molecule with NH_2 functional groups (TAPT). The Mg adatoms were used to mimic the metal center of the metallo-enzyme, as an active site for gas adsorption (CO_2 and O_2). The TAPT (as analog of the lysine molecule) and TPA molecules were chosen to mimic the amine and carboxylate environments of the active site, respectively (**Figure 6.1**). These components self-assembled on metallic substrates of Cu(100) and Mg(0001).

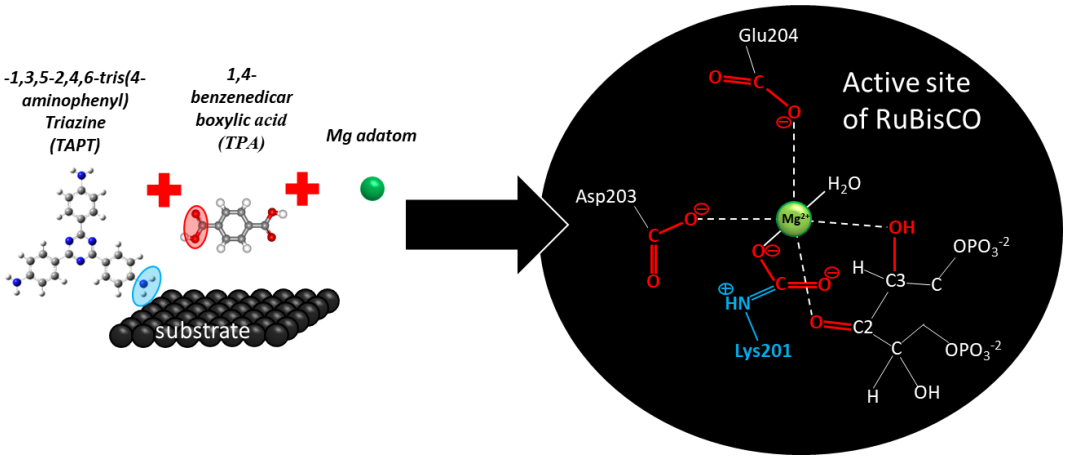

Figure 6.1: The rational design of the 2D supramolecular structures took inspiration in the active site of RuBisCO. Mg adatoms were used to mimic the metal center (in green), a TAPT molecule (amine functional groups in blue) was used as analog of the lysine molecule and a TPA molecule (carboxylate functional groups in red) was used to mimic the carboxylate environment of the active site. The adsorbates were deposited on a metallic substrate hold at RT.

The first part of this thesis studied the self-assembly properties of TAPT molecules. It was found that the NH_2 groups semi-deprotonate to allow the formation of MONs with adatoms from the host substrates. According to the nature of the substrate, MONs with different structural motifs are formed. In fact, the high reactivity of Cu(100) allowed the formation of directional 1D chain-like structures, while the low reactivity of Mg(0001) enhanced the interactions between the adsorbates to form compact 2D metal-organic structures. On the other hand, the COOH groups of TPA fully-deprotonate on both substrates, allowing the formation of homo-molecular networks.

Accordingly, the homo-molecular phase of TPA was used as a precursor to form more complex supramolecular systems. Thus, upon deposition of TAPT molecules on the TPA layer on Cu(100), the COO^- groups bind to the upcoming NH_2 groups to avoid their interaction with the surface, resulting in highly-ordered supramolecular hetero-molecular structures. In contrast, on Mg(0001), a thermal treatment induced the fully- and semi-deprotonation of the co-deposited TPA and TAPT molecules, respectively. The low reactivity of the substrate enhanced the H-bonding between the COO^- and NH groups that resulted in a porous metal-hetero-molecular structure. The highly electronegative environment of the pores allows trapping inside Mg adatoms in its cationic state: Mg^{2+}.

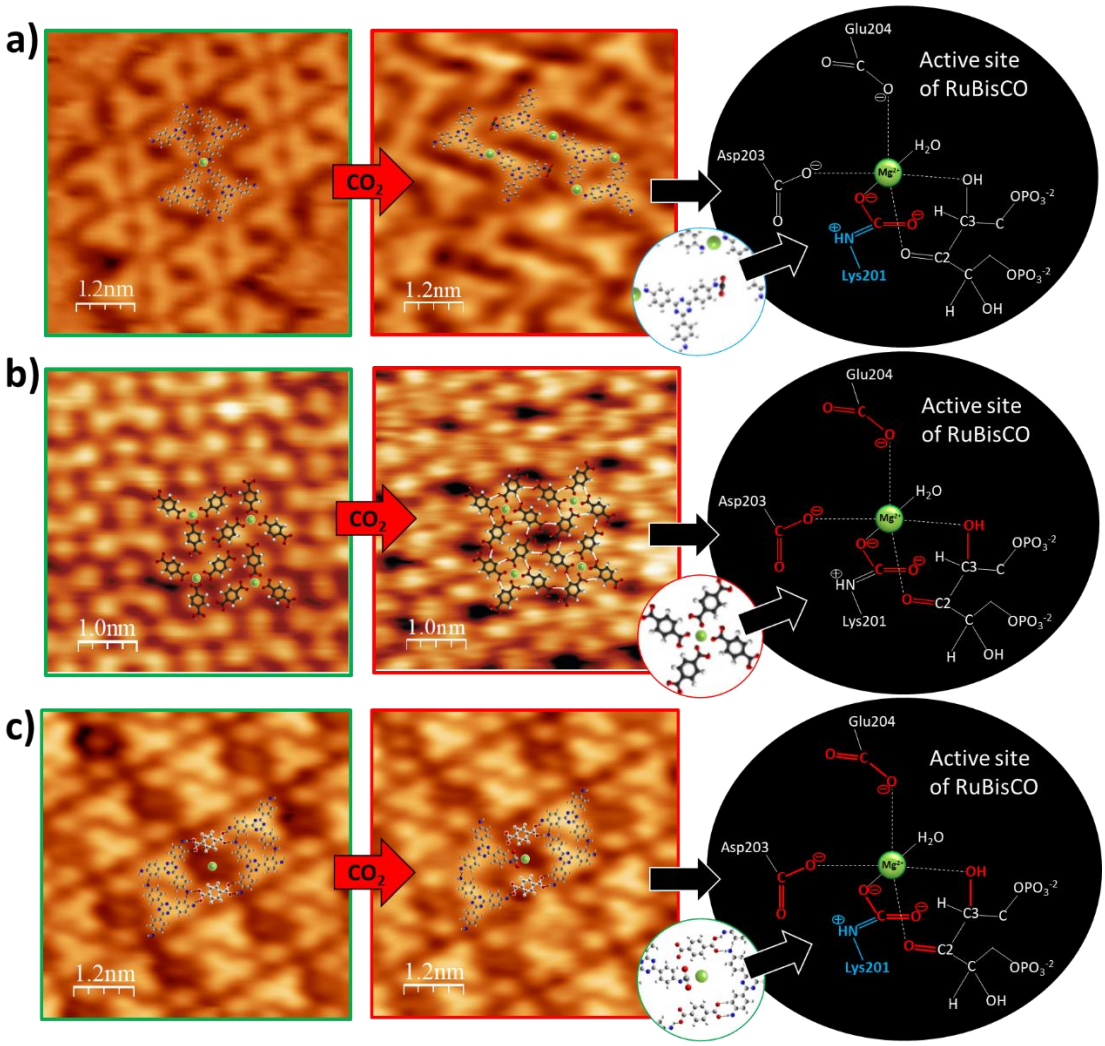

Figure 6.2: The Mg-based 2D supramolecular structures showed structural evidences of CO_2 adsorption and resembled partially the active site of RuBisCO. (a) The TAPT-Mg networks reacted with CO_2 to form carbamates as analogs of the carbamate of lysine in RuBiSCO. (b) The Mg-3TPA networks reacted with CO_2 and resembled the carboxylate environment around the Mg^{2+} center in RuBiSCO. (c) The $Mg_1(TPA)_2(TAPT)_2$ networks reacted with CO_2 and resembled the amine and carboxylate environments around the Mg^{2+} center in RuBiSCO.

The introduction of Mg adatoms in the structure of the MONs with Cu centers on Cu(100) failed, due to the competition between the Cu and Mg adatoms that prevents the formation of well-ordered networks. Mg adatoms showed a preference for the COO^- groups, while the NH_2 groups showed more affinity for the Cu adatoms. Indeed, upon deposition of Mg adatoms on a homo-molecular TPA layer on Cu(100), the COO^- groups bound electrostatically to the Mg^{2+} cations (Mg-3TPA ionic networks). The metal-organic structures with Mg centers showed structural and chemical evidences of gas adsorption on the Mg^{2+} centers at RT, thus resembling the active site of RuBisCO. In the presence of an amino environment (Mg-TAPT networks), the Mg atoms induced the interaction of CO_2 with the semi-deprotonated NH_2 group of TAPT to form carbamates (**Figure 6.2(a)**). In the presence of a carboxylate environment (Mg-3TPA networks), the Mg^{2+} centers acted as adsorption sites for CO_2 (as well as for O_2) (**Figure 6.2(b)**). Remarkably, the introduction of CO_2 in the metal-hetero-organic networks $[Mg_1(TPA)_2(TAPT)_2]$, formed carbamates that interacted electrostatically with the Mg^{2+} centers, thus resembling the carboxylate and amino environments in the active site of RuBisCO (**Figure 6.2(c)**). Interestingly, the Mg^{2+} cations, trapped inside the highly electronegative pores, also acted as active sites for TPA adsorption that further promoted the formation of 3D structures.

Mimicking the catalytic function of RuBisCO involves the transfer of an absorbed CO_2 molecule into C_n-organic molecules. As it was seen in **Figure 1.1**, the carboxylation reaction performed by the RuBisCO enzyme begins with the abstraction of a H^+ from the C3 site in the RuBP attached to the Mg^{2+} center. This abstraction triggers the electrons rearrangement process in RuBP that is stabilized by the Mg^{2+} center, and finishes with the incorporation of CO_2. A recent work has shown the fixation and transfer of CO_2 into ketones (RC(=O)R') that were previously charged with electrons photo-generated by silicon nanowires [179]. In this regard, 1-Phenylethan-1-one (Acetophenone, $C_6H_5C(=O)CH_3$) is a simple aromatic ketone that can be used as a 2D analog of RuBP for CO_2 transfer [12] (**Figure 6.3(a)**). Unlike sugar molecules, the model C-H acid acetophenone molecule can be tested in UHV conditions. Hence, it is intriguing to study the performance of the MONs incorporating CO_2 into the acetophenone. The deprotonation of this molecule once it is adsorbed in the 2D structures may trigger the road towards CO_2 fixation.

Thus, the self-assembly properties of 200 L of acetophenone deposited on an atomically clean surface of Mg(0001) at RT, was studied. The STM image in **Figure 6.3(b)** showed circular motifs scattered along the surface, whose diameter (~0.6 Å) fits well with the molecular length of a single acetophenone molecule (inset image). A new process to increase the molecular coverage should be implemented to enhance the molecular interactions. The next step consisted in the deposition of acetophenone on a typical **$[Mg_1(TPA)_2(TAPT)_2]$** network. The STM image in **Figure 6.3(c)** does not show any structural change in the structure. Nevertheless, spherical features are spotted within the pores (highlighted by the purple circles), whose diameter of ~0.6 Å agrees with the diameter of the acetophenone molecule. This suggests that the acetophenone molecules adsorb on the Mg^{2+} centers, which are trapped inside the pores. The incorporation of acetophenone in the **$[Mg_1(TPA)_2(TAPT)_2]$** network gives initial evidence to pursue the transfer of the C atoms from a CO_2 molecule into organic molecules [180]. Thus, the process was followed by the introduction of 650 L of CO_2 to study its reactivity with the acetophenone molecules contained on the **$[Mg_1(TPA)_2(TAPT)_2]$** structure. However, the analysis by STM did not reveal any

structural change, nor any additional feature in the network that could be taken as prove that new C_n-organic species were formed (images not shown here). In this regard, the Mg^{2+} centers of the Mg-3TPA ionic networks presented in **Chapter 4**, are also promising in terms of molecular adsorption. This encourages their use to study the catalytic transfer of the carbon from CO_2 into organic molecules. The analysis of such complex systems might be limited is not straightforward by a simple STM observation. Therefore, the use of a complementary techniques such as HR-XPS could give insights in the formation of new chemical species and the chemistry of the reactions as the binding energies peaks for acetophenone have been identified in previous studies [181]. In addition, as seen in **Figure 5.10(d**) and in experiments for CO_2 adsorption in MONs [65]**,** Thermal Program Desorption (TPD), might also be included in future experiments to detect the desorption of the C_n-organic molecules formed.

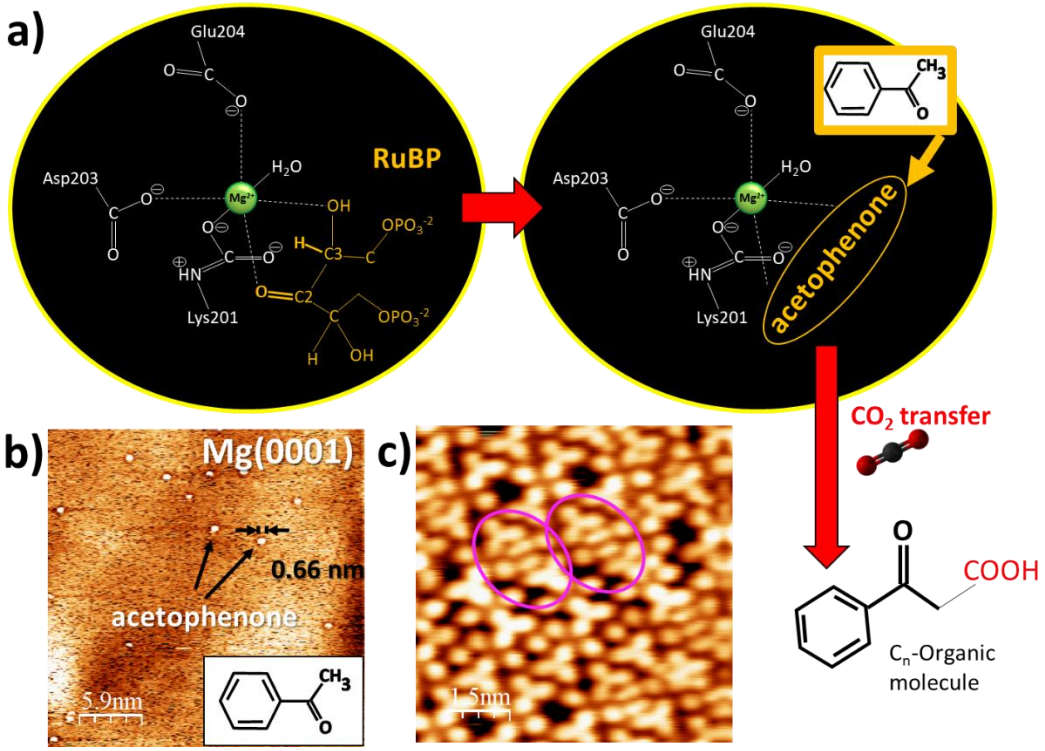

Figure 6.3: (a) Scheme that proposes the replacement of RuBP (highlighted in yellow) by an acetophenone molecule. The introduction of a CO_2 molecule may carboxylate the acetophenone to form eventually a C_n-organic molecule. (b) Bright spots representing acetophenone molecules deposited on a Mg(0001) surface. The inset shows the chemical structure of the acetophenone molecule. (c) STM image of the structure **$[Mg_1(TPA)_2(TAPT)_2]$** with additional spherical features inside the pores (highlighted by the purple circles) which may be related to acetophenone molecules adsorbed on the Mg^{2+} sites.

Conclusions

This thesis presented the combination of two approaches: biomimetics and 2D self-assembly. The rational design of the first Mg-based 2D supramolecular networks was bioinspired in the structure and the catalytic function of the active site of RuBisCO. The structural conformation of the self-assemblies could be tuned, by the cooperative or sole interaction of molecules bearing carboxylate- or amine functionalities with metal adatoms of Cu or Mg. The functional structures could mimic, with a certain degree of accuracy, the structure and the catalytic function of the active site of RuBisCO for CO_2 and O_2 adsorption. Thus, it was shown that it is possible to reverse the structure-function equation, i.e. inspired in the functionality of the active site we build a new structure molecule by molecule. These findings encourage the exploration and design of 2D nano-catalyst as analogues of the metallo-enzymes found in nature.

References

[1] G. Mul, C. Schacht, W. P. M. van Swaaij, and J. A. Moulijn, "Functioning devices for solar to fuel conversion," *Chem. Eng. Process. Process Intensif.*, vol. 51, pp. 137–149, Jan. 2012.

[2] J. M. Berg, J. L. Tymoczko, and L. Stryer, "Section 20.1: The Calvin Cycle Synthesizes Hexoses from Carbon Dioxide and Water," in *Biochemistry*, 5th edition., New York: W H Freeman, 2002.

[3] T. C. Taylor and I. Andersson, "The structure of the complex between rubisco and its natural substrate ribulose 1,5-bisphosphate," *J. Mol. Biol.*, vol. 265, no. 4, pp. 432–444, Jan. 1997.

[4] J. Newman, C. I. Branden, and T. A. Jones, "Structure determination and refinement of ribulose 1,5-bisphosphate carboxylase/oxygenase from Synechococcus PCC6301," *Acta Crystallogr. D Biol. Crystallogr.*, vol. 49, no. Pt 6, pp. 548–560, Nov. 1993.

[5] M. H. Sazinsky and S. J. Lippard, "Product Bound Structures of the Soluble Methane Monooxygenase Hydroxylase from Methylococcus capsulatus (Bath): Protein Motion in the α-Subunit," *J. Am. Chem. Soc.*, vol. 127, no. 16, pp. 5814–5825, Apr. 2005.

[6] S. Prabhulkar, H. Tian, X. Wang, J.-J. Zhu, and C.-Z. Li, "Engineered Proteins: Redox Properties and Their Applications," *Antioxid. Redox Signal.*, vol. 17, no. 12, pp. 1796–1822, Mar. 2012.

[7] J. Liu *et al.*, "Metalloproteins Containing Cytochrome, Iron–Sulfur, or Copper Redox Centers," *Chem. Rev.*, vol. 114, no. 8, pp. 4366–4469, Apr. 2014.

[8] M. Yan, Y. Lu, Y. Gao, M. F. Benedetti, and G. V. Korshin, "In-Situ Investigation of Interactions between Magnesium Ion and Natural Organic Matter," *Environ. Sci. Technol.*, vol. 49, no. 14, pp. 8323–8329, Jul. 2015.

[9] T. J. Andrews, "The bait in the Rubisco mousetrap," *Nat. Struct. Mol. Biol.*, vol. 3, no. 1, pp. 3–7, Jan. 1996.

[10] B. Stec, "Structural mechanism of RuBisCO activation by carbamylation of the active site lysine," *Proc. Natl. Acad. Sci. U. S. A.*, vol. 109, no. 46, pp. 18785–18790, Nov. 2012.

[11] H. Mauser, W. A. King, J. E. Gready, and T. J. Andrews, "CO2 Fixation by Rubisco: Computational Dissection of the Key Steps of Carboxylation, Hydration, and C−C Bond Cleavage," *J. Am. Chem. Soc.*, vol. 123, no. 44, pp. 10821–10829, Nov. 2001.

[12] D. Walther, M. Ruben, and S. Rau, "Carbon dioxide and metal centres: from reactions inspired by nature to reactions in compressed carbon dioxide as solvent," *Coord. Chem. Rev.*, vol. 182, no. 1, pp. 67–100, Feb. 1999.

[13] J. V. Barth, G. Costantini, and K. Kern, "Engineering atomic and molecular nanostructures at surfaces," *Nature*, vol. 437, no. 7059, pp. 671–679, Sep. 2005.

[14] J. V. Barth, "Fresh perspectives for surface coordination chemistry," *Surf. Sci.*, vol. 603, no. 10–12, pp. 1533–1541, Jun. 2009.

[15] R. Gutzler, S. Stepanow, D. Grumelli, M. Lingenfelder, and K. Kern, “Mimicking Enzymatic Active Sites on Surfaces for Energy Conversion Chemistry,” *Acc. Chem. Res.*, vol. 48, no. 7, pp. 2132–2139, Jul. 2015.
[16] S. L. Tait *et al.*, “Assembling Isostructural Metal-Organic Coordination Architectures on Cu(100), Ag(100) and Ag(111) Substrates,” *ChemPhysChem*, vol. 9, no. 17, pp. 2495–2499, Dec. 2008.
[17] T. R. Umbach *et al.*, “Site-specific bonding of copper adatoms to pyridine end groups mediating the formation of two-dimensional coordination networks on metal surfaces,” *Phys. Rev. B*, vol. 89, no. 23, p. 235409, Jun. 2014.
[18] A. Rastgoo-Lahrood *et al.*, “From Au–Thiolate Chains to Thioether Sierpiński Triangles: The Versatile Surface Chemistry of 1,3,5-Tris(4-mercaptophenyl)benzene on Au(111),” *ACS Nano*, vol. 10, no. 12, pp. 10901–10911, Dec. 2016.
[19] A. Dmitriev, H. Spillmann, N. Lin, J. V. Barth, and K. Kern, “Modular Assembly of Two-Dimensional Metal–Organic Coordination Networks at a Metal Surface,” *Angew. Chem. Int. Ed.*, vol. 42, no. 23, pp. 2670–2673, Jun. 2003.
[20] J. V. Barth, “Molecular architectonic on metal surfaces,” *Annu. Rev. Phys. Chem.*, vol. 58, pp. 375–407, 2007.
[21] J. V. Barth, J. Weckesser, N. Lin, A. Dmitriev, and K. Kern, “Supramolecular architectures and nanostructures at metal surfaces,” *Appl. Phys. A*, vol. 76, no. 5, pp. 645–652, Mar. 2003.
[22] L. Dong, Z. Gao, and N. Lin, “Self-assembly of metal–organic coordination structures on surfaces,” *Prog. Surf. Sci.*, vol. 91, no. 3, pp. 101–135, Aug. 2016.
[23] S. Stepanow *et al.*, “Rational Design of Two-Dimensional Nanoscale Networks by Electrostatic Interactions at Surfaces,” *ACS Nano*, vol. 4, no. 4, pp. 1813–1820, Apr. 2010.
[24] D. Skomski, S. Abb, and S. L. Tait, “Robust Surface Nano-Architecture by Alkali–Carboxylate Ionic Bonding,” *J. Am. Chem. Soc.*, vol. 134, no. 34, pp. 14165–14171, Aug. 2012.
[25] N. Abdurakhmanova *et al.*, “Stereoselectivity and electrostatics in charge-transfer Mn- and Cs-TCNQ4 networks on Ag(100),” *Nat. Commun.*, vol. 3, p. 940, Jul. 2012.
[26] T. R. Umbach *et al.*, “Atypical charge redistribution over a charge-transfer monolayer on a metal,” *New J. Phys.*, vol. 15, no. 8, p. 083048, 2013.
[27] W. Xu *et al.*, “Atomic-scale structures and interactions between the guanine quartet and potassium,” *Chem. Commun.*, vol. 49, no. 65, pp. 7210–7212, Jul. 2013.
[28] D. Skomski and S. L. Tait, “Ordered and Robust Ionic Surface Networks from Weakly Interacting Carboxyl Building Blocks,” *J. Phys. Chem. C*, vol. 117, no. 6, pp. 2959–2965, Feb. 2013.
[29] M. A. Lingenfelder *et al.*, “Towards Surface-Supported Supramolecular Architectures: Tailored Coordination Assembly of 1,4-Benzenedicarboxylate and Fe on Cu(100),” *Chem. – Eur. J.*, vol. 10, no. 8, pp. 1913–1919, Apr. 2004.
[30] S. L. Tait *et al.*, “Metal−Organic Coordination Interactions in Fe−Terephthalic Acid Networks on Cu(100),” *J. Am. Chem. Soc.*, vol. 130, no. 6, pp. 2108–2113, Feb. 2008.
[31] S. Pan *et al.*, “Design and control of electron transport properties of single molecules,” *Proc. Natl. Acad. Sci.*, vol. 106, no. 36, pp. 15259–15263, Sep. 2009.

[32] L. Wang, P. Li, H. Shi, Z. Li, K. Wu, and X. Shao, “Thickness-Dependent Adsorption of Melamine on Cu/Au(111) Films,” *J. Phys. Chem. C*, vol. 121, no. 14, pp. 7977–7984, Apr. 2017.
[33] T. Sirtl *et al.*, “Control of Intermolecular Bonds by Deposition Rates at Room Temperature: Hydrogen Bonds versus Metal Coordination in Trinitrile Monolayers,” *J. Am. Chem. Soc.*, vol. 135, no. 2, pp. 691–695, Jan. 2013.
[34] G. Pawin *et al.*, “A Surface Coordination Network Based on Substrate-Derived Metal Adatoms with Local Charge Excess,” *Angew. Chem. Int. Ed.*, vol. 47, no. 44, pp. 8442–8445, Oct. 2008.
[35] U. Schlickum *et al.*, “Metal−Organic Honeycomb Nanomeshes with Tunable Cavity Size,” *Nano Lett.*, vol. 7, no. 12, pp. 3813–3817, Dec. 2007.
[36] S. Stepanow *et al.*, “Surface-Assisted Assembly of 2D Metal–Organic Networks That Exhibit Unusual Threefold Coordination Symmetry,” *Angew. Chem. Int. Ed.*, vol. 46, no. 5, pp. 710–713, Jan. 2007.
[37] H. Walch *et al.*, “Extended Two-Dimensional Metal–Organic Frameworks Based on Thiolate–Copper Coordination Bonds,” *J. Am. Chem. Soc.*, vol. 133, no. 20, pp. 7909–7915, May 2011.
[38] J. He, C. Yang, Z. Xu, M. Zeller, A. D. Hunter, and J. Lin, “Building thiol and metal-thiolate functions into coordination nets: Clues from a simple molecule,” *J. Solid State Chem.*, vol. 182, no. 7, pp. 1821–1826, Jul. 2009.
[39] T. R. Umbach *et al.*, “Ferromagnetic Coupling of Mononuclear Fe Centers in a Self-Assembled Metal-Organic Network on Au(111),” *Phys. Rev. Lett.*, vol. 109, no. 26, p. 267207, Dec. 2012.
[40] J. A. Theobald, N. S. Oxtoby, M. A. Phillips, N. R. Champness, and P. H. Beton, “Controlling molecular deposition and layer structure with supramolecular surface assemblies,” *Nature*, vol. 424, no. 6952, pp. 1029–1031, Aug. 2003.
[41] S. Stepanow *et al.*, “Steering molecular organization and host–guest interactions using two-dimensional nanoporous coordination systems,” *Nat. Mater.*, vol. 3, no. 4, pp. 229–233, Apr. 2004.
[42] L. Bartels, “Tailoring molecular layers at metal surfaces,” *Nat. Chem.*, vol. 2, no. 2, pp. 87–95, Feb. 2010.
[43] L. Wang *et al.*, “Metal adatoms generated by the co-play of melamine assembly and subsequent CO adsorption,” *Phys. Chem. Chem. Phys.*, vol. 18, no. 4, pp. 2324–2329, Jan. 2016.
[44] J. Čechal *et al.*, “Functionalization of Open Two-Dimensional Metal–Organic Templates through the Selective Incorporation of Metal Atoms,” *J. Phys. Chem. C*, vol. 117, no. 17, pp. 8871–8877, May 2013.
[45] R. Decker *et al.*, “Using metal-organic templates to steer the growth of Fe and Co nanoclusters,” *Appl. Phys. Lett.*, vol. 93, no. 24, p. 243102, Dec. 2008.
[46] J. W. Akitt, “Some observations on the greenhouse effect at the Earth’s surface,” *Spectrochim. Acta. A. Mol. Biomol. Spectrosc.*, vol. 188, no. Supplement C, pp. 127–134, Jan. 2018.
[47] S. Chu and A. Majumdar, “Opportunities and challenges for a sustainable energy future,” *Nature*, vol. 488, no. 7411, pp. 294–303, Aug. 2012.
[48] Q. Liu, L. Wu, R. Jackstell, and M. Beller, “Using carbon dioxide as a building block in organic synthesis,” *Nat. Commun.*, vol. 6, p. 5933, Jan. 2015.

[49] A. Loiudice *et al.*, “Tailoring Copper Nanocrystals towards C2 Products in Electrochemical CO2 Reduction,” *Angew. Chem. Int. Ed.*, vol. 55, no. 19, pp. 5789–5792, May 2016.
[50] S. Hadenfeldt, C. Benndorf, A. Stricker, and M. Töwe, “Adsorption of CO2 on K-promoted Cu(111) surfaces,” *Surf. Sci.*, vol. 352, pp. 295–299, May 1996.
[51] U. Burghaus, “Surface chemistry of CO2 – Adsorption of carbon dioxide on clean surfaces at ultrahigh vacuum,” *Prog. Surf. Sci.*, vol. 89, no. 2, pp. 161–217, May 2014.
[52] P. R. Davies and J. M. Keel, “The reaction of carbon dioxide with amines at a Cu(211) surface,” *Surf. Sci.*, vol. 469, no. 2–3, pp. 204–213, Dec. 2000.
[53] Z. Guo *et al.*, “Magnesium-Based 3D Metal−Organic Framework Exhibiting Hydrogen-Sorption Hysteresis,” *Inorg. Chem.*, vol. 48, no. 17, pp. 8069–8071, Sep. 2009.
[54] D. Banerjee and J. B. Parise, “Recent Advances in s-Block Metal Carboxylate Networks,” *Cryst. Growth Des.*, vol. 11, no. 10, pp. 4704–4720, Oct. 2011.
[55] Z. Bao *et al.*, “Adsorption of Ethane, Ethylene, Propane, and Propylene on a Magnesium-Based Metal–Organic Framework,” *Langmuir*, vol. 27, no. 22, pp. 13554–13562, Nov. 2011.
[56] P. D. C. Dietzel *et al.*, “Adsorption properties and structure of CO2 adsorbed on open coordination sites of metal–organic framework Ni2(dhtp) from gas adsorption, IR spectroscopy and X-ray diffraction,” *Chem. Commun.*, no. 41, pp. 5125–5127, Oct. 2008.
[57] H. Wu, J. M. Simmons, G. Srinivas, W. Zhou, and T. Yildirim, “Adsorption Sites and Binding Nature of CO2 in Prototypical Metal−Organic Frameworks: A Combined Neutron Diffraction and First-Principles Study,” *J. Phys. Chem. Lett.*, vol. 1, no. 13, pp. 1946–1951, Jul. 2010.
[58] S. Fabris *et al.*, “Oxygen Dissociation by Concerted Action of Di-Iron Centers in Metal–Organic Coordination Networks at Surfaces: Modeling Non-Heme Iron Enzymes,” *Nano Lett.*, vol. 11, no. 12, pp. 5414–5420, Dec. 2011.
[59] D. Grumelli, B. Wurster, S. Stepanow, and K. Kern, “Bio-inspired nanocatalysts for the oxygen reduction reaction,” *Nat. Commun.*, vol. 4, p. 2904, Dec. 2013.
[60] D. Skomski, C. D. Tempas, K. A. Smith, and S. L. Tait, “Redox-Active On-Surface Assembly of Metal–Organic Chains with Single-Site Pt(II),” *J. Am. Chem. Soc.*, vol. 136, no. 28, pp. 9862–9865, Jul. 2014.
[61] M. Costas, M. P. Mehn, M. P. Jensen, and L. Que, “Dioxygen Activation at Mononuclear Nonheme Iron Active Sites: Enzymes, Models, and Intermediates,” *Chem. Rev.*, vol. 104, no. 2, pp. 939–986, Feb. 2004.
[62] E. I. Solomon *et al.*, “Geometric and Electronic Structure/Function Correlations in Non-Heme Iron Enzymes,” *Chem. Rev.*, vol. 100, no. 1, pp. 235–350, Jan. 2000.
[63] F. Rosati and G. Roelfes, “Artificial Metalloenzymes,” *ChemCatChem*, vol. 2, no. 8, pp. 916–927, Aug. 2010.
[64] M. J. Wiester, P. A. Ulmann, and C. A. Mirkin, “Enzyme Mimics Based Upon Supramolecular Coordination Chemistry,” *Angew. Chem. Int. Ed.*, vol. 50, no. 1, pp. 114–137, Jan. 2011.
[65] J. Čechal *et al.*, “CO2 Binding and Induced Structural Collapse of a Surface-Supported Metal–Organic Network,” *J. Phys. Chem. C*, vol. 120, no. 33, pp. 18622–18630, Aug. 2016.

[66] J. A. A. W. Elemans, S. Lei, and S. De Feyter, “Molecular and Supramolecular Networks on Surfaces: From Two-Dimensional Crystal Engineering to Reactivity,” *Angew. Chem. Int. Ed.*, vol. 48, no. 40, pp. 7298–7332, Sep. 2009.
[67] C. R. Ast *et al.*, “Sensing the quantum limit in scanning tunnelling spectroscopy,” *Nat. Commun.*, vol. 7, p. ncomms13009, Oct. 2016.
[68] F. Klappenberger, “Two-dimensional functional molecular nanoarchitectures – Complementary investigations with scanning tunneling microscopy and X-ray spectroscopy,” *Prog. Surf. Sci.*, vol. 89, no. 1, pp. 1–55, Feb. 2014.
[69] J. Bardeen, “Tunnelling from a Many-Particle Point of View,” *Phys. Rev. Lett.*, vol. 6, no. 2, pp. 57–59, Jan. 1961.
[70] A. U. Goonewardene, J. Karunamuni, R. L. Kurtz, and R. L. Stockbauer, “An STM study of the oxidation of Mg(0 0 0 1),” *Surf. Sci.*, vol. 501, no. 1–2, pp. 102–111, Mar. 2002.
[71] A. F. Carley, P. R. Davies, K. R. Harikumar, R. V. Jones, and M. W. Roberts, “Oxygen States at Magnesium and Copper Surfaces Revealed by Scanning Tunneling Microscopy and Surface Reactivity,” *Top. Catal.*, vol. 24, no. 1–4, pp. 51–59, Oct. 2003.
[72] W. S. Vogan, R. L. Champion, and V. A. Esaulov, “The role of an oxygen adsorbate on the secondary emission properties of low energy ion-bombarded magnesium,” *Surf. Sci.*, vol. 538, no. 3, pp. 211–218, Jul. 2003.
[73] J. B. Abreu, J. Sanabria-Chinchilla, K. D. Cummins, J. L. Stickney, and M. P. Soriaga, “The structure, composition and reactivity of clean and ambient-exposed polycrystalline and monocrystalline Mg surfaces,” *J. Electroanal. Chem.*, vol. 662, no. 1, pp. 36–42, Nov. 2011.
[74] G. Kresse and J. Hafner, “Ab initio,” *Phys. Rev. B*, vol. 47, no. 1, pp. 558–561, Jan. 1993.
[75] G. Kresse and J. Furthmüller, “Efficient iterative schemes for ab initio total-energy calculations using a plane-wave basis set,” *Phys. Rev. B*, vol. 54, no. 16, pp. 11169–11186, Oct. 1996.
[76] M. Dion, H. Rydberg, E. Schröder, D. C. Langreth, and B. I. Lundqvist, “Van der Waals Density Functional for General Geometries,” *Phys. Rev. Lett.*, vol. 92, no. 24, p. 246401, Jun. 2004.
[77] S. Jensen and C. J. Baddeley, “Formation of PTCDI-Based Metal Organic Structures on a Au(111) Surface Modified by 2-D Ni Clusters,” *J. Phys. Chem. C*, vol. 112, no. 39, pp. 15439–15448, Oct. 2008.
[78] F. Silly *et al.*, “Melamine Structures on the Au(111) Surface,” *J. Phys. Chem. C*, vol. 112, no. 30, pp. 11476–11480, Jul. 2008.
[79] Z. Shi, J. Liu, T. Lin, F. Xia, P. N. Liu, and N. Lin, “Thermodynamics and Selectivity of Two-Dimensional Metallo-supramolecular Self-Assembly Resolved at Molecular Scale,” *J. Am. Chem. Soc.*, vol. 133, no. 16, pp. 6150–6153, Apr. 2011.
[80] J. Liu *et al.*, “Structural Transformation of Two-Dimensional Metal–Organic Coordination Networks Driven by Intrinsic In-Plane Compression,” *J. Am. Chem. Soc.*, vol. 133, no. 46, pp. 18760–18766, Nov. 2011.
[81] T. Classen *et al.*, “Hydrogen and Coordination Bonding Supramolecular Structures of Trimesic Acid on Cu(110),” *J. Phys. Chem. A*, vol. 111, no. 49, pp. 12589–12603, Dec. 2007.

[82] T. Classen *et al.*, “Templated Growth of Metal–Organic Coordination Chains at Surfaces,” *Angew. Chem. Int. Ed.*, vol. 44, no. 38, pp. 6142–6145, Sep. 2005.
[83] N. Lin, A. Dmitriev, J. Weckesser, J. V. Barth, and K. Kern, “Real-Time Single-Molecule Imaging of the Formation and Dynamics of Coordination Compounds,” *Angew. Chem. Int. Ed.*, vol. 41, no. 24, pp. 4779–4783, Dec. 2002.
[84] A. Langner, S. L. Tait, N. Lin, R. Chandrasekar, M. Ruben, and K. Kern, “Ordering and Stabilization of Metal–Organic Coordination Chains by Hierarchical Assembly through Hydrogen Bonding at a Surface,” *Angew. Chem. Int. Ed.*, vol. 47, no. 46, pp. 8835–8838, Nov. 2008.
[85] S. L. Tait *et al.*, “One-Dimensional Self-Assembled Molecular Chains on Cu(100): Interplay between Surface-Assisted Coordination Chemistry and Substrate Commensurability,” *J. Phys. Chem. C*, vol. 111, no. 29, pp. 10982–10987, Jul. 2007.
[86] V. S. Vyas *et al.*, “A tunable azine covalent organic framework platform for visible light-induced hydrogen generation,” *Nat. Commun.*, vol. 6, p. ncomms9508, Sep. 2015.
[87] R. Gomes, P. Bhanja, and A. Bhaumik, “A triazine-based covalent organic polymer for efficient CO2 adsorption,” *Chem. Commun.*, vol. 51, no. 49, pp. 10050–10053, Jun. 2015.
[88] R. Gomes and A. Bhaumik, “A new triazine functionalized luminescent covalent organic framework for nitroaromatic sensing and CO2 storage,” *RSC Adv.*, vol. 6, no. 33, pp. 28047–28054, Mar. 2016.
[89] M. R. Liebl and J. Senker, “Microporous Functionalized Triazine-Based Polyimides with High CO2 Capture Capacity,” *Chem. Mater.*, vol. 25, no. 6, pp. 970–980, Mar. 2013.
[90] M. Treier, N. V. Richardson, and R. Fasel, “Fabrication of Surface-Supported Low-Dimensional Polyimide Networks,” *J. Am. Chem. Soc.*, vol. 130, no. 43, pp. 14054–14055, Oct. 2008.
[91] M. Treier, M.-T. Nguyen, N. V. Richardson, C. Pignedoli, D. Passerone, and R. Fasel, “Tailoring Low-Dimensional Organic Semiconductor Nanostructures,” *Nano Lett.*, vol. 9, no. 1, pp. 126–131, Jan. 2009.
[92] M. Böhringer, K. Morgenstern, W.-D. Schneider, M. Wühn, C. Wöll, and R. Berndt, “Self-assembly of 1-nitronaphthalene on Au(111),” *Surf. Sci.*, vol. 444, no. 1–3, pp. 199–210, Jan. 2000.
[93] S. Lukas, G. Witte, and C. Wöll, “Novel Mechanism for Molecular Self-Assembly on Metal Substrates: Unidirectional Rows of Pentacene on Cu(110) Produced by a Substrate-Mediated Repulsion,” *Phys. Rev. Lett.*, vol. 88, no. 2, p. 028301, Dec. 2001.
[94] P. Ruffieux *et al.*, “Self-Assembly of Extended Polycyclic Aromatic Hydrocarbons on Cu(111),” *J. Phys. Chem. B*, vol. 110, no. 23, pp. 11253–11258, Jun. 2006.
[95] B. Xu, C. Tao, E. D. Williams, and J. E. Reutt-Robey, “Coverage Dependent Supramolecular Structures: C60:ACA Monolayers on Ag(111),” *J. Am. Chem. Soc.*, vol. 128, no. 26, pp. 8493–8499, Jul. 2006.
[96] Y.-P. Lin *et al.*, “Self-Assembled Melamine Monolayer on Cu(111),” *J. Phys. Chem. C*, vol. 117, no. 19, pp. 9895–9902, May 2013.
[97] R. V. Plank, N. J. DiNardo, and J. M. Vohs, “HREELS study of the interaction of aniline with Cu(110),” *Surf. Sci.*, vol. 340, no. 1, pp. L971–L977, Oct. 1995.

[98] J. Björk *et al.*, “STM fingerprint of molecule–adatom interactions in a self-assembled metal–organic surface coordination network on Cu(111),” *Phys. Chem. Chem. Phys.*, vol. 12, no. 31, pp. 8815–8821, 2010.
[99] Y. Wang *et al.*, “Programming Hierarchical Supramolecular Nanostructures by Molecular Design,” *J. Phys. Chem. C*, vol. 117, no. 7, pp. 3440–3445, Feb. 2013.
[100] J. Rodríguez-Fernández *et al.*, “Temperature-controlled metal/ligand stoichiometric ratio in Ag-TCNE coordination networks,” *J. Chem. Phys.*, vol. 142, no. 10, p. 101930, Feb. 2015.
[101] N. Lin *et al.*, “Two-Dimensional Adatom Gas Bestowing Dynamic Heterogeneity on Surfaces,” *Angew. Chem. Int. Ed.*, vol. 44, no. 10, pp. 1488–1491, Feb. 2005.
[102] C. Steiner *et al.*, “Self-Assembly and Stability of Hydrogen-Bonded Networks of Bridged Triphenylamines on Au(111) and Cu(111),” *J. Phys. Chem. C*, vol. 119, no. 46, pp. 25945–25955, Nov. 2015.
[103] B. Wurster, D. Grumelli, D. Hötger, R. Gutzler, and K. Kern, “Driving the Oxygen Evolution Reaction by Nonlinear Cooperativity in Bimetallic Coordination Catalysts,” *J. Am. Chem. Soc.*, vol. 138, no. 11, pp. 3623–3626, Mar. 2016.
[104] M. Šimėnas and E. E. Tornau, “A model of melamine molecules ordering on metal surfaces,” *J. Chem. Phys.*, vol. 141, no. 5, p. 054701, Aug. 2014.
[105] J. Eichhorn, S. Schlögl, B. V. Lotsch, W. Schnick, W. M. Heckl, and M. Lackinger, “Self-assembly of melem on Ag(111)—emergence of porous structures based on amino-heptazine hydrogen bonds,” *CrystEngComm*, vol. 13, no. 18, pp. 5559–5565, Aug. 2011.
[106] M. Furukawa, T. Yamada, S. Katano, M. Kawai, H. Ogasawara, and A. Nilsson, “Geometrical characterization of adenine and guanine on Cu(110) by NEXAFS, XPS, and DFT calculation,” *Surf. Sci.*, vol. 601, no. 23, pp. 5433–5440, Dec. 2007.
[107] F. Klappenberger, A. Weber-Bargioni, W. Auwärter, M. Marschall, A. Schiffrin, and J. V. Barth, “Temperature dependence of conformation, chemical state, and metal-directed assembly of tetrapyridyl-porphyrin on Cu(111),” *J. Chem. Phys.*, vol. 129, no. 21, p. 214702, Dec. 2008.
[108] R. Madueno, M. T. Räisänen, C. Silien, and M. Buck, “Functionalizing hydrogen-bonded surface networks with self-assembled monolayers,” *Nature*, vol. 454, no. 7204, pp. 618–621, Jul. 2008.
[109] D. Feng, Z. Zhou, and M. Bo, “An investigation of the thermal degradation of melamine phosphonite by XPS and thermal analysis techniques,” *Polym. Degrad. Stab.*, vol. 50, no. 1, pp. 65–70, Jan. 1995.
[110] D. Fischer, K. Schwinghammer, C. Sondermann, V. W. Lau, J. Mannhart, and B. V. Lotsch, “Laser ablation of molecular carbon nitride compounds,” *Appl. Surf. Sci.*, vol. 349, no. Supplement C, pp. 353–360, Sep. 2015.
[111] E. Raymundo-Piñero, D. Cazorla-Amorós, A. Linares-Solano, J. Find, U. Wild, and R. Schlögl, “Structural characterization of N-containing activated carbon fibers prepared from a low softening point petroleum pitch and a melamine resin,” *Carbon*, vol. 40, no. 4, pp. 597–608, Apr. 2002.
[112] S. M. Barlow *et al.*, “Polymorphism in supramolecular chiral structures of R- and S-alanine on Cu(1 1 0),” *Surf. Sci.*, vol. 590, no. 2–3, pp. 243–263, Oct. 2005.

[113] D. Costa, C.-M. Pradier, F. Tielens, and L. Savio, “Adsorption and self-assembly of bio-organic molecules at model surfaces: A route towards increased complexity,” *Surf. Sci. Rep.*, vol. 70, no. 4, pp. 449–553, Dec. 2015.
[114] J. Greenwood, H. A. Früchtl, and C. J. Baddeley, “Self-Assembly of Upright, Partially Dehydrogenated Melamine on Pd(111),” *J. Phys. Chem. C*, vol. 117, no. 44, pp. 22874–22879, Nov. 2013.
[115] J. Greenwood, H. A. Früchtl, and C. J. Baddeley, “Ordered Growth of Upright Melamine Species on Ni{111}: A Study with Scanning Tunnelling Microscopy and Reflection Absorption Infrared Spectroscopy,” *J. Phys. Chem. C*, vol. 116, no. 11, pp. 6685–6690, Mar. 2012.
[116] M. R. Ashton, T. S. Jones, N. V. Richardson, R. G. Mack, and W. N. Unertl, “The chemisorption of polyimide precursors and related molecules on metal surfaces,” *J. Electron Spectrosc. Relat. Phenom.*, vol. 54–55, no. Supplement C, pp. 1133–1142, Jan. 1990.
[117] S. X. Huang, D. A. Fischer, and J. L. Gland, “Aniline Adsorption, Hydrogenation, and Hydrogenolysis on the Ni(100) Surface,” *J. Phys. Chem.*, vol. 100, no. 24, pp. 10223–10234, Jan. 1996.
[118] Y. Ge, H. Adler, A. Theertham, L. L. Kesmodel, and S. L. Tait, “Adsorption and Bonding of First Layer and Bilayer Terephthalic Acid on the Cu(100) Surface by High-Resolution Electron Energy Loss Spectroscopy,” *Langmuir*, vol. 26, no. 21, pp. 16325–16329, Nov. 2010.
[119] Y. Wang *et al.*, “Varying molecular interactions by coverage in supramolecular surface chemistry,” *Chem. Commun.*, vol. 48, no. 4, pp. 534–536, Dec. 2011.
[120] C. Wäckerlin, C. Iacovita, D. Chylarecka, P. Fesser, T. A. Jung, and N. Ballav, “Assembly of 2D ionic layers by reaction of alkali halides with the organic electrophile 7,7,8,8-tetracyano-p-quinodimethane (TCNQ),” *Chem. Commun.*, vol. 47, no. 32, pp. 9146–9148, Aug. 2011.
[121] M. Feng, H. Sun, J. Zhao, and H. Petek, “Self-Catalyzed Carbon Dioxide Adsorption by Metal–Organic Chains on Gold Surfaces,” *ACS Nano*, vol. 8, no. 8, pp. 8644–8652, Aug. 2014.
[122] M. Feng *et al.*, “Cooperative Chemisorption-Induced Physisorption of CO2 Molecules by Metal–Organic Chains,” *ACS Nano*, vol. 9, no. 12, pp. 12124–12136, Dec. 2015.
[123] V. Fournier, P. Marcus, and I. Olefjord, “Oxidation of magnesium,” *Surf. Interface Anal.*, vol. 34, no. 1, pp. 494–497, Aug. 2002.
[124] M. Kurth, P. C. J. Graat, and E. J. Mittemeijer, “Determination of the intrinsic bulk and surface plasmon intensity of XPS spectra of magnesium,” *Appl. Surf. Sci.*, vol. 220, no. 1–4, pp. 60–78, Dec. 2003.
[125] J.-W. He, J. S. Corneille, and D. W. Goodman, “An XPS study of Mg overlayers on a Mo(100) surface,” *Appl. Surf. Sci.*, vol. 72, no. 4, pp. 335–340, Dec. 1993.
[126] J. S. Corneille, J.-W. He, and D. W. Goodman, “XPS characterization of ultra-thin MgO films on a Mo(100) surface,” *Surf. Sci.*, vol. 306, no. 3, pp. 269–278, Apr. 1994.
[127] C. Chen, S. J. Splinter, T. Do, and N. S. McIntyre, “Measurement of oxide film growth on Mg and Al surfaces over extended periods using XPS,” *Surf. Sci.*, vol. 382, no. 1, pp. L652–L657, Jun. 1997.
[128] S. J. Splinter, N. S. McIntyre, W. N. Lennard, K. Griffiths, and G. Palumbo, “An AES and XPS study of the initial oxidation of polycrystalline magnesium with

water vapour at room temperature," *Surf. Sci.*, vol. 292, no. 1, pp. 130–144, Jul. 1993.
[129] L. Aballe, A. Barinov, A. Locatelli, T. O. Mentes, and M. Kiskinova, "Initial stages of heteroepitaxial Mg growth on W(110): Early condensation, anisotropic strain, and self-organized patterns," *Phys. Rev. B*, vol. 75, no. 11, p. 115411, Mar. 2007.
[130] H. H. Huang, X. Jiang, H. L. Siew, W. S. Chin, W. S. Sim, and G. Q. Xu, "Oxidation and growth of Mg thin films on Ru(001)," *Surf. Sci.*, vol. 436, no. 1, pp. 167–174, Aug. 1999.
[131] X. D. Peng and M. A. Barteau, "Characterization of oxide layers on Mg(0001) and comparison of H2O adsorption on surface and bulk oxides," *Surf. Sci.*, vol. 233, no. 3, pp. 283–292, Jul. 1990.
[132] S. Campbell, P. Hollins, E. McCash, and M. W. Roberts, "Reaction of carbon dioxide with the magnesium(0001) surface," *J. Electron Spectrosc. Relat. Phenom.*, vol. 39, no. Supplement C, pp. 145–153, Jan. 1986.
[133] M. Santamaria, F. Di Quarto, S. Zanna, and P. Marcus, "Initial surface film on magnesium metal: A characterization by X-ray photoelectron spectroscopy (XPS) and photocurrent spectroscopy (PCS)," *Electrochimica Acta*, vol. 53, no. 3, pp. 1314–1324, Dec. 2007.
[134] E. V. Thomsen, B. Jørgensen, and J. Onsgaard, "Adsorption and reactivity of CO2 on the K/Cu(110) interface and the effect of photon irradiation," *Surf. Sci.*, vol. 304, no. 1, pp. 85–97, Mar. 1994.
[135] W. Taifan, J.-F. Boily, and J. Baltrusaitis, "Surface chemistry of carbon dioxide revisited," *Surf. Sci. Rep.*, vol. 71, no. 4, pp. 595–671, Dec. 2016.
[136] H.-J. Freund and M. W. Roberts, "Surface chemistry of carbon dioxide," *Surf. Sci. Rep.*, vol. 25, no. 8, pp. 225–273, Jan. 1996.
[137] R. G. Copperthwaite, P. R. Davies, M. A. Morris, M. W. Roberts, and R. A. Ryder, "The reactive chemisorption of carbon dioxide at magnesium and copper surfaces at low temperature," *Catal. Lett.*, vol. 1, no. 1–3, pp. 11–19, Jan. 1988.
[138] W. N. R. W. Isahak, S. Z. Hasan, Z. A. C. Ramli, M. M. Ba-Abbad, and M. A. Yarmo, "Enhanced physical and chemical adsorption of carbon dioxide using bimetallic copper–magnesium oxide/carbon nanocomposite," *Res. Chem. Intermed.*, pp. 1–13, Sep. 2017.
[139] T. Kravchuk and A. Hoffman, "Enhanced reactivity and selectivity in oxidation of Cu(100) and α-Cu–Al(5at.%)(100) surfaces studied by electron and ion spectroscopies," *Surf. Sci.*, vol. 600, no. 6, pp. 1252–1259, Mar. 2006.
[140] B. Eren, R. S. Weatherup, N. Liakakos, G. A. Somorjai, and M. Salmeron, "Dissociative Carbon Dioxide Adsorption and Morphological Changes on Cu(100) and Cu(111) at Ambient Pressures," *J. Am. Chem. Soc.*, vol. 138, no. 26, pp. 8207–8211, Jul. 2016.
[141] S. Stepanow *et al.*, "Deprotonation-Driven Phase Transformations in Terephthalic Acid Self-Assembly on Cu(100)," *J. Phys. Chem. B*, vol. 108, no. 50, pp. 19392–19397, Dec. 2004.
[142] J. D. Fuhr *et al.*, "Interplay between Hydrogen Bonding and Molecule–Substrate Interactions in the Case of Terephthalic Acid Molecules on Cu(001) Surfaces," *J. Phys. Chem. C*, vol. 117, no. 3, pp. 1287–1296, Jan. 2013.

[143] X.-F. Yang, A. Wang, B. Qiao, J. Li, J. Liu, and T. Zhang, “Single-Atom Catalysts: A New Frontier in Heterogeneous Catalysis,” *Acc. Chem. Res.*, vol. 46, no. 8, pp. 1740–1748, Aug. 2013.
[144] D. Skomski, S. Abb, and S. L. Tait, “Robust surface nano-architecture by alkali-carboxylate ionic bonding,” *J. Am. Chem. Soc.*, vol. 134, no. 34, pp. 14165–14171, Aug. 2012.
[145] R. F. W. Bader, *Atoms in Molecules: A Quantum Theory*, 1st Paperback Edition edition. Oxford England : New York: Clarendon Press, 1994.
[146] P. L. Popelier, *Atoms in Molecules: An Introduction*, 1 edition. Harlow: Prentice Hall, 2000.
[147] J. Tersoff and D. R. Hamann, “Theory of the scanning tunneling microscope,” *Phys. Rev. B*, vol. 31, no. 2, pp. 805–813, Jan. 1985.
[148] J. Tersoff and D. R. Hamann, “Theory and Application for the Scanning Tunneling Microscope,” *Phys. Rev. Lett.*, vol. 50, no. 25, pp. 1998–2001, Jun. 1983.
[149] A. Carrera *et al.*, “Controlling Carboxyl Deprotonation on Cu(001) by Surface Sn Alloying,” *J. Phys. Chem. C*, vol. 117, no. 33, pp. 17058–17065, Aug. 2013.
[150] W. Zhang, A. Nefedov, M. Naboka, L. Cao, and C. Wöll, “Molecular orientation of terephthalic acid assembly on epitaxial graphene : NEXAFS and XPS study,” *Phys. Chem. Chem. Phys.*, vol. 14, no. 29, pp. 10125–10131, 2012.
[151] M. Marschewski, C. Otto, L. Wegewitz, O. Höfft, A. Schmidt, and W. Maus-Friedrichs, “Adsorption analysis of thin films of terephthalic acid on Au and Al studied by MIES, UPS and XPS,” *Appl. Surf. Sci.*, vol. 339, no. Supplement C, pp. 9–14, Jun. 2015.
[152] T. Suzuki *et al.*, “Substrate effect on supramolecular self-assembly: from semiconductors to metals,” *Phys. Chem. Chem. Phys.*, vol. 11, no. 30, pp. 6498–6504, Aug. 2009.
[153] S. Clair, S. Pons, A. P. Seitsonen, H. Brune, K. Kern, and J. V. Barth, “STM Study of Terephthalic Acid Self-Assembly on Au(111): Hydrogen-Bonded Sheets on an Inhomogeneous Substrate,” *J. Phys. Chem. B*, vol. 108, no. 38, pp. 14585–14590, Sep. 2004.
[154] M. E. Cañas-Ventura *et al.*, “Coexistence of one- and two-dimensional supramolecular assemblies of terephthalic acid on Pd(111) due to self-limiting deprotonation,” *J. Chem. Phys.*, vol. 125, no. 18, p. 184710, Nov. 2006.
[155] A. J. Du, S. C. Smith, X. D. Yao, and G. Q. Lu, “Catalytic Effects of Subsurface Carbon in the Chemisorption of Hydrogen on a Mg(0001) Surface: an Ab-initio Study,” *J. Phys. Chem. B*, vol. 110, no. 4, pp. 1814–1819, Feb. 2006.
[156] A. Lombana *et al.*, “Surface Organization of Polyoxometalate Hybrids Steered by a 2D Supramolecular PTCDI/Melamine Network,” *J. Phys. Chem. C*, vol. 120, no. 5, pp. 2837–2845, Feb. 2016.
[157] X. Sun, H. T. Jonkman, and F. Silly, “Tailoring two-dimensional PTCDA–melamine self-assembled architectures at room temperature by tuning molecular ratio,” *Nanotechnology*, vol. 21, no. 16, p. 165602, 2010.
[158] A. G. Slater, L. M. A. Perdigão, P. H. Beton, and N. R. Champness, “Surface-Based Supramolecular Chemistry Using Hydrogen Bonds,” *Acc. Chem. Res.*, vol. 47, no. 12, pp. 3417–3427, Dec. 2014.
[159] Z. Feng *et al.*, “A competitive amino-carboxylic hydrogen bond on a gold surface,” *Chem. Commun.*, vol. 51, no. 26, pp. 5739–5742, Mar. 2015.

[160] J. Ma *et al.*, “Dianhydride-Amine Hydrogen Bonded Perylene Tetracarboxylic Dianhydride and Tetraaminobenzene Rows,” *J. Phys. Chem. B*, vol. 110, no. 25, pp. 12207–12210, Jun. 2006.
[161] M.-T. Nguyen, C. A. Pignedoli, M. Treier, R. Fasel, and D. Passerone, “The role of van der Waals interactions in surface-supported supramolecular networks,” *Phys. Chem. Chem. Phys.*, vol. 12, no. 4, pp. 992–999, Jan. 2010.
[162] Liang Hailin *et al.*, “Two-Dimensional Molecular Porous Networks Formed by Trimesic Acid and 4,4′-Bis(4-pyridyl)biphenyl on Au(111) through Hierarchical Hydrogen Bonds: Structural Systematics and Control of Nanopore Size and Shape,” *Angew. Chem. Int. Ed.*, vol. 50, no. 33, pp. 7562–7566, Jun. 2011.
[163] N. Lin, A. Langner, S. L. Tait, C. Rajadurai, M. Ruben, and K. Kern, “Template-directed supramolecular self-assembly of coordination dumbbells at surfaces,” *Chem. Commun.*, vol. 0, no. 46, pp. 4860–4862, Nov. 2007.
[164] A. Langner, S. L. Tait, N. Lin, C. Rajadurai, M. Ruben, and K. Kern, “Self-recognition and self-selection in multicomponent supramolecular coordination networks on surfaces,” *Proc. Natl. Acad. Sci.*, vol. 104, no. 46, pp. 17927–17930, Nov. 2007.
[165] H. Sigel and R. B. Martin, “Coordinating properties of the amide bond. Stability and structure of metal ion complexes of peptides and related ligands,” *Chem. Rev.*, vol. 82, no. 4, pp. 385–426, Aug. 1982.
[166] D. Walther, M. Ruben, and S. Rau, “Carbon dioxide and metal centres: from reactions inspired by nature to reactions in compressed carbon dioxide as solvent,” *Coord. Chem. Rev.*, vol. 182, no. 1, pp. 67–100, Feb. 1999.
[167] T. Steiner, “The Hydrogen Bond in the Solid State,” *Angew. Chem. Int. Ed.*, vol. 41, no. 1, pp. 48–76, Jan. 2002.
[168] W. Xu *et al.*, “Cyanuric Acid and Melamine on Au(111): Structure and Energetics of Hydrogen-Bonded Networks,” *Small*, vol. 3, no. 5, pp. 854–858, May 2007.
[169] F. Silly *et al.*, “Deriving molecular bonding from a macromolecular self-assembly using kinetic Monte Carlo simulations,” *Phys. Rev. B*, vol. 77, no. 20, p. 201408, May 2008.
[170] H.-M. Zhang *et al.*, “One-Step Preparation of Large-Scale Self-Assembled Monolayers of Cyanuric Acid and Melamine Supramolecular Species on Au(111) Surfaces,” *J. Phys. Chem. C*, vol. 112, no. 11, pp. 4209–4218, Mar. 2008.
[171] D. Bonifazi, S. Mohnani, and A. Llanes-Pallas, “Supramolecular Chemistry at Interfaces: Molecular Recognition on Nanopatterned Porous Surfaces,” *Chem. - Eur. J.*, vol. 15, no. 29, pp. 7004–7025, Jul. 2009.
[172] K. Banerjee, A. Kumar, F. F. Canova, S. Kezilebieke, A. S. Foster, and P. Liljeroth, “Flexible Self-Assembled Molecular Templates on Graphene,” *J. Phys. Chem. C*, vol. 120, no. 16, pp. 8772–8780, Apr. 2016.
[173] M. Böhringer, W.-D. Schneider, K. Glöckler, E. Umbach, and R. Berndt, “Adsorption site determination of PTCDA on Ag(110) by manipulation of adatoms,” *Surf. Sci.*, vol. 419, no. 1, pp. L95–L99, Dec. 1998.
[174] M. Mura, F. Silly, V. Burlakov, M. R. Castell, G. A. D. Briggs, and L. N. Kantorovich, “Formation Mechanism for a Hybrid Supramolecular Network Involving Cooperative Interactions,” *Phys. Rev. Lett.*, vol. 108, no. 17, p. 176103, Apr. 2012.

[175] L. Dong *et al.*, "A self-assembled molecular nanostructure for trapping the native adatoms on Cu(110)," *Chem. Commun.*, vol. 49, no. 17, pp. 1735–1737, Jan. 2013.
[176] A. Langner *et al.*, "Selective Coordination Bonding in Metallo-Supramolecular Systems on Surfaces," *Angew. Chem. Int. Ed.*, vol. 51, no. 18, pp. 4327–4331, Apr. 2012.
[177] P. A. Staniec, L. M. A. Perdigão, B. L. Rogers, N. R. Champness, and P. H. Beton, "Honeycomb Networks and Chiral Superstructures Formed by Cyanuric Acid and Melamine on Au(111)," *J. Phys. Chem. C*, vol. 111, no. 2, pp. 886–893, Jan. 2007.
[178] V. S. Vyas *et al.*, "Exploiting Noncovalent Interactions in an Imine-Based Covalent Organic Framework for Quercetin Delivery," *Adv. Mater.*, vol. 28, no. 39, pp. 8749–8754, Oct. 2016.
[179] R. Liu, G. Yuan, C. L. Joe, T. E. Lightburn, K. L. Tan, and D. Wang, "Silicon Nanowires as Photoelectrodes for Carbon Dioxide Fixation," *Angew. Chem. Int. Ed.*, vol. 51, no. 27, pp. 6709–6712, Jul. 2012.
[180] M. Ruben, D. Walther, R. Knake, H. Görls, and R. Beckert, "Fixation of Carbon Dioxide by Oxalic Amidinato Magnesium Complexes: Structures and Reactions of Trimetallic Magnesium Carbamato and Related Complexes," *Eur. J. Inorg. Chem.*, vol. 2000, no. 5, pp. 1055–1064, May 2000.
[181] K. M. O'Donnell, O. Warschkow, A. Suleman, A. Fahy, L. Thomsen, and S. R. Schofield, "Manipulating the orientation of an organic adsorbate on silicon: a NEXAFS study of acetophenone on Si(0 0 1)," *J. Phys. Condens. Matter*, vol. 27, no. 5, p. 054002, 2015.

List of publications

The online version of the publications generated by this research can be found in the following link:

http://www.mpg-epfl.mpg.de/1007435/Max-Planck-EPFL_Nanolab

Curriculum Vitae

Personal information

Name:	Daniel Eduardo HURTADO SALINAS
Date of birth:	February 19, 1988
Nationality:	Peruvian

Education

Jan 2014-Jun 2018	**École Polytechnique Fédérale de Lausanne**, *PhD in Physics*, Lausanne, Switzerland. Thesis: *"Metal-organic coordination networks for CO_2 and O_2 Activation at room temperature"* Advisors: Dr. Magali Lingenfelder Prof. Klaus Kern
Feb 2016-May 2016	**Max Planck Institute Stuttgart**, *Researcher as part of the Max-Planck-EPFL program, Stuttgart, Germany.*
Oct 2011–Sept 2013	**Tokyo Institute of Technology**, *M.S. in Science*, Tokyo, Japan. Thesis: *"Room temperature operation in single electron transistors and solid-state molecular devices"* Advisor: Prof. Yutaka Majima
Jan 2009-Sep 2011	**National University of San Marcos**, *Licentiate in Physics*, Lima, Peru. Thesis: *"Study of Superficial Morphology Evolution and Crystallization of thermally treated Cu/SiO_2 Thin Films"* *Advisor: Prof. Ángel G. Bustamante Domínguez*
Jan 2005-Dec 2009	**National University of San Marcos**, *Bachelors in Physics*, Lima, Peru.

Research Experience

Acquired Skills.

- Scanning tunnel microscopy (STM).
- Self-assembly strategies for bottom-up fabrication.
- Biomimetic catalysis on surfaces.
- Organic chemistry.
- Surface science.
- Vacuum technology: vacuum gauges, ion pumps, turbo pumps.
- Electrical characterization: probe sensing, semiconductor parameter analysis, multifunc-tional synthesis.
- Physical characterization: scanning electron microscopy, X-ray diffraction.
- Electron-beam lithography, photolithography, and metal evaporation.
- Electroless gold plating.
- Software packages: Igor, Origin, Illustrator.

Patents

2015 WO/2014/142040, Yutaka Majima, Toshiharu Teranishi, Yasuo Azuma, Masanori Sakamoto, Shinya Kano, **Daniel Eduardo Hurtado Salinas**, "*Electronic Element*", 2014.9.18

Publications

2015 Victor M. Serdio V, Taro Muraki, Shuhei Takeshita, **Daniel E. Hurtado S**, Shinya Kano, Toshiharu Teranishi and Yutaka Majima, "Gap separation-controlled nanogap electrodes by molecular ruler electroless gold plating", **RSC Adv.**, **5**, 22160-22167 (2015). DOI: 10.1039/C5RA00923E

2012 L. De Los Santos Valladares, **D. Hurtado Salinas**, A. Bustamante Dominguez, D. Acosta Najarro, S.I. Khondaker, T. Mitrelias, C.H.W. Barnes, J. Albino Aguiar, Y. Majima, "Crystallization and electrical resistivity of Cu_2O and CuO obtained by thermal oxidation of Cu thin films on SiO_2/Si substrates", *Thin Solid Films*, **520**, 6368-6374 (2012). DOI: 10.1016/j.tsf.2012.06.043

2010 **Daniel Hurtado Salinas**, Angel Bustamante Dominguez, Lizbet Leon Felix, Luis De los Santos Valladares and Yutaka Majima, "Crystallography and surface morphology evolution of thermally treated Cu thin films on SiO_2/Si substrates", *Revista de Investigacion de Fisica*, **13**, 101301101 (2010). ISSN: 1728-2977

Presentations

Oral Presentations

United States | April 2018 "Hybrid Metal-Organic Bio-Inspired Networks and Their Reactivity Towards CO_2 and O_2 at Room Temperature", 2018 MRS Spring Meeting, Phoenix.

Germany | Oct 2014 "Reactivity of Bio-Inspired Ionic Networks for CO_2 Activation", 3rd Science Day of the Max Planck-EPFL Center for Molecular Nanoscience and Technology, the Fritz-Haber Institute, Berlin.

Turkey | Sep 2014 "Reactivity of Ionic Networks of Magnesium and Terephtalic Acid on Cu(100) in the Presence of Carbon Dioxide", European Conference on Surface Science (ECOSS-30), Antalya.

Japan | Mar 2013 *"Room Temperature Memory Operation in a Solid-State Device based on Thiol-Functionalized Oligo (Phenylene-Ethynylene)-Protected Gold Nanoparticles"*, 60th Spring Meeting 2013 of The Japan Society of Applied Physics, Kanagawa Institute of Technology.

Peru | Jan 2013 *"Fabrication and electrical characterization of chemically assembled nano-electronic devices"*, Summer Colloquium of Physics, National University of San Marcos.

Peru | Jan 2013 *"Room temperature Coulomb oscillation and low temperature*

discrete energy levels in a chemically assembled top-gated SET", XIX International Scientific Meeting of Summer (ECI), National University of Engineering.

Japan | Sep 2012 — *"Room Temperature Coulomb Oscillation in Chemically Assembled SET with SiN_x Passivation Layer"* & *"Room Temperature Solid-State Molecular Device by Using Porphyrin Derivatives"* The 73rd Autumn Meeting 2012 for The Japan Society of Applied Physics, Ehime University and Matsuyama University.

Poster Presentations

France | Oct 2016 — "Hybrid metal-organic coordination networks for CO_2 and O_2 activation at room temperature", European Conference on Surface Science (ECOSS-32), Grenoble.

Switzerland | Jan 2016 — "Metal-Organic Coordination Networks for CO_2 and O_2 activation", Swiss Working Group for Surface and Interface Science (SAOG), University of Fribourg.

Switzerland | Jan 2015 — "Reactivity of Metal-Organic Coordination Networks for CO_2 activation", Swiss Working Group for Surface and Interface Science (SAOG), University of Fribourg.

Korea | Aug 2013 — "Memory Operation in Electroless Gold Plated Nanogap", Korea-Japan Joint Forum International Conference on Organic Materials for Electronics and Photoelectronics, Pusan National University.

Japan | Aug 2012 — *"Room Temperature Operation Solid-State Molecular Device by Using Porphyrin Derivatives"*, Korea-Japan Joint Forum International Conference on Organic Materials for Electronics and Photoelectronics, Tohoku University.

Peru | Nov 2011 — *"Formation and growth of nano-grains of copper oxide in thermically oxidized Cu/SiO_2 thin films"*, Workshop about the importance, development, formation and disclosure of Nanoscience and Nanotechnology in Peru.

Awards, Distinctions, and Scholarships

JASSO — Monbukagaskusho Honors Scholarship for International Students

Natl. Univ. San Marcos — Graduated 2nd out of 126 students

Languages

Spanish **Native**
English **Advanced**
French **Basic**